

Charles University in Prague  
Faculty of Mathematics and Physics

## DOCTORAL THESIS



Mgr. Helena Reichlová

## Nanostructures and Materials for Antiferromagnetic Spintronics

Institute of Physics ASCR, v.v.i.

Supervisor of the doctoral thesis: Ing. Vít Novák, CSc.

Study programme: Physics of Nanostructures

Specialization: Spintronics

Prague 2015

I declare that I carried out this doctoral thesis independently, and only with the cited sources, literature and other professional sources.

I understand that my work relates to the rights and obligations under the Act No. 121/2000 Coll., the Copyright Act, as amended, in particular the fact that the Charles University in Prague has the right to conclude a license agreement on the use of this work as a school work pursuant to Section 60 paragraph 1 of the Copyright Act.

In ..... date .....

signature of the author

Title: Nanostructures and Materials for Antiferromagnetic Spintronics

Author: Mgr. Helena Reichlová

Department: Institute of Physics ASCR, v.v.i.

Supervisor: Ing. Vít Novák, CSc., Institute of Physics ASCR, v.v.i.

Abstract: This thesis is focused on two open problems of antiferromagnetic (AFM) spintronics: manipulation of AFM coupled moments and development of new materials combining AFM and semiconductor properties. We present three particular methods enabling AFM moments manipulation. The first method, based on the exchange spring effect in an AFM/FM double layer, strongly depends on the AFM layer thickness and temperature. We systematically vary these two parameters and identify the conditions when AFM moments can be manipulated. By the second method, cooling an AFM in a magnetic field through the critical temperature, we prove the concept of a fully AFM-based (containing no FM) spintronic device. The last studied method is based on current induced effects in nanostructures containing an AFM. By systematic study of samples with and without AFM we demonstrate the ability of AFM moments to absorb a current induced torque. Relying neither on a FM nor on cooling in magnetic field, this method represents an elegant way of AFM moments manipulation. In the second experimental part new materials for AFM spintronics are discussed, and one representative example, CuMnAs, is studied in detail. Characterization of bulk and epitaxial CuMnAs is presented and first spintronic functionality is shown.

Keywords: spintronics, magnetism, antiferromagnetic materials

# Acknowledgment

This thesis covers work done at the Institute of Physics at Academy of Science in Prague during years 2010-2015.

Firstly, I would like to thank my supervisor Vít Novák for his support and patience. Great thanks belongs also to everybody who advised me - Xavi Martí, Joerg Wunderlich, Kamil Olejník and Tomáš Jungwirth.

I am also grateful to our team from Cukrovarnická - Karel Vyborný, Vlastík Jurka, Karel Hruška, Pavel Zich, Jirka Zyka, Lukáš Nádvorník, Zbyněk Šobán, Štěpán Svoboda, Libor Šmejkal, Jakub Železný, Zdeněk Kašpar - for their advises, help and the great every day atmosphere. For support and friendly atmosphere in the common SQUID laboratory, I would like to acknowledge Miroslav Maryško and Jan Šváb.

For perfect administrative support in every possible situation I would like to thank Dagmar Zádrapová and Eva Hachlová. And for smooth organization of my study program to Václav Holý.

A significant number of measurements and sample fabrications would not be possible without our great collaborating labs. Above all I would like to thank our collaborators from the X-Ray group and the Opto-Spintronics group at Charles University, Hitachi Japan, Hitachi Cambridge, University of Nottingham, LNESS Como and ICMAB Barcelona.

I would also like acknowledge everybody who has participate on my education: All my teachers and friends from Faculty of Mathematics and Physic at Charles University in Prague, University of Louis Pasteur in Strasbourg and Ohio State University to share their knowledge with me. And my teachers from high school, Josef Marek and Karel Bartuška, who encouraged me to study physics.

Great thanks belongs also to my family for supporting me to be curious and independent. And for a bit of all mentioned above to Dominik.

# Contents

<b>1</b>	<b>Antiferromagnetic Spintronics: Motivation and Goals</b>	<b>3</b>
<b>2</b>	<b>Introduction</b>	<b>5</b>
2.1	Magnetism - Ferromagnetism and Antiferromagnetism . . . . .	5
2.1.1	Energy Functional and its Anisotropy . . . . .	11
2.1.2	Exchange Coupling Effect . . . . .	13
2.2	Magnetotransport . . . . .	17
2.2.1	Hall Effects . . . . .	17
2.2.2	Spin Galvanic Effect . . . . .	18
2.2.3	Magnetoresistance . . . . .	19
2.2.4	Magnetoresistance in layered systems . . . . .	20
2.2.5	Magnetotransport in Antiferromagnets . . . . .	23
2.3	Thermoelectric effects . . . . .	24
2.3.1	Thermal Effects in Antiferromagnets . . . . .	26
2.4	Spintronics . . . . .	26
2.4.1	Spin Valve . . . . .	27
2.4.2	Spin Torque . . . . .	30
2.4.3	Ferromagnetic and Antiferromagnetic Spintronics . . . . .	33
<b>3</b>	<b>Manipulation of the Antiferromagnetic Moments</b>	<b>35</b>
3.1	Concepts to Manipulate AFM Moments . . . . .	35
3.2	Materials and Structures . . . . .	35
3.2.1	IrMn Antiferromagnet . . . . .	35
3.2.2	Layered Structures . . . . .	36
3.2.3	Device Fabrication for Magnetotransport . . . . .	37
3.3	Samples characterization . . . . .	38
3.3.1	X-Ray Diffraction and Reflectivity . . . . .	38
3.3.2	Scanning Probe Microscopy . . . . .	40
3.3.3	Magnetometry . . . . .	40
3.4	AFM Moments Manipulation by Exchange Spring Effect . . . . .	44
3.4.1	SQUID Measurements . . . . .	44
3.4.2	TAMR Measurements . . . . .	48
3.4.3	Discussion of Results in Context of Existing Models . . . . .	50
3.4.4	Thermal Induced Magnetization Fluctuation . . . . .	52
3.4.5	Summary of the Exchange Spring Based AFM Manipulation . . . . .	53
3.5	AFM Moments Manipulation by Field Cooling . . . . .	54
3.5.1	Summary of Field Cooling Based AFM Manipulation . . . . .	56
3.6	AFM Moments Manipulation by Current Induced Torques . . . . .	57
3.6.1	Current induced torques on AFM moments . . . . .	57
3.6.2	Samples . . . . .	58
3.6.3	Detection of current induced torques . . . . .	58
3.6.4	Second Harmonics Detection . . . . .	60
3.6.5	Artifacts Caused by Sample Fabrication . . . . .	60
3.6.6	Samples with Ta/IrMn/CoFeB . . . . .	64
3.6.7	Samples with Ta/IrMn . . . . .	78

3.6.8	Summary of Current Induced Manipulation of AFM Moments	79
<b>4</b>	<b>New Materials for Antiferromagnetic Spintronics</b>	<b>80</b>
4.1	Route to AFM Semiconductors . . . . .	80
4.2	Bulk Orthorhombic CuMnAs . . . . .	82
4.2.1	Technology of Fabrication . . . . .	82
4.2.2	Structural Analysis . . . . .	82
4.2.3	Magnetic Characterization . . . . .	82
4.2.4	Transport Characterization . . . . .	83
4.3	Epitaxial CuMnAs . . . . .	84
4.3.1	Magnetic Characterization . . . . .	85
4.3.2	Structural Analysis . . . . .	86
4.3.3	Transport Characterization . . . . .	88
4.4	Exchange Coupling on CuMnAs/Fe Interface . . . . .	88
4.4.1	Temperature Dependence of Exchange Bias . . . . .	89
4.4.2	Other Possible Sources of $m(H)$ Shift . . . . .	90
4.5	Summary of CuMnAs Characterization . . . . .	91
	<b>Conclusion</b>	<b>92</b>
	<b>A Appendix</b>	<b>95</b>
A.1	Measurement Instruments . . . . .	95
A.1.1	SQUID . . . . .	95
A.1.2	Transport Measurements . . . . .	95
A.2	List of Presented Samples . . . . .	96
A.2.1	Exchange Spring Experiments . . . . .	96
A.2.2	Field Cooling Experiments . . . . .	97
A.2.3	Current Induced Torques Experiments . . . . .	97
A.2.4	Epitaxial CuMnAs . . . . .	97
A.3	Sample Mounting for Transport Measurement . . . . .	98
A.4	Lithography Processing . . . . .	98
A.5	Expected Contribution to Second Harmonic Signal . . . . .	99
	<b>List of Publications</b>	<b>104</b>
	<b>Bibliography</b>	<b>106</b>

# 1. Antiferromagnetic Spintronics: Motivation and Goals

Although antiferromagnetically (AFM) ordered spins were discovered in the first half of the 20th century they were long time considered as a theoretically interesting magnetic state, however, without any technological application. This can be illustrated from a quote of the Nobel lecture of Louis Néel in 1970: 'A large number of AFM materials is now known: these are generally compounds of the transition metals containing oxygen or sulphur. They are extremely interesting from the theoretical viewpoint, but do not seem to have any applications.' [1]

20 years later, AFM were theoretically described in almost every textbook, however, any technological application was still not predicted, as mentioned for example in [2]: 'As a result of the zero spontaneous magnetization within the domains and the consequent low permeability and susceptibility of AFM they do not find many technological applications.'

First technological application of AFM occurred with development of magnetic memory based on the giant magnetoresistance effect. AFM materials are used as a stabilization element to hold the magnetization orientation of one of the ferromagnetic layers via the exchange coupling between AFM and FM. This led to growing interest in AFM materials as mentioned also in a textbook from the year 2003: 'Moreover, there is a growing interest in AFM materials that originates from the application of the exchange-bias effect in spin valves, field sensors and non-volatile magnetic random access memories (M-RAMs).' [3]

The use of AFM materials as an active element of a spintronic device was predicted first theoretically in 2010 [4] and confirmed experimentally in 2011 [5]. Park et al. demonstrated that AFM material IrMn can exhibit tunneling anisotropic magnetoresistance. This and following experiments [6, 7, 8] showed that some of the effects well known from FMs can be repeated in AFMs. Compared to FM, AFM coupled moments have, however, several important advantages as will be in more details discussed later.

To fully exploit the potential of the AFM spintronics, some of the major questions need to be solved. Two of the most important ones are how to detect and how to effectively manipulate the AFM moments. The rigidity of AFM moments against external field that makes AFM appealing for spintronic application is in the same time the main hurdle when AFM moments should be tilted or even switched. Another actively studied problem of AFM spintronics is fabrication of suitable materials for "semiconductor AFM spintronics". As will be discussed in chapter 2, one of the major drawback of combining semiconducting and ferromagnetic properties into one material is the lack of room temperature ferromagnetic semiconductors. This is, however, not true for materials combining semiconducting and AFM properties and many of AFM semiconductors exist as discussed in the introduction of chapter 4. The spintronic functionality of AFM semiconductors was, however, not demonstrated yet.

**This thesis is focused on these two open problems of antiferromagnetic spintronics - detection and manipulation of the AFM moments and combination of semiconducting and antiferromagnetic properties**

**into one material.**

This thesis consists of four parts. After the motivation, the second chapter contains a brief introduction to magnetism that is required to understand the experimental parts. Broader overview of recent spintronic research and the context of this work is also mentioned here.

The third chapter is focused on a systematic study of AFM moments manipulation and detection in metals. Sample characterization and fabrication is followed by the experimental results. Well known antiferromagnet IrMn was used for fabrication of nanostructures which are afterwards studied by transport and magnetometry methods. To manipulate the AFM moments we have employed several effects known previously, in particular, the exchange spring effect and cooling in an external magnetic field, and we studied in details the behavior of AFM. We have detected the AFM moments orientation by tunneling anisotropic magnetoresistance and we identified the conditions when spin-valve like signal can be observed in AFMs. Finally, we have studied a novel approach to manipulate magnetic moments by spin torques. We have prepared nanostructures including an ultra thin AFM, we developed a method to measure and separate various current induced effects and we have observed the first indication of spin orbit torque absorbed by an AFM.

The fourth chapter of the thesis is focused on fabrication and characterization of a new promising materials for antiferromagnetic spintronics. We discuss the route from ferromagnetic semiconductors towards the antiferromagnetic ones and we study in detail one promising material - CuMnAs. We characterized samples prepared by chemical synthesis and by epitaxial growth. Experimentally observed exchange coupling on the interface CuMnAs/Fe is shown confirming the AFM order and a basic spintronic functionality. Other potential sources of exchange bias and exchange broadening (beside the AFM/FM interface) are discussed and experimentally excluded.

The last part summarizes the achieved results.

## 2. Introduction

Magnetism is a phenomenon originating in quantum physics that is studied in various ways by a broad community of scientists. In the same time it is a phenomenon that is extremely important for technological applications (starting from a compass to a modern hard-drive) and therefore known also to almost everybody outside the scientific community. Although it is far beyond the scope of this work to describe the origin of magnetism, we will define terminology, relation between variables and basic concepts of magnetism and exchange coupling in this chapter. This will be a starting point to a short introduction to the magnetotransport and thermo-electric phenomena that will be described in the section 2.3. In the last section the spintronic research will be introduced and the recent understanding of problems studied in this thesis will be briefly summarized.

### 2.1 Magnetism - Ferromagnetism and Antiferromagnetism

To understand the origin of magnetism one needs to go into the nanoscale dimensions and study the magnetic properties on the atomic level. The origin of a magnetic moment of an atom are the electron's orbital motion, a change in the motion caused by an external magnetic field and the electron's spin. Here will be given only a brief overview of quantities and notation that will be used in this work [9, 2, 3, 10].

Energy of an electron with a magnetic momentum  $\mathbf{m}$  and spin angular momentum  $m_S$  in external magnetic field  $\mathbf{H}$  is

$$E = -\mu_0\mathbf{m}\cdot\mathbf{H} = g\mu_B\mu_0Hm_S, \quad (2.1)$$

where  $\mu_0$  is the permeability of free space and  $g$  is the g-factor.

Torque  $\mathbf{T}$  acting on a magnetic moment  $\mathbf{m}$  is defined as

$$\mathbf{T} = \mu_0\mathbf{m} \times \mathbf{H}. \quad (2.2)$$

The magnetization  $\mathbf{M}$  is defined as a sum of magnetic moments in a unit volume.

Magnetization depends on the external magnetic field. The response of a material to an external magnetic field is described by the magnetic susceptibility  $\chi$  defined by the following equation [9]

$$\chi = \frac{M}{H}. \quad (2.3)$$

Based on the criteria how macroscopic materials respond to an external magnetic field we can divide them into several classes. The simplest and most natural way is to define three group of materials summarized into Tab. 2.1 with corresponding values of the magnetic susceptibility.

Historically much later, after identifying the three classes mentioned above, several other magnetic phases were discovered. Based on their spin textures we define ferrimagnets, helimagnets, antiferromagnets and others. These materials

Material	$\chi$	Example
Diamagnet	$\chi$ negative	Silicon, Gold
Paramagnet	$\chi \sim 10^{-3} - 10^{-5}$	Aluminum, Platinum
Ferromagnet	$\chi \sim 50 - 10000$	Iron, Cobalt

Table 2.1: Classes of materials based on their response to an external magnetic field and the corresponding values of susceptibility. [2]

belong to the same class as ferromagnets because the magnetic moments are ordered. In the following paragraph we will briefly introduce classes of magnetic phases relevant for this work.

**Diamagnetism** In diamagnetic materials all the electrons are paired (having spin up and down compensating), therefore there is no permanent net magnetic moment per atom. On the atomic level only the change of the orbital motion of electrons under an external magnetic field gives rise to a diamagnetic response. The susceptibility of diamagnets was explained in 1905 by Paul Langevin [11] by considering electron motion around a nucleus as a current loop generating magnetic moment. In zero magnetic field the total moment of two paired electrons is canceled. In case of non-zero external magnetic field change of the magnetic flux through the loop leads to an induced moment which is, in agreement with Lenz law, in the opposite direction than the external magnetic field. The susceptibility in the Langevin model of diamagnetism depends on the number of electrons  $Z$  and number of atoms  $N$  in a volume  $V$

$$\chi = \frac{M}{H} = -\frac{N e^2 \mu_0}{V 6m_e} \sum_i^Z \langle R_i^2 \rangle \quad (2.4)$$

$m_e$  is electron mass,  $e$  is electron charge and  $R_i$  is the radius of the electrons orbital. From Eq. 2.4 follows that diamagnetism is independent of temperature. Majority of known elements in nature are diamagnetic.

**Paramagnetims** Paramagnetic (PM) properties are resulting from the presence of unpaired electrons. It means that, unlike in diamagnets, both the orbital angular momentum and electron spin are contributing to the magnetic moment. The magnetic moment of a paramagnet is positive when a positive external magnetic field is applied and for complete polarization (aligning all moments to the direction of the applied field) infinitely high magnetic field is needed. Susceptibility of a paramagnet follows Curie Law

$$\chi = \frac{C}{T} \quad (2.5)$$

$C$  is a material constant including effective magnetic moment of paramagnetic ion. Each material with unpaired electrons becomes paramagnetic at certain temperature which can be very high for magnetically ordered materials. For materials that undergo transition from magnetically ordered state (as ferromagnet, antiferromagnet etc) to paramagnet a more general form of Eq. 2.5 is valid

$$\chi = \frac{C}{T - \theta}, \quad (2.6)$$

where  $\theta$  is a constant which is positive and equal to critical temperature  $T_C$  for materials undergoing FM-PM transition, and negative for materials undergoing the AFM-PM transition at critical temperature  $T_N$ .

**Ferromagnetism** Ferromagnets (FM) are a special class of materials in which net magnetic moment persists also when external magnetic field is zero. FM materials, similar to paramagnets, have unpaired electrons. The main difference is that, unlike PM without any collective interaction of atomic magnetic moments, FM materials show very strong interaction between atomic moments. Phenomenological explanation was given in 1907 by Pierre Ernest Weiss [12] by introducing the Weiss molecular field. It is an effective field that aligns the neighboring magnetic moments of atoms. It, however, does not act as an external field since it does not fulfill the Lorentz force law. It can not be explained by any effect known at that time (e.g. the dipole-dipole interaction). The origin of the Weiss molecular field was explained thirty years later by including the spin degree of freedom to the wave function of an electron. The spin-dependent Hamiltonian leads to Heisenberg exchange energy expressed using the electrons spins  $\mathbf{S}_i$  as

$$E_{\text{ex}} = -J \sum_{i,j} \mathbf{S}_i \mathbf{S}_j, \quad (2.7)$$

where  $J$  is the exchange constant characterizing the coupling between the spins in a magnetically ordered material. It has positive values for FM materials and negative for AFM materials.

There is only a small number of itinerant FM materials in nature (compared to a high number of AFMs). A simple picture of competing kinetic and exchange energy leads to the Stoner criterion which sets the condition if a material is FM or PM. The material is FM if

$$J \cdot D(E_F) \geq 1 \quad (2.8)$$

where  $D(E_F)$  is the density of states at the Fermi level. The Stoner criterion is fulfilled by only few materials, for example Cobalt, Iron or Nickel.

**Heusler alloys** Beside the magnetic elements, as Fe or Ni, also variety of alloys based on non-magnetic elements exhibit FM behavior. One example of these materials are Heusler alloys [13] - FM alloys with fcc crystal structure and composition of atoms in ratio  $X_2YZ$  (or  $XYZ$  for half Heusler alloys). Thanks to the double-exchange mechanism between magnetic neighbors the alloy is magnetic. This group of materials consists of more than 1500 alloys (from which more than 250 compounds are semiconductors) whose properties can be predicted from number of their valence electrons [14].

Because of the more complex interactions between the particular moments in a FM material, the magnetization loop contains more information than in case of paramagnetic or diamagnetic materials. In Fig. 2.1 an example of magnetization as a function of applied magnetic field for a FM material is shown. The important characteristics of a FM material, schematically indicated in Fig. 2.1, include:

- Saturation magnetization  $M_S$ , under sufficiently high magnetic field all the magnetic moments are aligned and magnetization of a material is saturated.  $M_S$  is a characteristic property of a material. For example  $M_S(Fe) \sim 1.7 \times 10^6 \text{ Am}^{-1}$ ,  $M_S(\text{Permalloy}) \sim 0.63 \times 10^6 \text{ Am}^{-1}$ .
- Coercive field  $H_C$  is the strength of the field needed to reduce the magnetic induction to zero. In other words coercivity measures the ability of a FM to withstand an external magnetic field without losing the magnetization. An expression for  $H_C$  will be given later in this chapter.
- Remnant magnetization  $M_R$  is the magnetization remaining when magnetic field is zero.

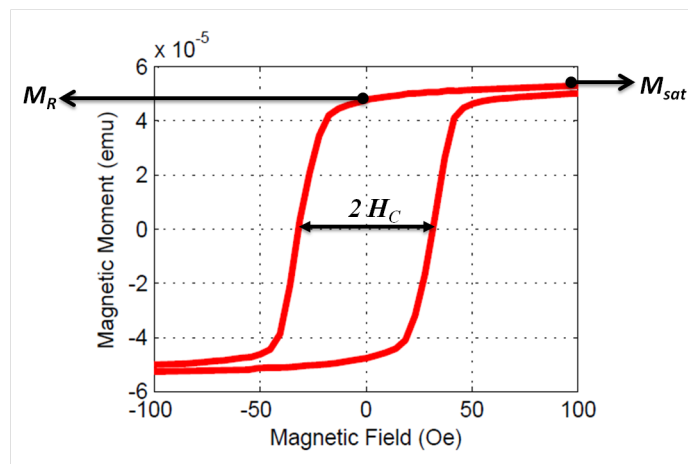


Figure 2.1: Example of a magnetization loop of a FM material. Saturation magnetization, Coercive field and Remnant magnetization are indicated.

The critical temperature at which material loses its FM properties is the Curie temperature  $T_C$ . In Fig. 2.2 (a) a typical temperature dependence of FM magnetization is shown.

**Antiferromagnetism** Antiferromagnets (AFM) are materials in which the net magnetic moment is zero although the magnetic moments are oriented; in this thesis we will use term AFM moments for antiferromagnetically ordered magnetic moments. AFMs were longtime considered paramagnets until 1930's when L. Néel proposed the existence of another magnetically ordered state (almost simultaneously with L. D. Landau who, however, did not believe for long time that the AFM exist in nature [15, 16]). Several studies of materials with zero net magnetic moment revealed very different temperature dependence of susceptibility than expected for a paramagnet (summarized in [17]). The susceptibility did not follow Curie law in the whole temperature range but exhibited a peak at a certain temperature. The  $\chi(T)$  dependence was explained theoretically (for example [18]) as a transition between paramagnetic and antiferromagnetic order. The critical temperature, at which the AFM order appears, is the Néel temperature  $T_N$  and it corresponds to the maxima of the  $\chi(T)$  function. In 1949 the AFM order existence was confirmed by neutron diffraction [19]. A typical example of  $\chi(T)$  is shown in the right panel in Fig. 2.2: when an external magnetic

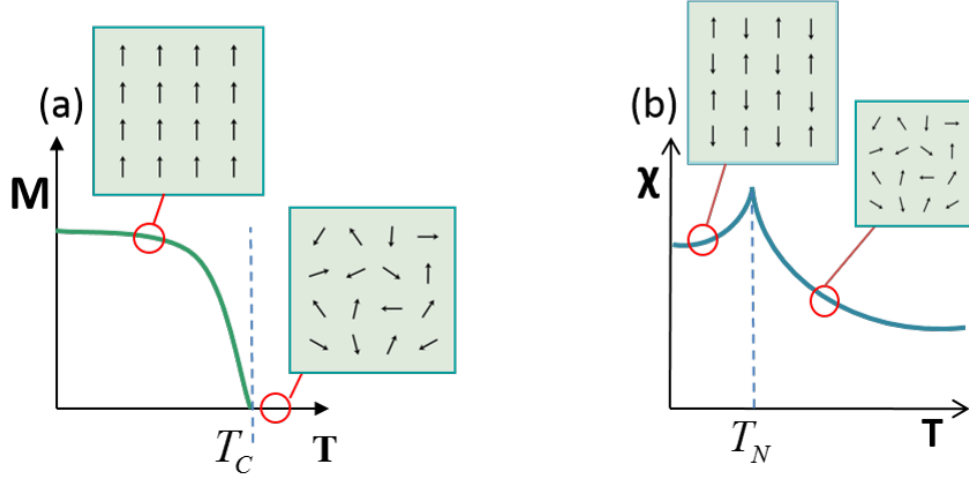


Figure 2.2: Magnetization of a FM in external magnetic field (a) and susceptibility of an AFM (b) as a function of temperature. Critical temperature of a FM is called Curie temperature, for an AFM it is Néel temperature.

Material	bulk $T_N$	source
Cr	67 K	[21]
MnO	122 K	[10]
MnTe	310 K	[22]
IrMn <sub>3</sub>	730 K	[23]
$\gamma$ -IrMn	650 K	[23]
CuMnAs epitaxial	575 K	[24]

Table 2.2: Example of AFM and their bulk  $T_N$ .

field is applied the AFM becomes weakly magnetized due to a small tilt of the AFM moments. In zero magnetic field no magnetic moment can be measured. The susceptibility of materials undergoing an AFM-PM transition is described by the Eq.2.6 where the constant  $\theta < 0$  in the range above  $T_N$ . Whereas there is only few FMs in nature, AFM order is relatively common. Several examples of AFM materials including their Néel temperature are summarized in Tab.2.1. In context of this thesis it is important to note that the bulk  $T_N$  can be reduced if an AFM material is grown as a very thin film [20, 7].

As described above, AFMs are magnetically ordered materials with zero net magnetic moment. However, unlike FM with all moments parallel, the AFM moments do not need to be only antiparallel and can be oriented in a different fashion. In fact, there is a large number of AFM spins arrangements given by the exchange and anisotropy energy of a particular material. The exchange energy of an AFM material prefers to keep two neighboring moments perfectly antiparallel and the magnetic anisotropy sets the preferred orientation of the magnetic moments relative to the crystallography direction. The resulting spin arrangements can be very complex and the exact spin texture for many of materials is not known. Here we show only three examples of AFM spin textures. The simplest example is a cubic lattice with antiferromagnetic coupling between one moment and all its neighbors as schematically shown in Fig. 2.3 (a). An example of this

spin arrangement is MnO.

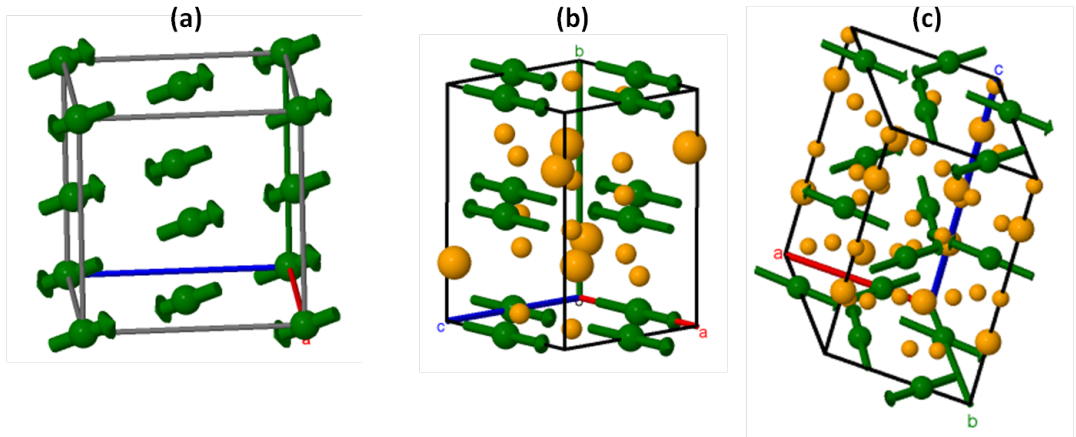


Figure 2.3: Example of antiferromagnetic spin arrangements. (a) cubic lattice with AFM coupling between the moment and all its neighbors. (b) AFM coupling between the planes. (c) Non-collinear spin texture. [25]

Next common AFM spin texture is ferromagnetic coupling in one plane and the AFM coupling between two planes. This is schematically shown in Fig. 2.3 (b). Although in this figure the moments are pointing in one of the crystallographic planes, it is not always the case. Generally the moments can point in an arbitrary direction (and still be coupled antiferromagnetically with the next plane). Example of such arrangement is MnTe where moments in-plane are FM coupled, the planes are AFM coupled and the exact orientation (angle) of the moments in-plane is not known [22].

Last presented example of AFM order is so called non-collinear or frustrated AFM. It consists of, for example, face center cubic and hexagonal lattices where magnetic moments are organized in triangles. In a triangle it is obviously not possible to orient all three spins to be antiparallel because after aligning two spins antiparallely the third would experience "frustration" where to point to keep the zero total magnetization. Instead, the spins are arranged in other, non-collinear, fashion as shown schematically in Fig. 2.3 (c). An example of non-collinear AFM is  $\text{IrMn}_3$  [26].

Beside variety of spin arrangements within those shown in Fig. 2.3 several other examples of AFM ordering exist (for example helimagnets). They are, however, not studied in this thesis and thus will not be discussed.

Similar to  $\mathbf{M}$  in case of FM materials, a vector giving direction of the moments exists for AFM materials. It is called Néel vector  $\mathbf{L}$ , it has direction parallel to the spins (if they are ordered antiparallel) and the amplitude corresponds to the sum of the two sublattices. The definition of the Néel vector is more sophisticated for non-collinear AFMs [27]. Following symmetry arguments, multiple Néel vectors can be defined as a different linear combination of the particular sublattices [28].

**Spin Glass** Last magnetic texture that will be mentioned is the spin glass (SG) magnetic order [29]. In this magnetic phase short range correlation are competing with long range interactions described for FM or AFM. The electronic magnetic moment is present but there is roughly equal probability to be coupled ferro- or

antiferromagnetically. As a result, a certain level of randomness plays role in the final orientation of magnetic moments. A regular pattern known from FM or AFM is not present, instead, random state is formed. At low temperature the spins are "frozen" in a particular state hence the name "glass". A prototype SG material is a dilute magnetic alloy, with a small amount of magnetic impurity randomly substituted into the lattice of a nonmagnetic metallic host, for example, CuMn. In the last decades lot of effort was put to understand and quantify the spin glass phase [30, 31, 32]. Although the topic of this thesis is not to study SG systems effects related to the SG phenomenon will be discussed later in this chapter and also need to be considered in our experiments.

### 2.1.1 Energy Functional and its Anisotropy

In the previous chapter we have described concepts, terminology and basic classes of magnetic materials. In this chapter we will discuss energies that need to be considered in order to describe the macroscopic properties as saturation field, anisotropy or coercive field.

**Demagnetizing Energy** We have mentioned already the energy of a magnetic moment in a magnetic field in Eq. (1.1). Beside an external magnetic field the magnetic moment of an atom is also affected by the dipolar field of its neighbors. The added effective field is called *demagnetizing field*  $H_d$  and it is related to the shape of the sample. We define the *demagnetizing factor*  $N_d$ . It is generally a tensor reflecting the geometry of a sample with trace  $\text{Tr}(N_d) = 1$ . Example of  $N_d$  for a spherical sample and a thin film perpendicular to  $z$  sample are:

$$N_d(\text{sphere}) = \begin{pmatrix} \frac{1}{3} & 0 & 0 \\ 0 & \frac{1}{3} & 0 \\ 0 & 0 & \frac{1}{3} \end{pmatrix} \quad (2.9)$$

$$N_d(\text{thin film}) = \begin{pmatrix} 0 & 0 & 0 \\ 0 & 0 & 0 \\ 0 & 0 & 1 \end{pmatrix}. \quad (2.10)$$

The demagnetizing field is  $\mathbf{H}_d = -N_d\mathbf{M}$  and the demagnetizing energy is

$$E_d = -\frac{\mu_0}{2} \int_V \mathbf{M}\mathbf{H}_d dV. \quad (2.11)$$

The consequence of the demagnetizing field is the shape anisotropy. For example a thin FM layer has its preferred orientation of magnetization in the plane of the film.

**Exchange Energy** Exchange energy responsible for a magnetic order was mentioned and defined in Eq. 2.7.

**Magnetocrystalline Energy** The magnetocrystalline energy is usually small compared to the exchange energy. However, it needs to be considered to find the preferred orientation of magnetization within the sample. Magnetocrystalline anisotropy is the energy necessary to rotate a magnetic moment in a single crystal from the easy axis to the hard axis. It originates in the spin orbit coupling - the easy and hard axis arise from the interaction of a spin magnetic moment with the crystal lattice and the interaction results in a preferred direction of magnetization relative to the crystal axis.

**Stoner-Wohlfart Model** In order to find the magnetization orientation in a magnetically ordered material minimalization of the total energy  $E_{\text{TOT}}$  need to be done. The simplest approximation is the Stoner-Wohlfarth model which assumes a uniform rotation of all spins. In such model the energy functional is simplified since the exchange energy is a constant and does not change when magnetization is rotated.

We assume a thin magnetic film in which the magnetization easy axis is, due to the demagnetization field, in-plane. The anisotropy of the material in plane can be found from energy functional. In the simplest case we assume only uniaxial anisotropy  $K_u$ . We define, in Fig. 2.4, the angles of magnetization, Néel vector and magnetic field used in this work with respect to the sample basis where  $\mathbf{y}$  is the easy axis of the magnetization given, for example, by crystallography direction.

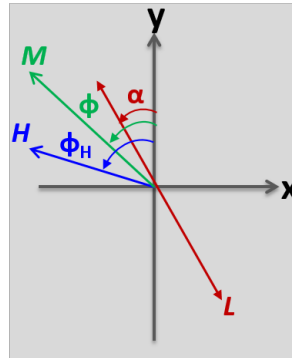


Figure 2.4: Definition of angles of magnetization, Néel vector and magnetic field.

The total energy is

$$E_{\text{tot}} = -\mu_0 \mathbf{H} \mathbf{M} \cos(\phi_H - \phi) + K_u \sin^2 \phi, \quad (2.12)$$

where  $\phi_H$  and  $\phi$  are angles of the magnetic field and magnetization, respectively, and are defined in Fig. 2.4

Within the Stoner-Wohlfarth model the coercive field can be expressed from the Eq. 2.12 as

$$H_C = \frac{K_u}{\mu_0 M_S}. \quad (2.13)$$

## 2.1.2 Exchange Coupling Effect

In the previous chapter we have mentioned the magnetocrystalline and the shape anisotropy. Another source of (unidirectional) anisotropy is a phenomenon called exchange bias or, better, exchange coupling effect (ECE). It was discovered in 1956 by Meiklejohn and Bean [33] when studying FM cobalt particles in an AFM cobalt oxide matrix. They have observed that the magnetization loop is displaced from the center and broadened when it is cooled in a magnetic field from temperature  $T > T_N$ . Although in literature the term *exchange bias* usually refers to both exchange broadening and exchange shift (bias), we will in the following use term *exchange coupling effect* which, in our opinion, better suits as a common term for these two effects. Exchange bias therefore refers only to the shift of the magnetization loop.

A schematic picture of ECE is shown in Fig. 2.5 showing two significant features of ECE: the exchange broadening and the exchange shift (bias) of the  $M(H)$  loop. The exchange broadening  $H_{ec}$  refers to an increase of the coercivity and it is defined as a half of the  $M(H)$  loop width. The exchange bias  $H_{eb}$  is symmetric with respect to zero when cooled in two magnetic fields with an opposite polarity.

The exchange coupling effect persists below critical blocking temperature  $T_B$ . Note that the temperatures at which the exchange broadening and the exchange bias vanish do not need to be identical. For many systems both  $H_{eb}$  and  $H_{ec}$  are non-zero at low temperature. When temperature increases both  $H_{eb}$  and  $H_{ec}$  are decreasing, however, they rarely vanish at the same temperature [34]. Instead, depending on the system parameters, either  $H_{eb}$  or  $H_{ec}$  reaches zero value at lower temperature than the other effect.

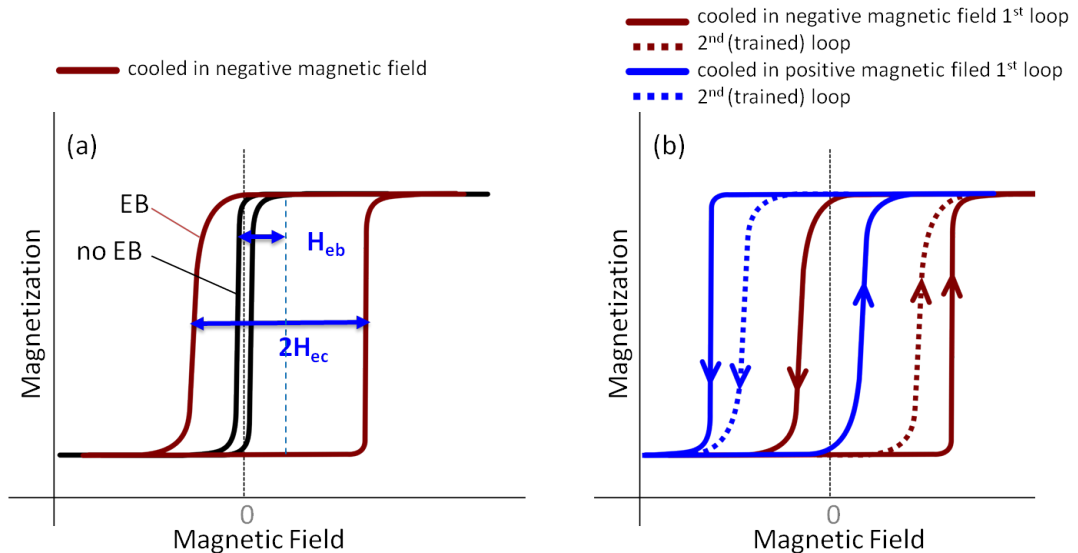


Figure 2.5: Schematic picture of the exchange coupling effect. (a)  $M(H)$  after cooling in negative (red line) field. Clear presence of exchange bias and exchange broadening (indicated by blue arrows) compared to the  $M(H)$  above blocking temperature (black line). (b) Characteristic shape of exchange biased  $M(H)$  after cooling in opposite magnetic fields (blue and red solid lines) disappears after measuring one more loop (training). After training the ECE is weaker but still present (dotted line).

**Systems where ECE is observed** In 1950' the ECE was observed on FM particles in an AFM matrix [33] and it was soon recognized as an interfacial effect. But ECE is not limited only to the interface AFM/FM and it can be present in various systems [35]. For example at ferrimagnet/AFM or ferrimagnet/FM interfaces, but also FM/spin glass [32]. Other studies focused on the effect of disorder on the interface and concluded that imperfections of the interface lead to increasing ECE [36] or that there is no contribution to ECE from atomically flat parts of the interface [37]. Several works studied the effect of interface roughness on  $M(H)$  after field cooling, and it was shown that the shift of the  $M(H)$  loop can be assigned also to roughness of the layer (regardless of coupling to any other adjacent layer).

**Models for Exchange Bias** Various models were proposed for exchange biased systems and several reviews were written on that topic (example [38], [39], [40]). However, currently none of the models seems to be universal and generally accepted. In the following section we give a brief survey of some of the models. In Chap. 3 we will confront them with our experimental observation.

**Meiklejohn-Bean Model** The simplest Meiklejohn-Bean (MB) model describes the new anisotropy as an additional term in Eq. 2.12. It introduces anisotropy  $K_u^{\text{AFM}}$  of the AFM and the effective interface exchange coupling  $J_{\text{EB}}$

$$E_{\text{tot}} = -\mu_0 \mathbf{H} M t_{\text{FM}} \cos(\phi_H - \phi) + K_u^{\text{FM}} t_{\text{FM}} \sin^2 \phi + K_u^{\text{AFM}} t_{\text{AFM}} \sin^2 \alpha - J_{\text{EB}} \cos(\phi - \alpha), \quad (2.14)$$

where  $t_{\text{FM}}$  and  $t_{\text{AFM}}$  are the thicknesses of the FM and AFM, respectively,  $\alpha$  is the angle of the Néel vector  $\mathbf{L}$ . Note that usually the angle of magnetization  $\phi$  and the "angle of antiferromagnetization"  $\alpha$  are expected to be same (collinear coupling).

The exchange coupling constant estimated from MB model is

$$J_{\text{EB}} = H_{\text{eb}} M t_{\text{FM}} \quad (2.15)$$

where  $M$  is magnetization of the FM layer. In the MB model the exchange coupling does not depend on the thickness of AFM layer. The MB model implies that the exchange bias occurs when  $K_u^{\text{AFM}} t_{\text{AFM}} / J_{\text{EB}} \geq 1$ .

The MB model puts strong assumptions on the system. First, it assumes perfect atomically flat interface between AFM and FM layer. Second, it assumes Stoner-Wohlfart model is valid, i.e. both the FM and AFM materials are single domain, the FM is uniformly rotating and the AFM layer is perfectly rigid. Next assumption is that either AFM material is fully uncompensated on the interface (it has a net magnetic moment) [33] or that the AFM is fully compensated but rigidly rotates (all the AFM uniformly) [41]. Last assumption is that the coupling with FM layer is happening on the interface everywhere equally.

The MB model is overestimating the ECE that is measured experimentally. However, the major failure of the model is that it can not explain simultaneous presence of  $H_{\text{eb}}$  and  $H_{\text{ec}}$ . This fact comes from the minimalization of the energy functional in Eq. 2.14. For small values  $K_u^{\text{AFM}} t_{\text{AFM}} / J_{\text{EB}}$  the MB predicts only exchange broadening and for higher values only exchange bias. Experimentally

both effects in the same time are observed as will be discussed in the experimental part.

**Antiferromagnetic Domain Wall - Mauri Model** Several approaches to improve the exchange bias magnitude predicted by MB model were done (summarized for example in [38]). An important contribution was made by Néel [42]. He introduced the idea of an AFM domain wall nucleation when the magnetization reversal is happening. He also calculated that for a very thin AFM layer no exchange bias is observed (only exchange broadening remains).

The AFM domain walls were extensively studied also by Mauri [43]. The Mauri model assumes a single domain FM layer rigidly uniformly rotating in magnetic field and single domain wall AFM coupled to the FM layer. Then, if  $K_{\text{AFM}}$  is small, it is energetically favorable to form a domain wall in the AFM parallel to the interface. It means the AFM moments are 'dragged' by the FM layer as schematically shown in Fig. 2.6.

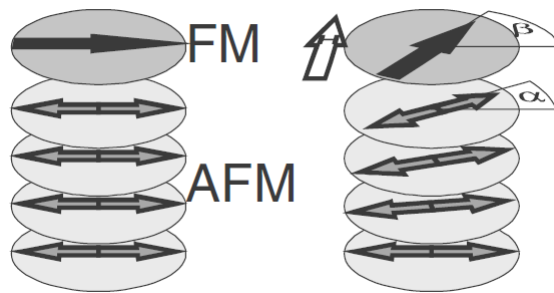


Figure 2.6: A schematic illustration of an AFM domain wall, so called exchange spring effect. [44]

The existence of an AFM domain wall shown in Fig. 2.6 was a key assumption for several models of ECE [42, 43], however, it was confirmed experimentally only later by Scholl [44] who studied X-ray magnetic linear dichroism spectroscopy on single crystal Co/NiO and observed (exchange) spring of the AFM moments. The thickness of the AFM nevertheless plays a critical role if an exchange spring is created.

**Role of uncompensated spins and interface roughness** Both the MB and Mauri models assumed a perfect AFM/FM interface and fully compensated or uncompensated moments on the interface. In 1987 (the same year Mauri published his model) Malozemoff introduced atomic-scale roughness on the AFM/FM interface as a parameter to explain ECE [45]. The frustrated interfaces or defects are responsible for AFM domains formations perpendicular to the interface. This reduces the number of spins contributing to the coupling and the energy of a domain wall has to be added to the energy functional leading to ECE change (stronger or weaker [46]). Also this model was, due to the lack of imaging techniques, confirmed only later [46]. AFM diluted by non-magnetic defects was studied in [46] and they concluded that ECE is dominated by the uncompensated spins from the AFM domain state in the volume that is responsible for the FM/AFM exchange interaction at the interface.

Other works([47, 48]) focused on the role of uncompensated spins on the interface by employing XMCD spectroscopy which is element sensitive and it can therefore separate the contributions from different elements on the interface. They have concluded that the domain wall formation is not crucial for the ECE explanation and that rather the uncompensated spins on the interface are playing the key role. They have shown that a small fraction of uncompensated spins is pinned (and not able to rotate) which is responsible for the shift of the  $M(H)$ . Majority of uncompensated spins can rotate leading to increased coercivity of the  $M(H)$ .

**Radu Spin Glass Model** In the previous model ECE was attributed to the AFM uncompensated spins on the interface. Two types of spins were observed contributing either to exchange broadening or exchange bias. The fact that some of the AFM spins are (due to random frustrated interactions at the AFM/FM interface) free to rotate indicates that such system should be described in terms of spin-glass [49]. Spin-glass model [50] assumes two types of AFM states: first, spins with high anisotropy which holds them pinned; second, AFM states with lower anisotropy which are free to rotate with the FM layer. Schematic figure is shown in Fig. 2.7.

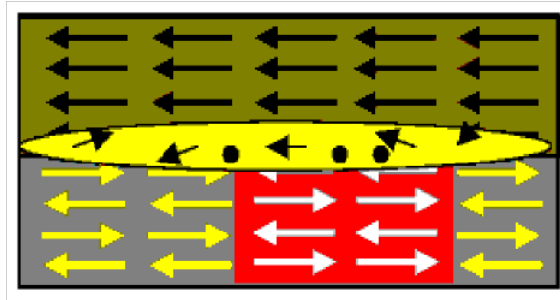


Figure 2.7: Spin Glass Model of ECE. Pinned and unpinned spins. After [39]

Spin glass model gives explanation to the training effect (shown for example in Fig. 2.5) by considering field cooled state only as a local energy minima of a complex SG energy landscape. This minima has a relatively weak energy barrier with a neighboring (deeper) energy minima and the barrier can be easily overcome by applying an external magnetic field (i.e. measuring  $M(H)$ ). It leads to different shape of  $M(H)$  when measured twice (or eventually more). The SG model seems to give good description of the experimentally observed data, recently was extended also to the uncompensated spins coming from the FM material [51].

**Positive Exchange Bias** The exchange bias has a negative sign in majority of systems. It means that the  $M(H)$  loop is shifted towards negative values when cooled in a positive magnetic field. However, it was observed [38] that the interfacial coupling can also have an opposite sign, so called positive exchange bias. An example of a system where positive exchange bias was observed is an interface CoFeB/IrMn [52].

Although lot of work was done since discovery of ECE some questions remain open and the research about the origin of ECE is still discussed. Already the

fact that ECE can be observed in various materials in various forms is indicating that the origin of the effect might not be identical in all the systems and different models and approximations are required to describe different samples. In this thesis the focus is put on manipulating AFM moments, and the exchange bias and exchange spring as one of the tools will be discussed in Chapter 2.

## 2.2 Magnetotransport

In this section we will give a brief overview of the transport properties in presence of a magnetic field (either external or effective spin orbit field). Two types of effects can be observed when a magnetic field is applied to a sample. First, ordinary magnetotransport effects which depend on the external magnetic field  $\mathbf{H}$ . Second, anomalous (or extraordinary) effects which are present in magnetically ordered materials and depend also on the magnetization  $\mathbf{M}$ .

This section has several parts. First we discuss effects with Hall symmetry, including ordinary, anomalous and spin Hall effects. In the next part we discuss the spin galvanic effect which is important for discussion of spin orbit torques. In the next part we discuss the magnetoresistance effects which we present separately for bulk materials and layered systems.

### 2.2.1 Hall Effects

Typical examples of the two categories are the ordinary Hall effect (OHE) and the anomalous Hall effect (AHE). The OHE is a well known phenomenon measured on transverse (sometimes called Hall) contacts. When magnetic field has an out-of-plane component perpendicular to the in-plane current direction the Lorentz force acts on the conduction electrons leading to voltage on the transverse contacts. OHE is measured generally in every material (also in an AFM) [10].

In ferromagnetic materials AHE occurs in addition to OHE. AHE originates in the spin-orbit interaction causing asymmetric scattering of spin polarized electrons leading to an increase of the transverse voltage.

The Hall resistivity  $\rho_H$  can be written as

$$\rho_H = R_0 H_{\perp} + R_e M, \quad (2.16)$$

where  $H_{\perp}$  is the out-of plane component of magnetic field perpendicular to the in-plane current direction,  $R_0$  is ordinary Hall coefficient,  $R_e$  is anomalous Hall coefficient and  $M$  is out-of-plane magnetization component. Beside the well known OHE and AHE a broad family of Hall effects exists. The only other member that will be mentioned here in more details is the spin Hall effect (SHE).

**Spin Hall effect** This effect was theoretically predicted by Dyakonov and Perel [53] and experimentally observed 30 years later [54, 55]. The effect is schematically shown in the left panel in Fig. 2.8. Pure spin current transverse to an applied electric field is generated, and spins up and down are accumulated on the opposite edges of the sample. The ratio between the charge current and the spin current in a material is characterized by spin Hall angle  $\theta_H$ . Importantly, SHE originates in the spin-orbit interaction and therefore the effect is present even

in the absence of a magnetic field. Because equal spin currents flow in opposite direction (spins up and spins down are scattered to the opposite sides) the net charge current is zero. Although the electric Hall voltage can not be measured as in the OHE and AHE case, spin sensitive detection methods were employed to visualize the accumulation of the spins up and down on the opposite edges of the sample, as shown in the right panel in Fig. 2.8.

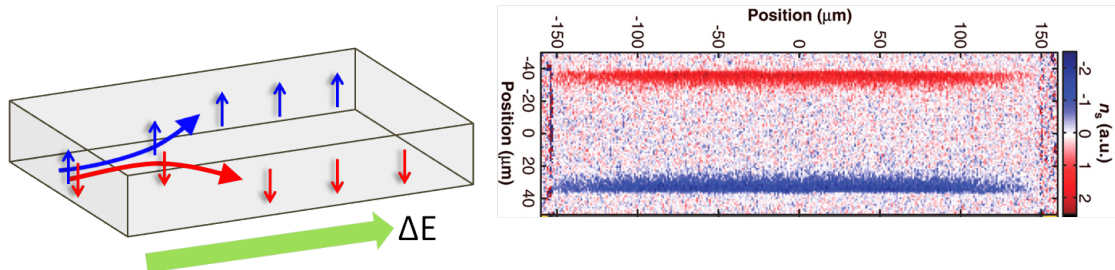


Figure 2.8: Left: Schematic illustration of spin Hall effect. When electric field is applied the spins up and down are scattered to the opposite side of the channel leading to transverse spin polarization. Right: Experimental observation of SHE from [55]. Kerr microscopy was employed to visualize the opposite spins accumulation on the two edges of the sample when electric field was applied.

Detailed microscopic origin of SHE is intensively studied [53, 56]. Some theoretical studies [53, 57] consider SHE as a result of asymmetric scattering of spins up and down (extrinsic SHE). However, also intrinsic SHE was predicted [58, 59]. In this case the effective spin orbit field is momentum dependent which means that the effective spin-orbit field an electron will experience depends on its spin. Therefore a change of electron momentum (by applying electric field) causes change in the effective magnetic field. The spins try to re-align with the field, the direction of tilt is opposite at the opposite sides of the Fermi surface, therefore spin current is present. Note that, unlike extrinsic SHE which relies on SOC at the impurities, the intrinsic SHE should be present also in zero disorder limit.

The inverse spin Hall effect (iSHE) refers to voltage generated between the opposite lateral sides of a sample as a result of a spin polarization.

### 2.2.2 Spin Galvanic Effect

Similar to intrinsic SHE, spin galvanic effect (SGE) [60] is a consequence of spin orbit coupling and asymmetric, momentum dependent, scattering. Due to the SOC the bands in momentum space are split. Due to a spin polarization one band is filled to higher energies. Because of these two ingredients the chance of spin-flip event of an electron traveling in one direction is higher than in the other direction leading to imbalance between the carriers with positive and negative velocity. The consequence is that electric current can be present in a sample without any battery (electric, thermal, concentration gradients etc.).

The inverse spin galvanic effect (iSGE) refers to spin polarization on the opposite sides of a sample as a result of a charge current.

### 2.2.3 Magnetoresistance

Magnetoresistance (MR) is a change of resistance under magnetic field  $\mathbf{B}$  and in principle can be observed in every (conductive) material. Almost every metal exhibit some form of MR regardless if it is magnetic or not [61]. In layered metals or manganite perovskites, the MR is negative (the resistance decreases with applied magnetic field), whereas the MR of a nonmagnetic semiconductor is positive and usually includes physical and geometric contributions [62]. The amplitude of MR increased from several percent to several thousands of percent [63, 64] since its discovery due to technological progress and new materials.

If one considers a spherical Fermi surface with isotropic and energy independent electron effective mass  $m_{\text{eff}}$  the magnetoresistance can not be explained (although the Hall effect can). To describe magnetotransport phenomena observed in real materials presence of electrons with energy dependent  $m_{\text{eff}}$  and/or of scattering time  $\tau$  must be considered. Varying  $m_{\text{eff}}$  results from non parabolicity of bands close to the Fermi level and varying scattering time  $\tau$  is typically for certain scattering mechanism.

Generally, the MR signal is usually given as a relative change caused by magnetic field, typically as

$$\frac{\Delta R}{R} = \frac{R(H) - R(0)}{R(0)}. \quad (2.17)$$

In single-carrier-type semiconductors MR is proportional to  $(\mu H)^2$ , where  $\mu$  is the carrier mobility. High-mobility semiconductors can therefore show relatively large effects [65]. Several MR effects will be measured and discussed in this thesis and are therefore briefly introduced in the following.

#### Anisotropic Magnetoresistance

Anisotropic magnetoresistance (AMR) is a relative change in the resistance as a response to a change in the orientation of magnetization. AMR was the first magnetoresistance effect observed. In 19<sup>th</sup> century Lord Kelvin observed that a piece of iron increased resistance about 1% when magnetic field was applied longitudinally and decreased when applied transversely relative to the current direction. The effect originates in the spin-orbit coupling and is an intrinsic property of the material. This means that AMR is a bulk effect and to observe a MR signal only one layer is sufficient. Phenomenologically AMR has crystalline (cAMR) and non-crystalline (ncAMR) component. The non-crystalline component depends only on the angle between magnetization and current direction as shown in Fig. 2.9, where  $\phi$  is the angle of the magnetization as defined in Fig. 2.4. .

The crystalline AMR originates in the crystal symmetries and it reflects magneto-crystalline anisotropies [66, 67, 68]. Here only the general phenomenological expression for longitudinal ( $\Delta R_{xx}$ ) and transverse AMR ( $\Delta R_{xy}$ ) is given

$$\Delta R_{xx} = r_{\text{nc}} \cos(2\phi) + r_{c1} \cos(2\psi) + r_{c2} \cos(4\psi) + r_{\text{nc,c}} \cos(4\psi - 2\phi) \quad (2.18)$$

$$\Delta R_{xy} = r_{\text{nc}} \sin(2\phi) + r_{\text{nc,c}} \cos(4\psi - 2\phi), \quad (2.19)$$

where the angle  $\phi$  is angle between magnetization and current direction and angle  $\psi$  is angle between magnetization and a reference crystalline direction depending on the measured system. The first term in Eq. 2.18 describes ncAMR, the second

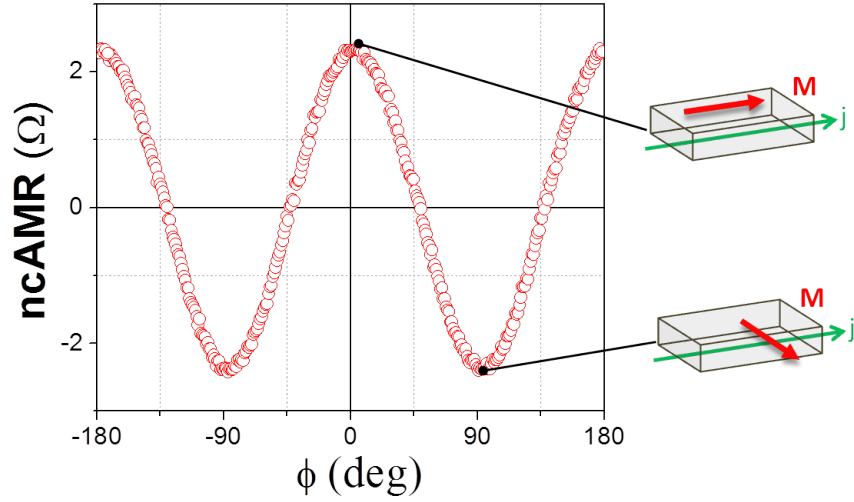


Figure 2.9: Example of non-crystalline AMR. The resistance changes depending on whether the magnetization is parallel or perpendicular to the current direction.

and third are lowest order cAMR terms and the last one is a crossed cAMR, ncAMR term. The higher order terms might exist, however, they are neglected. The Eq. 2.19 describes transverse AMR, where all purely crystalline terms can be excluded due to symmetry arguments and only terms containing ncAMR remain. Note that transverse AMR is sometimes also called planar Hall effect. The symmetry of the effect, however, does not fulfill the Hall symmetry and for this reason this effect is called transverse AMR in this thesis.

## 2.2.4 Magnetoresistance in layered systems

**Giant Magnetoresistance** The large magnetoresistance effect was discovered in 1980' and because of the MR signal of more than 50% it was named giant magnetoresistance (GMR). The effect was almost simultaneously observed in groups of Albert Fert [69] and Peter Grunberg [70] both of whom received the Nobel Prize in 2007 for the GMR discovery. They observed a significant change of the resistance depending on the relative orientation of two adjacent FM layers. A schematic sketch of a GMR device along with the measured variation of the resistance is shown in Fig.2.10 (a). Electric current is applied perpendicular to the interfaces and the resistance varies as a function of relative orientation of the two FM layers (indicated by blue arrows). Relatively strong change of MR signal made the GMR technologically very interesting, the main applications will be in more details discussed in the Sec. 2.4.1.

**Tunneling Magnetoresistance** Tunneling magnetoresistance (TMR) is observed in a system consisting of two magnetic layers separated by a thin insulator which electric current can tunnel through as illustrated in Fig. 2.10 (b). Because the tunneling current depends on the density of states of the two FM layers the final resistance of the magnetic tunnel junction (MTJ) depends on the respective orientation of magnetization of the two FM layers. The effect was discovered in

1975 [71], Fe/GeO/Co tunnel junctions exhibited  $\sim 14\%$  variation of resistance under magnetic field sweep at 4.2 K. Higher quality thin film fabrication and more suitable materials lead to TMR effect at 300 K ([72]) and increased the effect up to  $\sim 1000\%$  ([73]).

Note that in GMR and TMR structures two FM layers, FM1 and FM2, are not switching in the same time due to a different coercivity or because one of them can be pinned by a AFM, as will be also discussed later.

**Tunneling Anisotropic Magnetoresistance** Tunneling anisotropy magnetoresistance (TAMR) is, similar to TMR, based on the tunneling effect through an insulating barrier, as shown schematically in Fig. 2.10 (c). Unlike TMR, TAMR requires only one magnetic layer with strong spin-orbit coupling accompanied by a non-magnetic electrode on the other side of the tunneling barrier. The effect can be observed in materials with anisotropic density of states with respect to the magnetization direction. TAMR was observed for the first time in 2004 in a ferromagnetic semiconductor (Ga,Mn)As [75], later also in a metal structures [74].

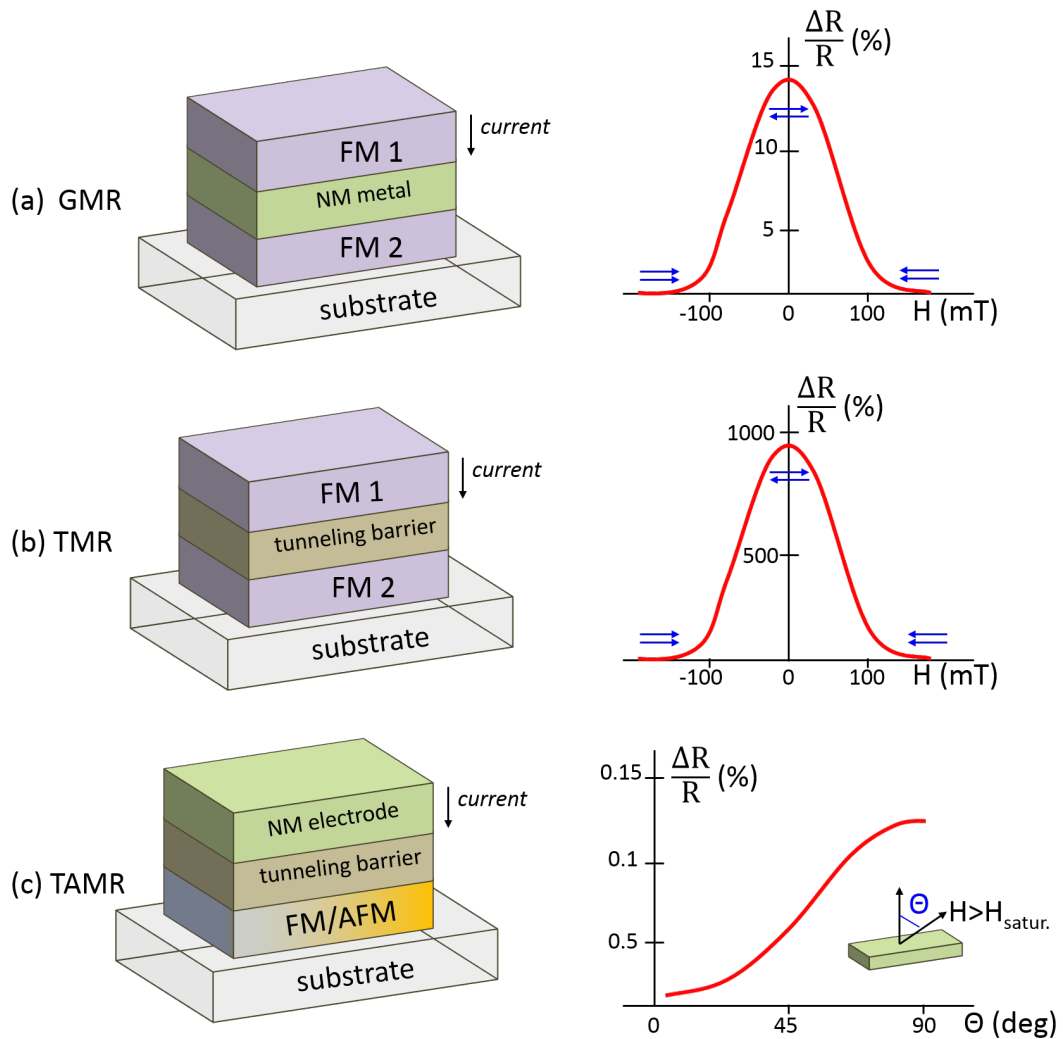


Figure 2.10: Schematic illustration of the magnetoresistance effects in layered systems. (a) Schematic illustration of GMR effect. Two FM layers are separated by a conductive non-magnetic layer. GMR signal during a magnetic field sweep is shown in the right part. Depending on whether the two FM layers are parallel or antiparallel (indicated by small arrows above the measured curve) the GMR signal increases or decreases. GMR signal reaches  $\sim 10\%$  [69]. (b) Schematic illustration of a TMR effect. Two FM layers are separated by a thin insulating barrier. TMR signal during magnetic field sweep has similar dependence as GMR, however, it can reach two orders higher change in resistance [73]. (c) Schematic illustration of a TAMR effect. One magnetic layer and non-magnetic electrode are separated by a tunneling barrier. TAMR variation when strong external magnetic field is rotated is shown in the right part. TAMR signal is typically small [74].

### 2.2.5 Magnetotransport in Antiferromagnets

All effects described above were observed in FM materials and became a textbook matter. In contrast, magnetotransport in AFM is not so well understood yet.

#### GMR

Several theoretical works ([76, 77]) studied the GMR presence in AFM. In the simplest model, where GMR arises from resistivity difference between majority-spins and minority-spins channels, antiferromagnetic GMR (AGMR) cannot be explained because AFM bulk resistivity is spin independent [77]. In case of two AFMs separated by a paramagnetic spacer a shift by half period of the spin density wave corresponds to the difference between parallel and antiparallel configurations. This shift could lead to AGMR, very high quality interfaces are, however, required. Moreover fixing one of the AFM layers is challenging. Experimentally was observed coupling of two AFM layers separated by a thin tunneling barrier [78], however, magnetotransport data were not measured. To summarize, although weak AGMR was predicted [76], no experimental evidence of AGMR or tunneling ATMR was shown so far.

#### AMR

In contrast to GMR, AMR is not an interfacial effect and it originates in the spin orbit coupling. AMR is quadratic in magnetization and therefore FM and AFM coupled spins are indistinguishable. This means that a bulk AFM material can exhibit AMR in case the antiferromagnetic moments can be manipulated as was confirmed by several experimental studies [7, 8].

#### TAMR

In 2010 it was shown theoretically [4] that a single electrode made from AFM material with strong spin orbit coupling can exhibit TAMR due to the anisotropic density of states. This was confirmed also experimentally [5] and it will be discussed in more details in Chap. 3.

#### Hall effects

Recently anomalous Hall effect and spin Hall effect were theoretically proposed in non-collinear metallic AFMs with large spin orbit coupling [79, 80, 81, 27]. To our knowledge, AHE was not experimentally observed in AFM yet [27]. Spin Hall effect was observed in MnPt, IrMn, PdMn and FeMn [82]; spin Hall angle was evaluated and short spin diffusion length  $\sim 1$  nm was observed. Inverse spin Hall effect of CuAu-I-type AFMs was studied experimentally using spin pumping [82].

## 2.3 Thermoelectric effects

Beside the magnetotransport phenomena thermal effects can also contribute to the measured voltage [83, 84]. These effects are not caused by a gradient of electric voltage; instead, they are induced by a thermal gradient. Although the thermoelectric effects are not subject of study in this thesis, some of these effects are contributing to our measurements and need to be taken into account in data analysis. Therefore a brief overview of thermoelectric effects will be given here.

**Thermal AMR** In the same year Lord Kelvin discovered AMR, he also observed the magneto-thermoelectric analog - thermally induced AMR [85]. The thermoelectric power represented by Seebeck coefficient  $S$  is related to the electrical conductivity  $\sigma$  through Mott formula [86, 87] and has generally the same symmetry as AMR if the gradient of electric potential is replaced by a gradient of temperature.

**Nernst Effect** Nernst effect can be interpreted as an analogy of the ordinary Hall effect. When magnetic field and perpendicular thermal gradient are applied to a conductor electric field is induced normal to both. Nernst effect is schematically shown in Fig. 2.11 (a).

**Anomalous Nernst Effect** Anomalous Nernst effect (ANE) is a thermoelectric equivalent of anomalous Hall effect. When a temperature gradient is applied to a ferromagnet and magnetization of the sample is out-of plane, voltage perpendicular to both develops, as schematically shown in Fig. 2.11 (b).

**Planar Nernst Effect** Planar Nernst effect is measured on transverse contacts, but unlike ANE, PNE depends on the angle between thermal gradient and magnetization in-plane of the sample [88, 89]. The angular dependence of PNE is  $\sim \sin(2\phi)$ , therefore it can be interpreted as a thermal counterpart of transverse AMR.

**Spin Nernst Effect** Spin Nernst effect is schematically shown in Fig. 2.11 (c). It is a thermal counterpart of the spin Hall effect, when thermal gradient is applied to a non-magnetic material with high spin orbit coupling, spins up and down are scattered to the opposite side of the channel perpendicular to the applied current. To our knowledge this effect was not systematically measured yet, however theoretical calculation were done [90].

**Seebeck Effect** The Seebeck effect is a well known phenomenon in which a conductor under a temperature gradient generates electric voltage along the thermal gradient. Its efficiency is represented by the Seebeck coefficient  $S$  defined as the ratio of the generated electric voltage to the temperature differences. The best known application of the Seebeck effect is a thermocouple, in which two dissimilar conductors under the same thermal gradient exhibit measurable electric voltage. Seebeck effect is schematically shown in Fig. 2.11 (d).

**Spin Seebeck Effect** The spin Seebeck effect (SSE) refers to an electric voltage detected in a non-magnetic material attached to a ferromagnet under a thermal gradient. The temperature gradient in FM generates spin polarization which enables thermal spin injection to the adjacent NM metal over a scale of several millimeters [91]. The inverse spin Hall effect converts the spin current into electrical voltage, as schematically shown in Fig. 2.11 (e). The macroscopic distance to which pure spin current is injected is many orders of magnitude larger than the spin diffusion length. This makes the SSE very interesting and recently a very actively studied topic [92, 83, 93, 94].

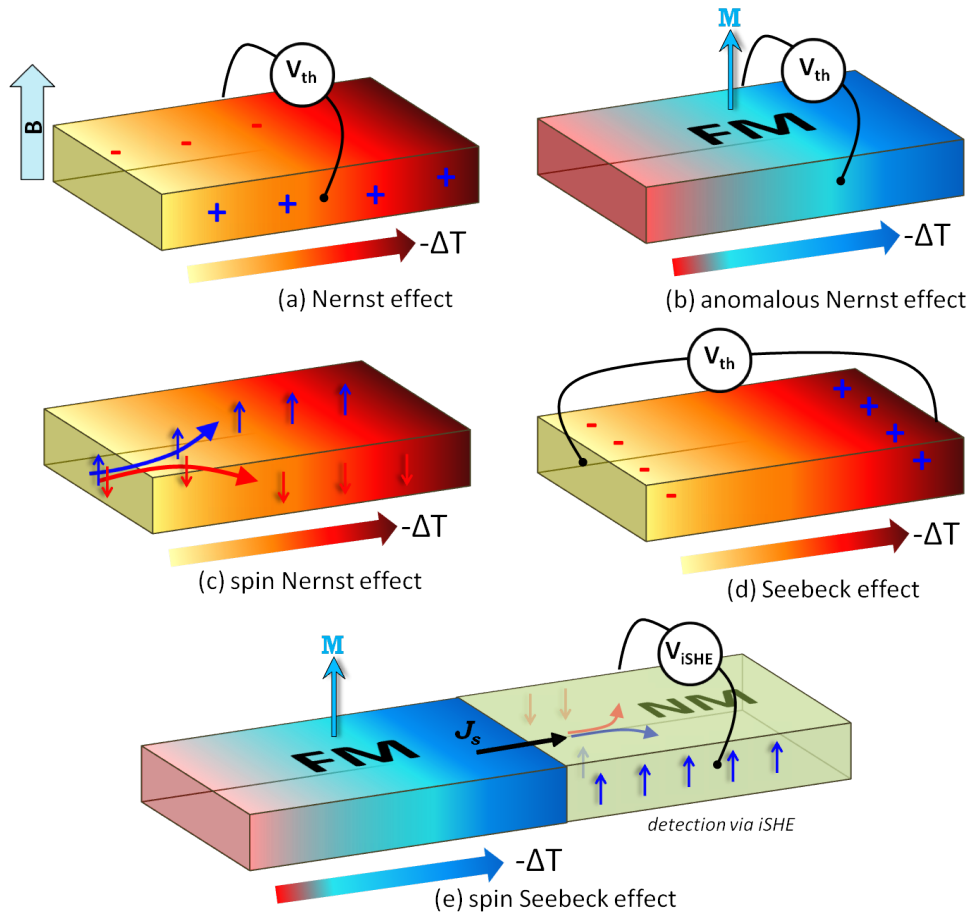


Figure 2.11: Schematic illustration of thermo-electric effects. (a) Nernst effect. (b) Seebeck effect. (c) Anomalous Nernst effect. (d) Spin Nernst effect. (e) Spin Seebeck effect.

Beside the effects shown in Fig. 2.11 a variety of other thermally induced effect exists. One example of more complex thermal effect is Anisotropic Magnetoresistive Heating.

**Anisotropic Magnetoresistive Heating** Anisotropic magnetoresistive heating [95] is not broadly known because of its usually weak strength. However, for certain experiments (for example when strong temperature dependence of resistance is expected) AMR heating should be considered. As mentioned, magnetoresistance describes how the resistance of conductors varies with respect to

the angle between magnetization and current direction. Joule heating is proportional to the resistance of the magnet, therefore the Joule heating depends on the angle between magnetization and current direction.

### 2.3.1 Thermal Effects in Antiferromagnets

Thermoelectric effects in AFM are not systematically described yet. Naturally, all thermal effects independent of the magnetic order are in principle present also in AFM. This includes Seebeck effect or Nernst effect. An AFM attached to a FM under thermal gradient can also exhibit voltage due to the injection of spin current via SSE. As mentioned above, ANE is a thermoelectric equivalent of AHE, therefore could be in principle present in non-collinear AFMs. However, up to our knowledge, no study of ANE in AFM was reported yet.

## 2.4 Spintronics

Spintronics is an intensively studied branch of condensed matter physics that employs not only the electron's charge (as 'traditional electronics' does) but also the electron's spin (giving the name 'spintronics'). Adding the spin degree of freedom would increase significantly the capability and performance of modern electronic devices. The major benefits include increased data processing speed, increased integration density, decreased electric power consumption or non-volatile character of the magnetic memory. Some of the spintronic effects have already found their application. The potential of the spintronics is, however, much bigger and increases with newly observed phenomena [96, 97, 8] and materials [98, 24]. A broad variety of topics are included in the spintronics research, some of the effects were already briefly discussed in the previous chapters. In the following section, the spintronic research areas relevant for this thesis will be summarized and the major challenges discussed. A short introduction into two important spintronic concepts will be given: the realization of a spin valve and the concept of a spin torques. In the last section advantages and disadvantages of antiferromagnetic spintronic will be discussed.

In the simplest picture condensed matter spintronics could be separated into two branches - metallic spintronics and semiconductor spintronics.

**Metallic Spintronics** Utilizing magnetic materials for spintronics has already found its application: GMR and TMR based spin valves are probably the best known examples and they will be discussed in more details. Despite technological orientation of the metallic spintronics, there is ongoing intense development on the basic research level and a lot of new phenomena were discovered. One of the major challenges is to enable control of the magnetization orientation without assistance of an external magnetic fields. This includes control via photonic fields or via spin polarized electric current. The second will be in more details discussed later.

**Semiconductor Spintronics** Semiconductor Spintronics is incorporating the spin degree of freedom to a semiconducting materials. The first obvious advantage, compared to the metallic spintronics, is the compatibility with existing

semiconductor technology. Even more interesting advantage is, however, the potential for combining multiple functions into a single material [99, 100]. Spin transistor logic functionality based on iSHE was recently demonstrated [96] and the major challenges - efficient spin injecting, detection and manipulation - are very actively studied and discussed [101, 102, 103].

Another category of semiconductor spintronics includes materials combining semiconducting and ferromagnetic properties into a single material and, unlike the experiments mentioned previously, the FM injector is not required. An archetypical material representing these properties is diluted magnetic semiconductor (Ga,Mn)As [104, 105, 106, 107], a compound in which Ga atoms are randomly replaced by magnetic  $\text{Mn}^{2+}$ .

Although research on (Ga,Mn)As lead to number of very important spin-related discoveries [75], the low critical Curie temperature and the extrinsic origin of magnetism limit the potential for application. The limited number of ferromagnetic semiconductors is, however, in contrast with a relatively high number of semiconductors with an AFM spin texture, as can be illustrated in Tab. 2.3, some of which have critical Néel temperature well above the room temperature. This observation, fueled by prediction [4] and demonstration [5] of spintronic functionality in AFM materials, lead to increased interest in AFM semiconductors. Experiments made with LiMnAs and the corresponding ab initio calculations [98] served as a pioneering work to demonstrate the semiconducting band structure of I-Mn-V compound in a room temperature AFM prepared by molecular beam epitaxy. The mobility of lithium in LiMnAs, however, makes the material unstable after the exposition to air [98]. Inspired by the first successful experiments with LiMnAs, other materials are now being actively studied. One example is MnTe, antiferromagnetic semiconductor with  $T_N \sim 320 \text{ K}$ , that is well known in semiconductor research [108] and also its potential for AFM semiconductor spintronics is being intensively explored [22]. Another material, which will be in details studied in Chap. 4 of this thesis, is CuMnAs. Both poly-crystalline [109] and epitaxial CuMnAs [24] were prepared and promising results of spintronic functionality were recently confirmed [24, 110].

### 2.4.1 Spin Valve

Spin valve is the simplest functional device which employs spin dependent transport. Typically it is based on some of the MR effects (GMR, TMR, TAMR) and serves as a field sensor or detector of state of a magnetic memory cell. Usually it consists of two FM layers (e.g. alloys of nickel, iron, and cobalt). One of them is a reference FM layer whose magnetization direction is pinned by exchange bias to an AFM (e.g. IrMn). The second - sensor - FM layer is free to rotate. The sensor layer usually has low coercivity therefore can be switched by relatively small magnetic field. The two relative orientations of FM layers - parallel and antiparallel - are representing two memory states "1" and "0". As the magnetizations in the two layers change from parallel to antiparallel alignment, the resistance of a spin valve rises typically from 5 to 10% for GMR-based spin valve and can be as high as 600% for TMR-based spin valves [73].

Although commercially used spin valves are GMR or TMR based, for a spin valve like signal (i.e. two resistance states representing "1" and "0") only one mag-

II-VI	$T_C$ (K)	$T_N$ (K)	III-V	$T_C$ (K)	$T_N$ (K)
MnO		122	FeN		100
MnS		152	FeP		115
MnSe		173	FeAs		77
MnTe		<b>323</b>	FeSb		100-220
EuO	67		GdN	72	
EuS	16		GdP		15
EuSe		5	GdAs		19
EuTe		10	GdSb		27

I-VI-III-VI			II-V-IV-V		
CuFeO <sub>2</sub>		11	MnSiN <sub>2</sub>		<b>490</b>
CuFeS <sub>2</sub>		<b>825</b>			
CuFeSe <sub>2</sub>		70			
CuFeTe <sub>2</sub>		254			

Table 2.3: Survey of magnetic semiconductors. The table shows that in common III-V and II-VI semiconductors AFM ordered spins are more frequent than FM ordered ones. After [24].

netic layer is sufficient, as demonstrated by TAMR based spin valve in (Ga,Mn)As [75]. A schematic picture of the TAMR-based spin valve is in Fig. 2.13. The tunneling barrier is sandwiched between (Ga,Mn)As and top golden electrode. Tunneling resistance is measured when magnetic field is swept along several direction as shown in right panel in Fig. 2.13. The high and low resistances are measured corresponding to a spin valve behavior due to the anisotropic density of states in the material and the two step magnetization reversal process. Switching of the free layer was earlier made exclusively by magnetic fields (for example Oersted field generated by the current in the write line). The magnetic fields are, however, also one of the major drawbacks of this technology. Increasing integration density requires increasing magnetic anisotropy of the free layer in order to prevent them from reversing by a stray field of a neighboring bit or from thermal fluctuation. Increased anisotropy also requires higher magnetic field to write a bit, therefore higher current in the write line, which is energy-wise and size-wise opposite to the desired trend. The exciting development in understanding the spin transfer phenomena, however, brought an elegant alternatives, that will be discussed in the next section.

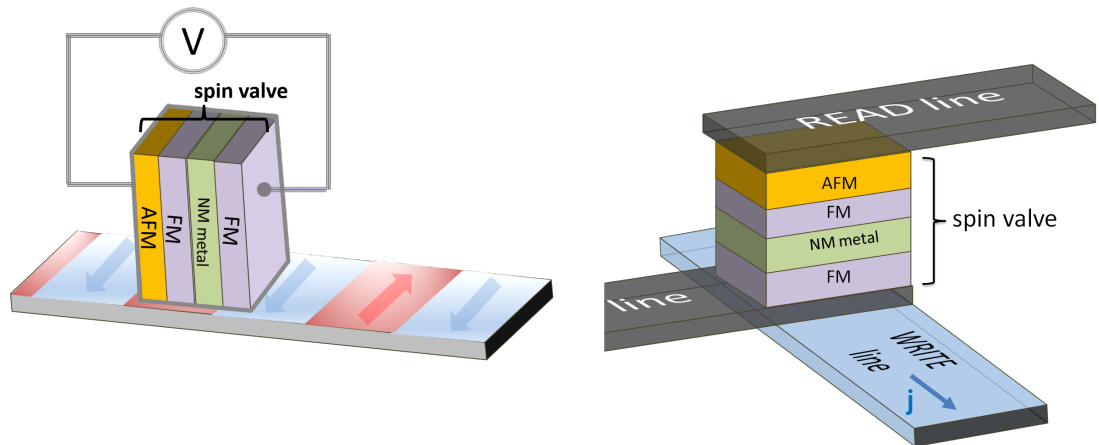


Figure 2.12: Example of an application of a spin valve. Right: Schematic picture of MR sensor (read head). One FM layer is pinned by the AFM and serves as a reference layer. The second one is free (sensor) layer and can detect the magnetization of the hard disk below ("1" and "0" are represented by red and blue stripes). Left: Schematic structure of a GMR based memory cell. The spin valve sensor consists of a FM reference layer and a sensor layer whose direction can be changed. The state of the memory is read by measuring the resistance on the read line, the memory is written by the Oersted field induced by current in the write line.

**Application** Concept of a spin valve has already found its applications, two common devices, a read head and a memory cell, are schematically shown in Fig. 2.12. In a large number of modern computers data are recorded and stored in microscopic areas of a magnetic material in a hard-disk. The information is read by a read head (left panel in Fig. 2.12) as the disk rotates underneath it by sensing the magnetization orientation by a corresponding change of magnetoresistance. GMR, or more commonly used MTJ, due to its high sensitivity to relative orientation of two magnetic layers, allowed to scale the storage density up by orders of magnitude.

Another well known application of a spin valve are magnetic random access memories (MRAM). Compared to the traditional RAM, MRAM are non-volatile and therefore the information is not lost when a computer is switched off.

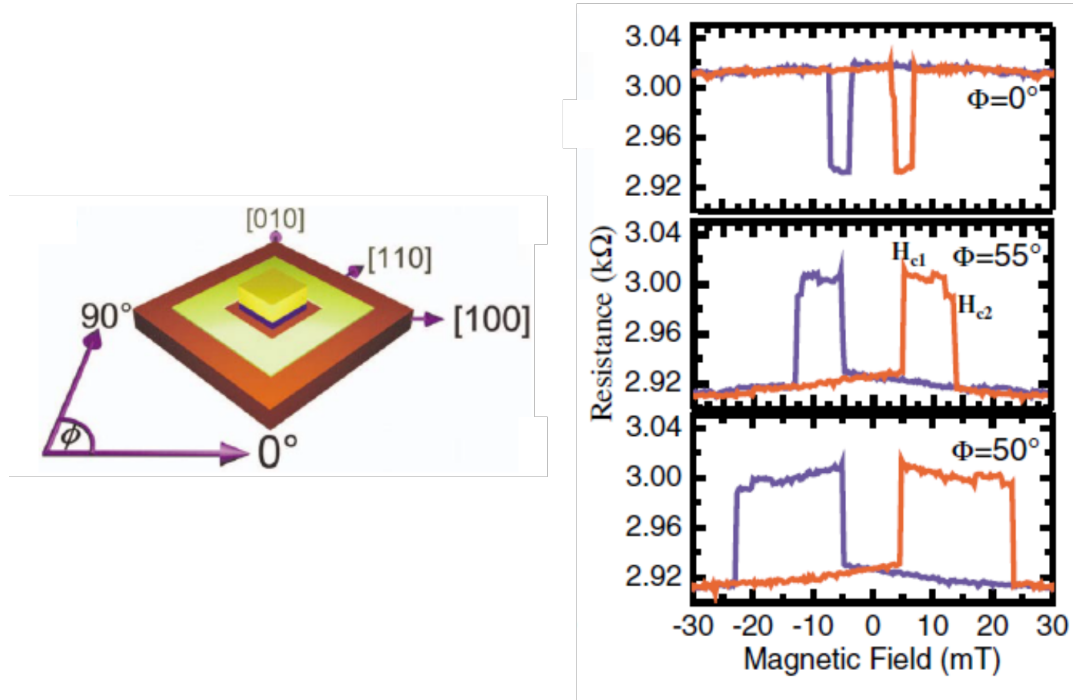


Figure 2.13: Spinvalve based on TAMR. Left: Schematic picture of a (Ga,Mn)As device. Right: Measured spin valve like signal when magnetic field is swept. After [75].

## 2.4.2 Spin Torque

Generally, spin torques are phenomena, in which spins experience a torque that can lead to their tilt or switch. The origin of the torque can be separated into two groups: spin transfer torques (STT) and spin orbit torques (SOT). SOT will be discussed in more details and also systematically studied in Chap. 3. The reason is that, unlike STT which are weak in AFM [76], SOT are predicted to be promising tool to manipulate AFM moments [111], as will be also demonstrated in the experimental part.

### Spin transfer torque

When a spin polarized current enters a magnetic material, angular momentum of a spin polarized electrical current entering a ferromagnet is transferred to the magnetization and it exerts a torque on the magnetization which can lead to its switch. STT mechanism is illustrated in Fig. 2.14. STT can be understood as the inverse effect of a current becoming polarized by passing through a FM because of the spin dependent scattering. There are various techniques used to generate STT as optical pumping[112], ferromagnetic resonance [102] or current polarization by a FM layer as shown in the left panel in Fig. 2.14. STT enabled development of spin-logic devices and STT-RAM [113] that are since 2012 commercially available.

### Spin orbit torque

Spin orbit torques are based on relativistic spin orbit coupling and are schematically illustrated in Fig. 2.15. Spin orbit torques mechanism was observed much

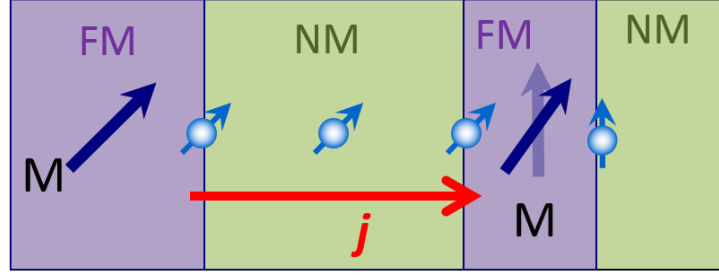


Figure 2.14: Schematic illustration of current induced spin transfer torque. Electric current is polarized by the first FM layer (small blue arrows). The spin polarized current transfers the angular momentum to the magnetization in the second FM layer leading to the tilt of the magnetization.

later than STT [114, 97, 115], the origin of SOT and its relationship with material properties are still very actively studied [113, 116, 117, 118, 119, 120, 121, 122, 123, 124]. Similar to STT, there are multiple techniques that successfully generate SOT, as optical spin orbit torque [125], FMR resonance [126] and current induced spin orbit torques. SOT, in contrast to STT, does not require spin polarized current injected to FM. Instead, the intrinsic properties of the material can cause a torque on the magnetization. The important requirement for SOT is a system with inversion asymmetry including materials with strong spin orbit coupling (SOC), as was demonstrated in (Ga,Mn)As [114]. High current density is sent to a material with strong spin orbit coupling. The charge current couples to the spin and due to SOC a non equilibrium electron spin density is generated exerting a torque to the magnetization.

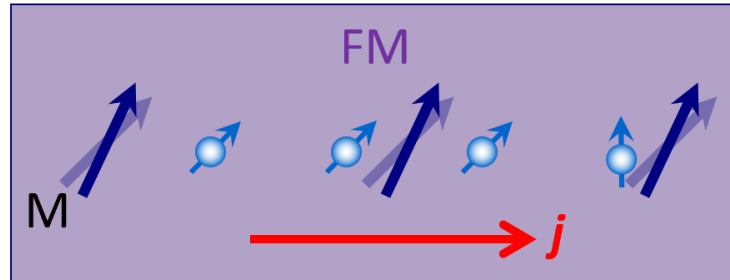


Figure 2.15: Schematic illustration of current induced spin orbit torque. The polarization layer is not required, broken inversion symmetry in the material can induced effective fields that lead to magnetization switch.

Electric control of magnetization is, however, especially appealing for materials used in commercial devices mostly consisting of ferromagnetic metals without any structural asymmetry. Therefore it attracted a lot of attention when magnetization was switched in a thin FM layer in contact with a non-magnetic metal with high SOC [97, 115]. Although the interpretation was different (and the research is still ongoing), the common property of these two experiments is the broken inversion symmetry, not in the bulk as in (Ga,Mn)As, but on the FM/NM interface. According to recent understanding of SOT, two effects are contributing:

**1. SOT generated by SHE** First mechanism, used to explain switching in [115], is based on generation of spin current in the NM material due to the spin Hall effect, as schematically shown in left panel in Fig. 2.16. The spin current is injected into the FM layer and leads to magnetization reversal. Note that mechanism of spin polarized current injection would be in principle similar to STT, however, SHE originates in spin orbit coupling and therefore this mechanism also belongs to the group of SOT.

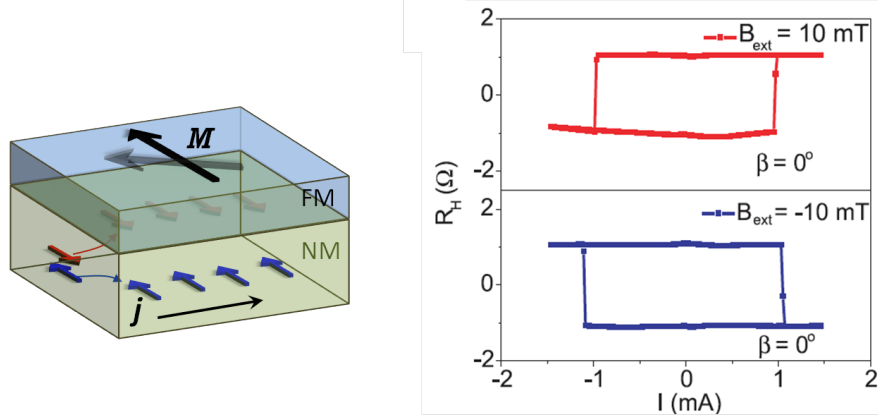


Figure 2.16: Left: Schematic picture of SOT. Spin current is generated due to SHE in non-magnetic metal and after is injected to FM layer leading to magnetization reversal. Right: Magnetization reversal due to SHE in Ta measured in Ta/CoFeB system, after [115].

**2. SOT generated by inverse spin galvanic effects** Second mechanism behind SOT is caused by the inverse spin galvanic effects [97, 116, 118, 121, 124] that are result of spin-orbit interactions (as Rashba interaction [127] or Dresselhaus interaction [128]). These effects are present in systems with SOC and broken inversion symmetry, for example by interface of two materials. This leads to spin redistribution and net spin polarization which can generate effective fields  $H_{\text{eff}}$  that act on the magnetization of the FM layer similarly as an external applied field. This can lead to the magnetization tilt or reversal.

In a particular system SOT can be generated by iSGE, SHE, or both. Which of the mechanisms is dominant is intensively studied and several experimental methods to distinguish the mechanisms were proposed. One approach is to study thickness dependence of the non-magnetic layer underneath the FM one [116]. Generation of SOT via SHE requires certain thickness of the non-magnetic material in order to build up the spin current. In contrast, iSGE is generated on the interface NM/FM and should not depend on the NM thickness. Another approach to distinguish the origin of SOT is to study their symmetry under magnetic field rotation [118, 123]. This method was also studied in this thesis and will be discussed in Chap. 3, here only a brief summary of the torque symmetries is given.

**Symmetry of SOT** We assume a structure in Fig. 2.17. Symmetry is broken in z-axis by the interface, current is along x-axis and  $\mathbf{m}$  is magnetization direction vector. Spin accumulation on the NM/FM interface can be either transverse to the current generating a transverse effective field  $H_{\text{eff}}^{\perp}$  [97] or longitudinal generating a longitudinal effective field  $H_{\text{eff}}^{\parallel}$  [129]. The transverse effective field does not depend on the magnetization and it is perpendicular to x-axis and z-axis, therefore  $H_{\text{eff}}^{\perp} \sim y$ . The longitudinal effective field is perpendicular to the magnetization  $H_{\text{eff}}^{\parallel} \sim \mathbf{m} \times y$ .

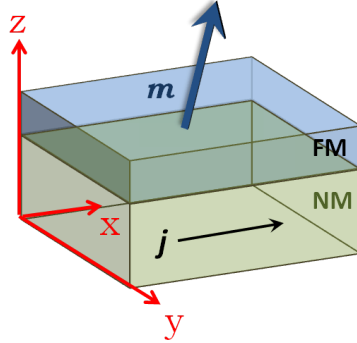


Figure 2.17: Definition of directions for SOT symmetry.

The torques corresponding to the effective fields are

$$T_{\text{field-like}} \sim \mathbf{m} \times y \quad (2.20)$$

$$T_{\text{antidamping-like}} \sim \mathbf{m} \times (y \times \mathbf{m}). \quad (2.21)$$

The corresponding effective fields are called field-like (independent of magnetization) and antidamping-like (depending on the magnetization).

### 2.4.3 Ferromagnetic and Antiferromagnetic Spintronics

Relatively long history of FM spintronics and the ability to manipulate FM materials by an external magnetic field made ferromagnets essential part in majority of spintronic applications. They are, however, reaching some of their limits. From the application point of view metallic FM, present in magnetic memory and logic, are suffering mainly by increasing integration density. To prevent magnetic bits from reversing each other high stability of a single FM bit and small stray field is required. Stability can be improved by increasing the coercive field, however, this requires higher magnetic field or STT to switch the bit and therefore increases energy consumption. From the semiconductor spintronics point of view, the major drawback is the lack of room temperature ferromagnetic semiconductors and the extrinsic origin of ferromagnetism.

Some of these disadvantages could be overcome if AFMs are used instead. The major advantages of AFM is the absence of a stray field and the relative insensitivity to an external magnetic field or radiation. Hence, the integration density, unlike for FM, is not limited. Another advantage is that the switching

of antiferromagnetic moments is supposed to be faster than in case of ferromagnetic moments [111] and less energy consuming. When combining magnetic and semiconducting properties in one material, AFMs are more likely to keep the semiconducting properties. The reason is that in FM exchange splitting tends to lower the energy gap, as is illustrated in Fig. 2.18.

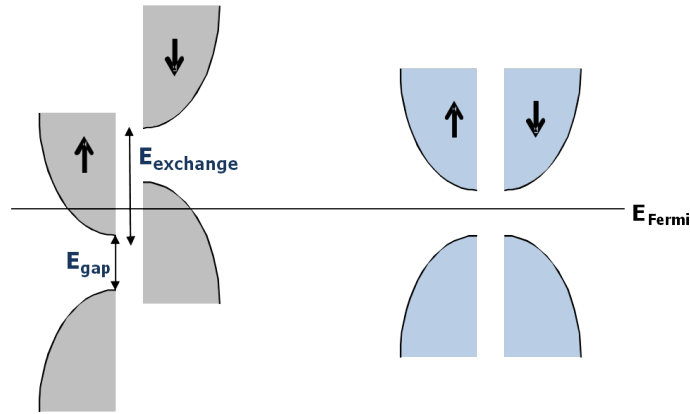


Figure 2.18: Schematic picture why AFM semiconductors are more favorable than FM semiconductors. After [98]

Compared to FM spintronics, the AFM one is not so well explored yet, however, several phenomena known from FM, as AMR [7], TAMR[5] or spin Hall angle [82], have been found to be present also in AFMs, and other effects, as SOT [111] or AHE [81], are predicted. Some of other phenomena, as thermoelectric effects or resonance effects in AFM, are described incomparably less than in FM or not at all. Beside all the advantages, AFM also suffer by some disadvantages. The same properties that make AFMs appealing for applications are, however, also bringing several challenges to the AFM spintronics. One of the most important is the way of manipulation of AFM moments that was not systematically studied yet. Another open questions is fabrication of high quality AFM semiconductor and a proof of its spintronic functionality.

# 3. Manipulation of the Antiferromagnetic Moments

## 3.1 Concepts to Manipulate AFM Moments

The major goal of this chapter is to study ways of AFM moments manipulation.

We have employed three techniques which enable AFM moments manipulation. First, we focus on the exchange spring effect and we study behavior of the AFM in a coupled system IrMn/NiFe. This method relies on the FM layer which is used as a tool to manipulate the AFM moments. In the next step we remove the FM layer and we study the manipulation of AFM moments by cooling in an external magnetic field through the critical temperature  $T_N$ . When a magnetic field during the cooling process is applied along different crystallographic directions, AFM moments can be oriented and aligned in different orientations. Different orientation of AFM moments results in varying TAMR signal.

We have employed magnetometry and TAMR as detection tools of magnetic moments orientation [5, 6] in the two previously described methods. Although magnetometry is primarily sensitive to the FM layer and TAMR is sensitive to the AFM layer we have shown that TAMR and magnetometry data can be correlated.

The last studied technique is based on current induced torques acting on AFM moments. We have prepared nanostructures comprising an ultrathin AFM which enabled measurements above and below  $T_N$ . For detection of current induced torques we have employed second harmonic technique, which detects sensitively non-ohmic variations of measured resistance.

Magnetic and transport properties of the samples are studied. More details about the used instruments can be found in Appendix A.1. Magnetic properties of the samples were measured in Quantum Design Superconducting quantum interference device (SQUID) MPMS XL-7. Transport properties were studied in Quantum Design Physical Property Measurement System (PPMS) and Oxford Instruments (OI) cryostat with a 3D vector magnet.

## 3.2 Materials and Structures

Materials and samples used for AFM moments manipulation will be summarized in this section and their magnetic and structural properties will be presented.

### 3.2.1 IrMn Antiferromagnet

The AFM material present in all discussed nanostructures is  $\text{Ir}_{0.2}\text{Mn}_{0.8}$ . This material was selected as a typical representative of AFM that is widely used and grown also for technology applications. A phase diagram of Ir-Mn is shown in Fig. 3.1. Ir-Mn alloys exist in several stable configurations depending on the Mn percentage and temperature; the chemically ordered phase  $\text{IrMn}_3$  reaches the highest critical temperature, ranging between 730 K [23] to 1000 K [26]. If grown in thin films, it has the same triangular magnetic structure as bulk  $\text{IrMn}_3$  [26].

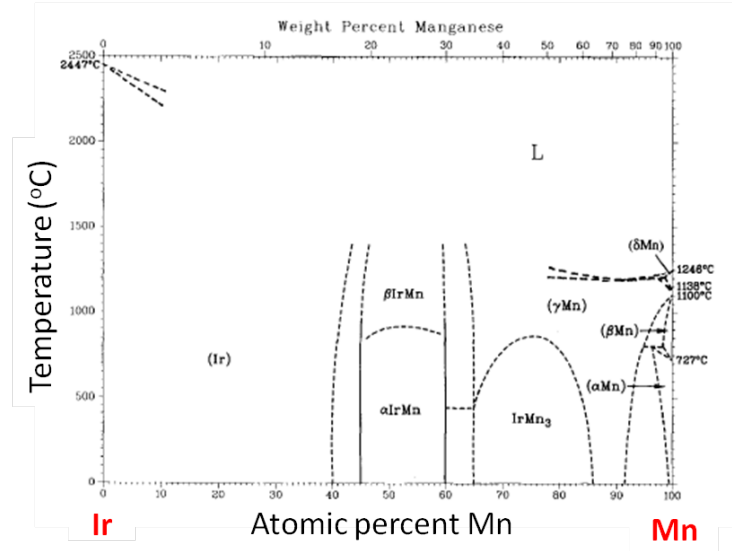


Figure 3.1: Phase diagram of Ir-Mn alloy. After [130].

The chemically disordered IrMn has magnetic moments tilted from the crystal diagonals [26], and the critical temperature of the material is reduced approximately to the range between 650 K [23] - 730 K [26]. The chemically disordered  $\text{Ir}_x\text{Mn}_{1-x}$  ( $x$  ranging 0.15-0.25) is preferred for magnetic storage applications because of large exchange fields and high thermal stability. It is important to note that the critical temperature  $T_N$  of ultra thin films (below 3 nm) of IrMn can be further reduced to values below room temperature [7].

### 3.2.2 Layered Structures

All samples studied in this chapter consist of polycrystalline layers prepared by UHV RF magnetron sputtering in base pressure  $10^{-9}$  Torr on a thermally oxidized silicon substrate with  $\sim 100 - 700$  nm  $\text{SiO}_2$  layer or on  $\text{SrTiO}_3$  substrate. Magnetic field of 0.4 T in the sample plane was applied during the growth. The basic structures studied in this thesis are schematically shown in Fig. 3.2. Layered materials were prepared according to our requirements by Hitachi, Japan and LNESS Como, Italy. Complete list of measured samples can be found in Appendix A.2 and is schematically shown in Fig. 3.2. The layered structure in Fig. 3.2 (a) is used for exchange spring study, the important property is exchange coupling on the AFM/FM interface. The layered structure in Fig. 3.2 (b) is used for AFM moment manipulation by cooling in magnetic field, the important characteristic is thin IrMn film with reduced  $T_N$  and absence of FM layer. The layered structure in Fig. 3.2 (c) is used for study of current induced torques, the important characteristic are thin metallic layers. The choice of materials and layer thickness is summarized in the following:

**Ta/Ru layer** Common recipe started from buffer layers of Tantalum and Ruthenium (typically  $\sim 60$  nm) to smooth the interface. The buffer layer was critical for sample fabrication into tunnel junctions (for TAMR) and for the IrMn thickness study. For current induced effects experiments it was, however, critical to achieve

a high current density. Therefore the buffer layer thickness had to be reduced to only thin (2-5 nm) Ta.

**FM layer** The choice of FM layer was also different for various experiments. The interface IrMn/NiFe is known for high and well defined exchange coupling. For this reason, IrMn/NiFe system was selected to study the exchange spring and the role of temperature and IrMn thickness. The NiFe thickness was fixed to 10 nm in all exchange spring experiments, the easy plane of the material was in-plane. In contrast, for current induced effects out-of-plane anisotropy of the FM layer is preferred and thin layers are required to achieve high current density. Therefore thin CoFeB layers, known to have out-of-plane anisotropy [131], were prepared. IrMn/CoFeB interface is known for weak and positive exchange coupling [52] as was also confirmed in our samples. A strong exchange coupling is, however, not required to study current induced torque, as will be discussed in the Sec. 3.6.

**oxide and capping layers** The MgO oxide layers were sputtered from a target under pure Ar atmosphere with pressure of 10 mTorr and annealed after the growth to achieve crystalline structure of MgO [5, 6, 7]. The MgO oxide layer served either as a tunneling barrier in case of the TAMR experiments or as a capping layer to protect the metallic layers. Wafers that were further processed for TAMR devices were capped by a Pt layer which served as the second electrode on the other side of the MgO barrier. Unpatterned samples which were measured in SQUID did not contain Pt layer. Wafers grown for current induced torque effects experiments (Fig. 3.2 (c)) contained also  $\text{AlO}_x$  layer to protect the ultrathin metallic layers below.

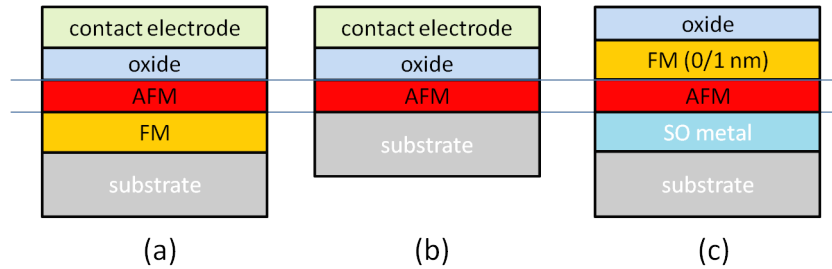


Figure 3.2: Schematic compositions of samples measured in this chapter. (a) Samples used for manipulation of AFM moments by exchange spring, (b) stack of layers used to manipulate AFM moments by cooling in magnetic field, (c) samples used to study current induced effect on AFM.

### 3.2.3 Device Fabrication for Magnetotransport

**TAMR devices** Tunnel junctions were patterned in Hitachi, Japan and LNESS, Como. In order to define the MTJs for electrical measurements, mesa structures of  $1 \times 2 \mu\text{m}^2$  -  $5 \times 10 \mu\text{m}^2$  were patterned from the wafer by photolithography and ion milling. After device fabrication, wafers were annealed at  $350^\circ \text{C}$  for 1h in a  $10^{-6}$  Torr vacuum in a magnetic field of 0.4 T applied along the same direction as during the growth.

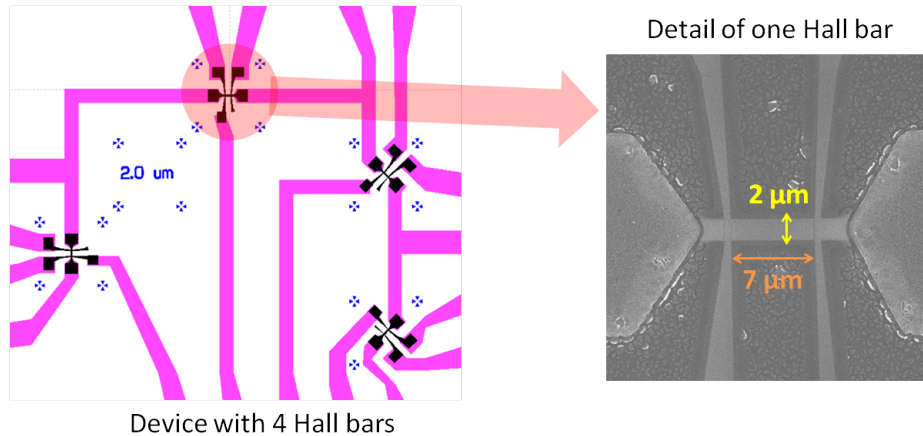


Figure 3.3: Design of a device consisting of 4 Hall bars rotated by  $45^\circ$  to each other and a SEM image of one Hall bar with dimensions indicated in the picture.

**Hall bars** Current induced effects were studied on Hall bars patterned from wafers fabricated in Hitachi, Japan. Details about lithography processing can be found in Appendix A.4. An example of a device design and a SEM image of a Hall bar are shown in Fig. 3.3. Four Hall bars were fabricated in each device in order to measure simultaneously multiple Hall bars with different angles between magnetic field and current. The width of a Hall bar is  $2\ \mu\text{m}$ , the distance between the longitudinal contacts is  $7\ \mu\text{m}$ . Samples were tested on a probe station before they were glued and wire-bonded to a chip carrier or PCB.

### 3.3 Samples characterization

#### 3.3.1 X-Ray Diffraction and Reflectivity

All wafers were characterized by X-Ray reflectivity (XRR) and X-Ray diffraction (XRD). XRD determines the crystal quality and orientation. XRR gives information about thickness of the particular layers and interfacial roughness. Special care was taken to analyze data measured on ultra-thin films (stack of layers in Fig. 3.2 (c)) which will be discussed in more details in the last paragraph of this section.

**XRD characterization** XRD characterization was done by X. Marti and V. Holy (Charles University, Prague) and D. Kriegner (JKU, Linz). XRD was used to verify the out-of-plane texture of the films as shown in Fig. 3.4; the IrMn and NiFe layers are (111) out-of-plane oriented, Ru and Ta are (001) and (110) oriented, respectively. In the plane of the layers the samples are polycrystalline. The MgO insulating barrier has a pronounced [001] out-of-plane texture (preferred orientation of individual crystals), while the IrMn layer shows strong [111] texture, as was also confirmed in previous works [5].

**XRR Characterization of ultra-thin layers** To confirm the nominal thickness of the ultra-thin layers several methods were employed. The main characterization was done by careful XRR measurement and analysis by D. Kriegner and

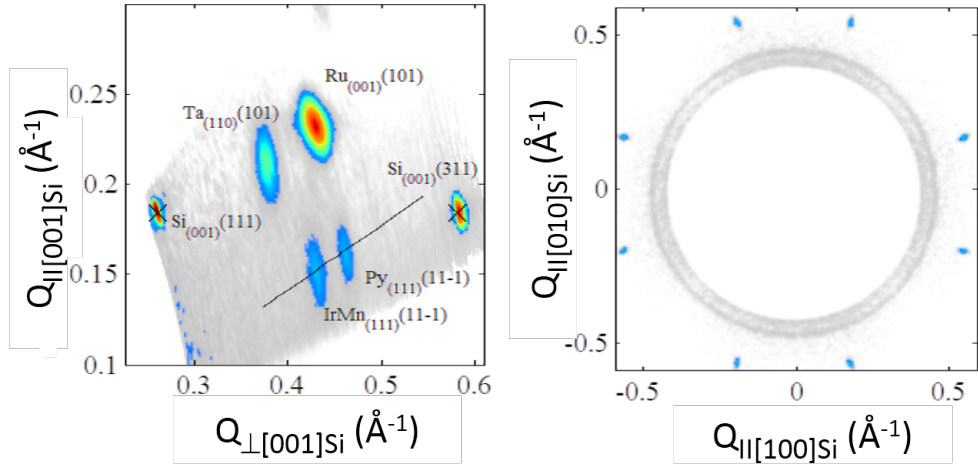


Figure 3.4: Material characterization by XRD. Measured sample stack shown in Fig. 3.2 (a). Left: All individual layers show out-of-plane texture as indicated in the labels of the XRD peaks. Right: Data show that the layers are polycrystalline with no preferred in-plane orientation. Measured by X. Marti (unpublished).

V. Holy (Charles University, Prague), the obtained data were in agreement with X-Ray fluorescence measured on one particular sample by B. Kaerstner (PTB, Berlin). The ultrathin magnetic layers were also studied by SQUID magnetometry, as will be discussed in the next section. XRR measurements were performed using a laboratory diffractometer with Cu radiation. The layer thickness determined by XRR is: Ta( $2.2 \pm 0.2$  nm)/IrMn( $0.6 \pm 0.3$  nm)/CoFeB( $0.9 \pm 0.2$  nm)/MgO( $1.4 \pm 0.2$  nm) capped with 10 nm of  $\text{AlO}_x$  for sample with CoFeB and Ta( $5 \pm 0.2$  nm)/ IrMn( $1.3 \pm 0.3$  nm)/MgO( $1.4 \pm 0.2$  nm)/ $\text{AlO}_x$ (10 nm) for sample without CoFeB. The root mean square roughness of all interfaces is 0.15 – 0.3 nm. XRR simulations are performed using the Parratt formalism [132] shown in Fig. 3.5. Omitting any of the five distinct layers in the simulation would not allow to fit the measured data.

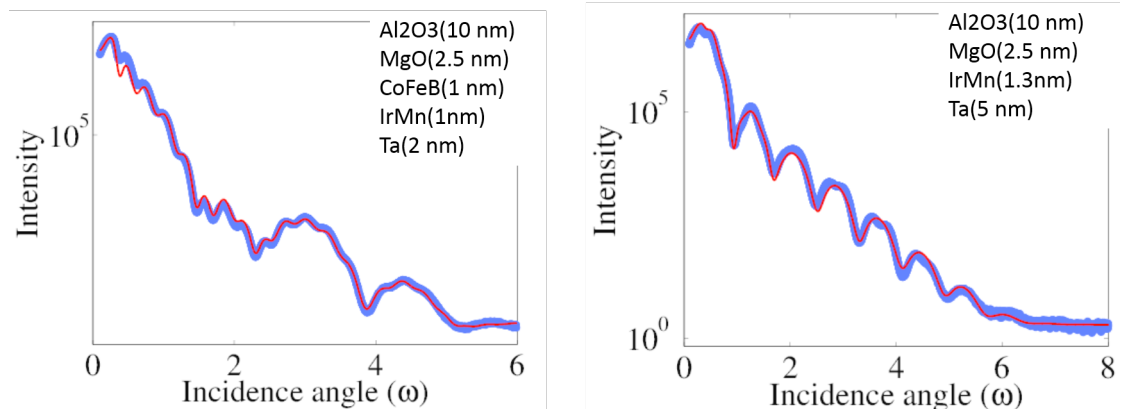


Figure 3.5: Material characterization. X-Ray reflectivity measurement (blue dots) and simulation (red line) of the sample with CoFeB in the left panel and without CoFeB in the right panel. Measured by D. Kriegner (unpublished).

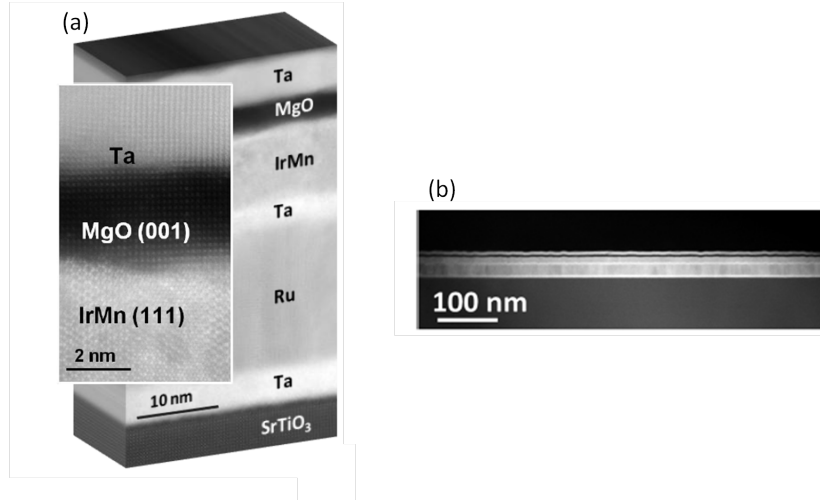


Figure 3.6: STEM image of stack of layers with low and high resolution to confirm the high quality of the layers. Left: Details of the interfaces. Right: Distinct interfaces over large distance. After [7].

### 3.3.2 Scanning Probe Microscopy

The wafers were characterized by Atomic Force Microscopy (AFM) in order to obtain the roughness of the surface and the homogeneity of the wafer. AFM measurements were carried out by group in LNESS Como. AFM analyses at intermediate growth steps revealed that each new layer preserved the RMS roughness of less than 1 nm. The high structural quality of the heterostructures was confirmed by STEM, an example of STEM images taken by M. Varela (Oak Ridge National Laboratory) is shown in Fig. 3.6. This particular image is taken on a sample from the batch schematically sketched in Fig. 3.2 (b). Low and high resolution STEM Z-contrast images show that the stacking comprises continuous films over large distances.

### 3.3.3 Magnetometry

All wafers were characterized by SQUID magnetometer prior device fabrication to confirm the expected magnetic properties. SQUID magnetometry was in particular important tool to study the exchange spring effect as will be discussed in more details later. In this section we will show the exchange coupling presence on IrMn/FM interfaces and we will discuss the effect of annealing on the exchange coupling effect. Wafers containing only IrMn (no FM) were also measured in SQUID prior device fabrication in order to confirm zero net magnetic moment.

#### Exchange Coupling at IrMn/FM Interface

Exchange coupling effect (consisting of increased coercivity  $H_{ec}$  and exchange bias shift  $H_{eb}$ ) was introduced in Chap. 2.1.2 for a general AFM/FM interface. Exchange coupling is, however, very sensitive to material selection, layer thickness, temperature, interface roughness and other parameters. Therefore a systematic magnetometry measurement of every sample was performed to confirm the coupling of the FM layer with IrMn. Interface between IrMn/NiFe is well known for

a strong exchange coupling. Typical thickness of IrMn in such bilayer is  $\sim 10$  nm leading to high IrMn anisotropy. Exchange coupling at the AFM/FM interface is present, however, due to the strong anisotropy of thick IrMn, the exchange coupling effect is reduced to exchange bias shift only. The exchange coupling is however present also for thinner IrMn; in this case the coupling between FM and AFM has two consequences, one is exchange bias and the second is exchange broadening. It is important to note that the blocking temperature  $T_B$ , at which the exchange coupling disappears, is not identical for  $H_{ec}$  and  $H_{eb}$  and therefore two critical blocking temperature may exist.

**Symmetry of Exchange Coupling Effect** An important characteristics of exchange coupling effect is its symmetry with respect to the direction of magnetic field cooling. IrMn/NiFe samples were grown in magnetic field, thus preferred direction of magnetization was set and samples exhibit exchange coupling effect also when cooled in zero magnetic field, as can be seen in Fig. 3.7 (black line). The main difference is, however, in the shape of magnetization loop, when a sample is cooled in magnetic field a typical asymmetric shape of the hysteresis loop occurs (blue line in left panel in Fig. 3.7). This asymmetry does not persist after training.

When IrMn/NiFe interface is cooled down in positive magnetic field the shift of the magnetization loop to negative values should be identical as shift to the positive values after cooling in negative magnetic field. The starting temperature for cooling in field needs to be higher than the critical  $T_N$  in order to achieve a symmetric exchange bias. This can be used to roughly estimated  $T_N$  of a thin AFM film as seen in Fig. 3.7. Two samples were cooled in magnetic field  $+0.3$  T and  $-0.3$  T from 400 K. The sample with 5 nm IrMn exhibit symmetric exchange bias at low temperature as shown in the left panel. The sample with 10 nm IrMn, however, does not exhibit symmetric exchange bias at low temperature, as shown in the right panel. This can be explained by reduced  $T_N$  of thinner IrMn to vicinity of 400 K while  $T_N$  of 10 nm thick IrMn is well above 400 K.

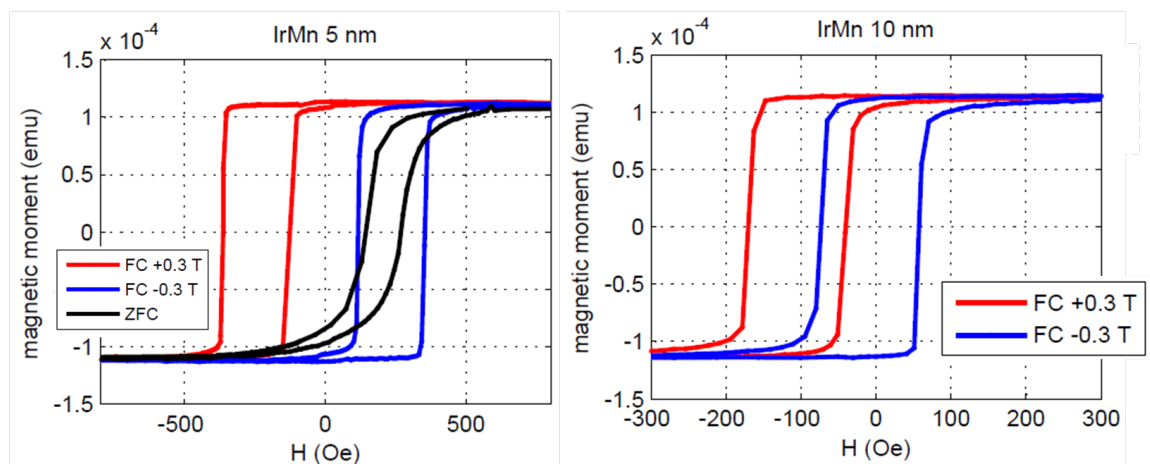


Figure 3.7: Symmetry of exchange bias as a function of IrMn thickness. Samples were cooled in  $\pm 0.3$  T from 400 K. Left: 5 nm thin IrMn sample exhibit symmetric EB. Right: 10 nm thick IrMn does not show symmetric EB.

**Effect of Annealing on Exchange Coupling Effect** Samples were annealed at 350° in order to increase the exchange coupling effect on the IrMn/NiFe interface. The effect of annealing on exchange coupling is shown in Fig. 3.8. A wafer comprising IrMn(5 nm)/NiFe was divided into four parts; one part remained as grown and three parts were annealed at different temperatures (270°C, 300°C, 350°C). A sample from each quarter was afterwards measured in SQUID, the results are shown in Fig. 3.8. It can be seen that both  $H_{ec}$  and  $H_{eb}$  increase with the increasing annealing temperature, the strongest effect is after annealing at 350°. Similar increase of exchange coupling was observed for all measured samples, in Fig. 3.8 (b),(c) three examples are shown (IrMn thickness 4 nm, 5 nm and 7.5 nm).

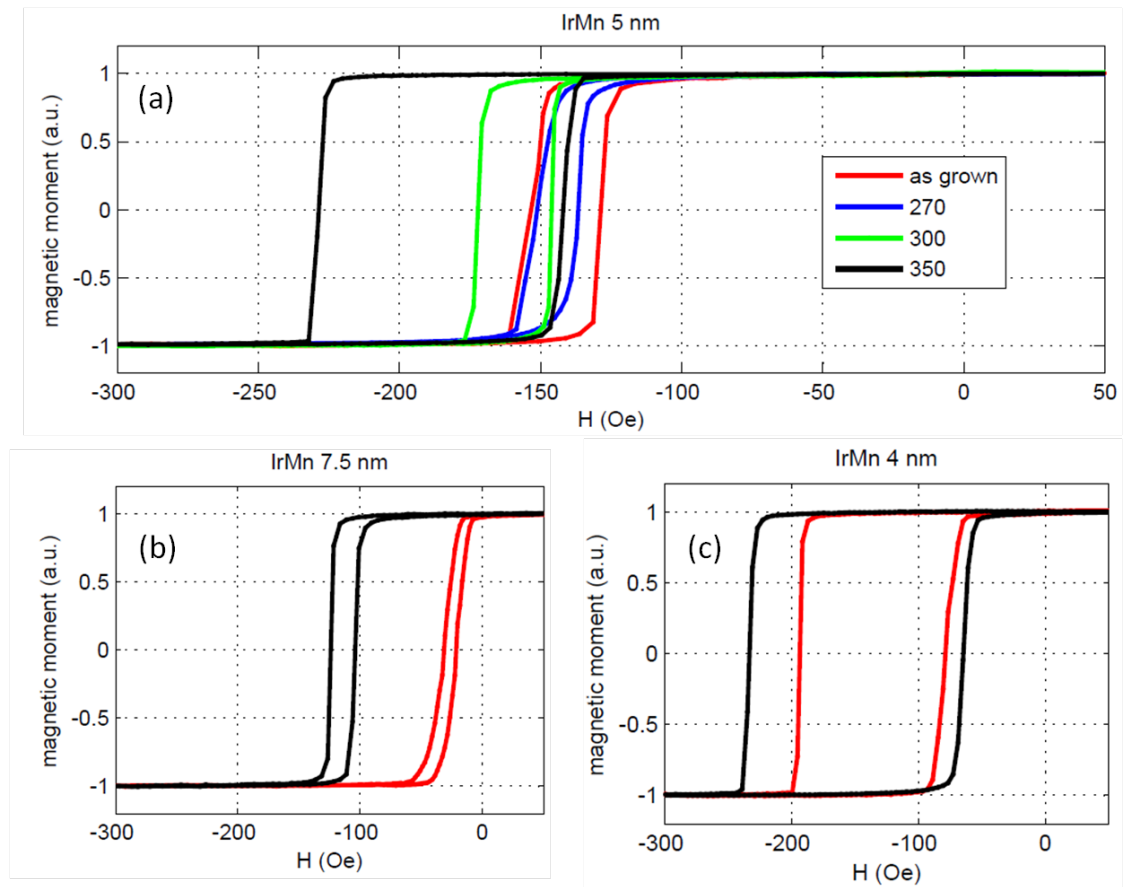


Figure 3.8: Effect of annealing on EB. All data shown are measured at 5 K after cooling in a magnetic field +0.5 T from 400 K in-plane of the sample. Sample with 5 nm thick IrMn (a) was measured as grown and annealed at 270°C, 300°C, 350°C, samples with 7.5 nm thick IrMn (b) and 4 nm thick IrMn (c) measured as grown and annealed at 350°C.

**Exchange Coupling at IrMn/CoFeB Interface** Another studied system was IrMn/CoFeB interface where IrMn was only 1 nm thin. This bilayer is not as much studied as IrMn/NiFe or IrMn/CoFe because the observed exchange broadening is weaker and exchange bias was found to be small and shifted to positive values (positive exchange bias). Consistent with literature [52] we observed a small positive exchange bias and only a small exchange broadening as shown in

Fig. 3.9 when sample is field cooled in magnetic field from 400 K to 5 K. The ultra thin IrMn has lower  $T_N$  and therefore also the blocking temperature of the exchange coupling is lowered. At 200 K the interface IrMn/CoFeB does not exhibit any exchange coupling effect anymore as can be seen in the right panel in Fig. 3.9.

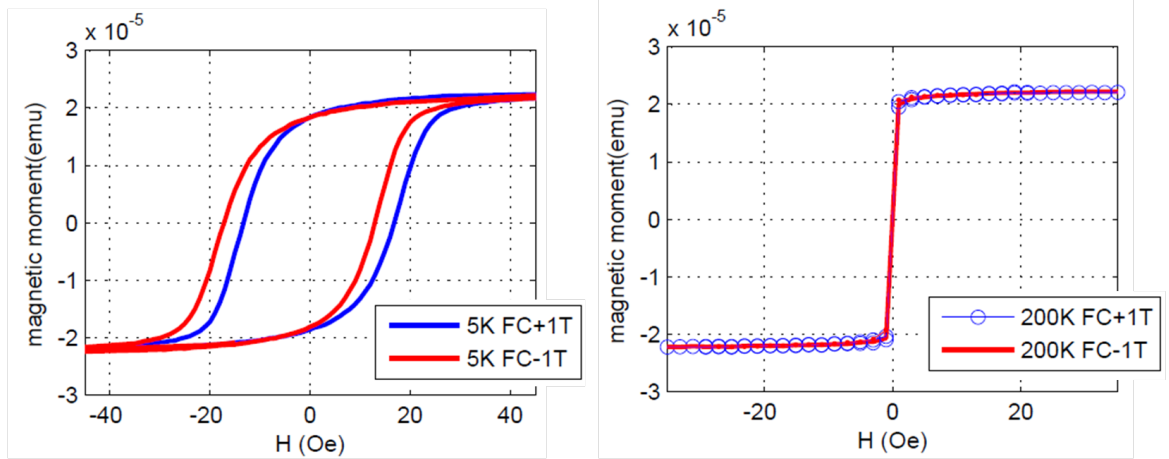


Figure 3.9: Exchange coupling on IrMn/CoFeB interface. Left: Measured at 5 K after cooling in magnetic field  $\pm 1$  T from 400 K in-plane of the sample. Right: After cooling in magnetic field from 400 K to 200 K.

### Samples with IrMn only

Wafers without FM layer are expected to show only linear paramagnetic or diamagnetic signal when measured in SQUID (depending on the type of used substrate). The absence of net magnetic moment is an important confirmation of fully compensated AFM without FM inclusions or impurities. For this reason we have measured a magnetization loop of all wafers containing no FM prior device fabrication. An example is shown in Fig. 3.10. Note that there is no hysteretic behavior observed. Furthermore, the linear magnetization loop can be roughly compared with expected diamagnetism of the substrate. Knowing the size of the presented sample and the magnetic susceptibility of silicon we estimated the magnetic moment to be roughly  $1.2 \times 10^{-5}$  emu when 1000 Oe is applied, which is in agreement of measured data. We also estimated the contribution of a 10 nm thick IrMn film in case all the magnetic moments of Mn would be polarized, and we obtained value  $\sim 1.0 \times 10^{-5}$  emu. This value would be visible in the measured data, if present. Because this contribution was not observed we concluded that IrMn has the expected AFM order.

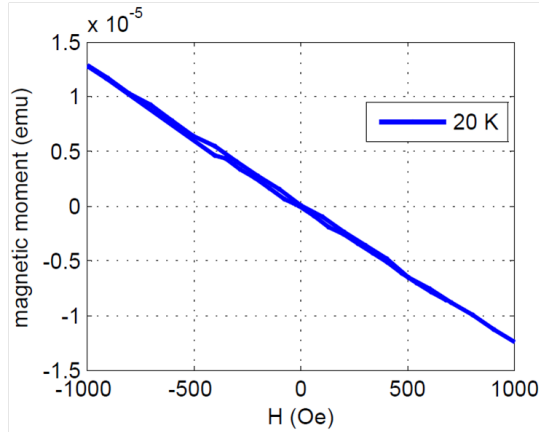


Figure 3.10: Magnetic moment of a sample with 10 nm thick IrMn (comprising no FM). No net magnetic moment can be observed

### 3.4 AFM Moments Manipulation by Exchange Spring Effect

The first discussed technique of AFM moments manipulation is the exchange spring effect [44]. When a FM is coupled to IrMn the rotation of FM moments can lead to a spring created in the IrMn layer. According to the Mauri model an exchange spring can be created if  $K_u^{\text{AFM}}$  is small, which is the case of thin IrMn. In thick IrMn layers  $K_u^{\text{AFM}}$  is relatively stronger and the exchange spring is less favorable to appear.

On the other side, when the IrMn layer is too thin, the anisotropy is lowered, and the AFM layer rotates fully with the FM, only increasing  $H_{\text{ec}}$ . This means that an exchange spring creation depends on the thickness of IrMn. Another parameter that strongly influences the exchange spring is temperature variation of the IrMn anisotropy and the exchange coupling constant. Therefore, we have systematically measured bilayers of IrMn/NiFe(10 nm) with varying IrMn thickness from 1.5 nm to 10 nm in temperature range between 5 K to 400 K.

#### 3.4.1 SQUID Measurements

The exchange spring effect can be studied by analyzing SQUID measurements of a magnetization loop  $M(H)$  of a FM coupled to an AFM. This method does not require sample patterning and, compared to sensitive MTJ devices, the risk of sample damage is very low. It is important to note, however, that the SQUID magnetometry detects only the FM ordered moments, therefore the information about AFM moments can be deduced only indirectly. The schematic illustration of the measured stack of layers is in Fig. 3.11.

An example of a magnetization loop without any exchange coupling effect is shown in Fig. 3.12 (a). In this case the response measured by SQUID magnetometer reflects only the magnetic properties of NiFe,  $M(H)$  is not shifted and has a small coercive field.

When AFM moments are robust (typically when the AFM layer is thick)  $M(H)$  is shifted as can be seen in Fig. 3.12 (b). In this case the IrMn/NiFe interface adds an exchange field which is causing the shift of  $M(H)$ , however, no exchange



Figure 3.11: Schematic illustration of the stack of layers used for exchange spring effect experiments.

spring is generated and AFM moments are not manipulated. Another extreme case is a very thin IrMn, where the lowered anisotropy allows the AFM layer to fully follow the FM layer and therefore no shift of  $M(H)$  is created. Instead, the magnetization loop is broadened as can be seen in Fig. 3.12 (c). Both of these situations can be explained within the MB model of exchange coupling. The last scenario, shown in Fig. 3.12 (d), is a magnetization loop that is both broadened and shifted. This means that the AFM moments can be rotated, however, only partially (compared to the full rotation represented in Fig. 3.12 (c)). The last two examples are of particular importance for transport measurement and it can not be described by a simple MB model as will be discussed in the end of this section.

As already mentioned, the important parameters that decide if exchange spring can lead to any AFM moments reorientation are the thickness of IrMn and the experimental temperatures. The data shown in Fig. 3.12 are selected to illustrate four possible scenarios. For a complete picture, however, we measured systematically several thicknesses of IrMn at various temperatures. The list of samples can be found in Appendix A.2, the thickness of IrMn ranged from 1.5 nm to 10 nm, all samples were measured after field cooling in magnetic field 0.5 T in-plane of the sample from 400 K to temperatures between 5 K to 390 K. Every  $M(H)$  was then analyzed and values of exchange broadening  $H_{ec}$  and exchange bias  $H_{eb}$  were extracted. The results of this analysis are summarized in Fig. 3.13.

As seen in the left panel of Fig. 3.13  $H_{eb}$  is strongest for IrMn thickness  $\sim 4$  nm at 5 K. When temperature is increased  $H_{eb}$  for IrMn 4 nm is getting significantly weaker and it vanishes at  $\sim 350$  K. The reduced blocking temperature of  $H_{eb}$  is related to lowered  $T_N$  of thin IrMn. For thicker 10 nm IrMn the exchange bias at low temperature is not as strong as for the thin IrMn; however, it persists up to higher temperature (the instrument measurement range did not allow to study blocking temperature higher than 400 K). Right panel of Fig. 3.13 shows exchange broadening as a function of IrMn thickness and temperature. It can be seen that the highest broadening at low temperature is observed for thinnest IrMn. When increasing temperature  $H_{ec}$  is relatively quickly decreasing for all thicknesses of IrMn with exception of IrMn  $\sim 3$ -5 nm thick. This means that for this thickness range the AFM moments are partially rotated also at higher temperatures.

Based on Fig. 3.13 we can identify four different regions with respect to the exchange coupling behavior, and condense Fig. 3.13 into a diagram shown in

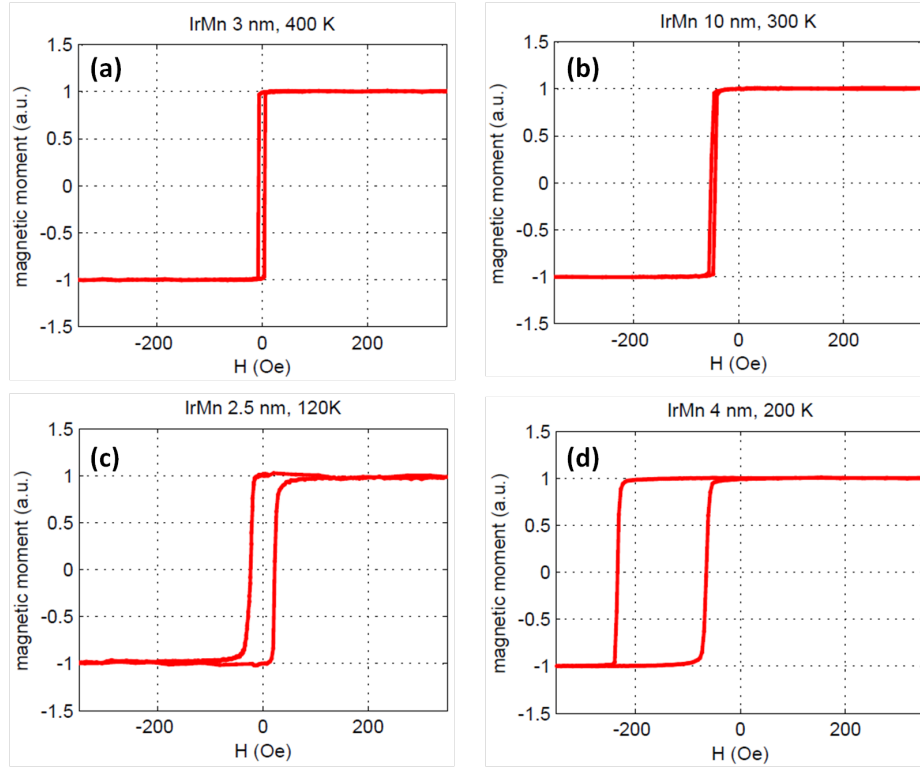


Figure 3.12: Effect of exchange coupling on magnetization loop of NiFe. (a)  $M(H)$  when IrMn/NiFe interface is not coupled. (b)  $M(H)$  for robust "bulk-like" IrMn, the coercivity is not increased, only exchange shift appears. (c)  $M(H)$  for IrMn with low anisotropy, thin IrMn which rotates fully with NiFe,  $M(H)$  exhibits only increased coercivity without exchange shift. (d)  $M(H)$  with both increased coercivity and shift, partial rotation of IrMn moments.

Fig. 3.14. In the first region above both blocking temperatures no exchange coupling effect is observed (red color in Fig. 3.14). The second phase (green) can be interpreted as the situation when IrMn and NiFe are coupled, however, anisotropy of IrMn is low and it fully follows the NiFe magnetization. The third region (blue) is a transition region when IrMn is thick enough not to be fully rotated and in the same time it is not thick enough that the strong bulk anisotropy would take over. This leads to a partial rotation of the AFM moments, i.e. creation of an exchange spring. The last region (black) covers data measured on thick IrMn samples which at lower temperatures exhibit a weak broadening of  $M(H)$ , however at high temperature behaves as a robust bulk IrMn.

Note that this diagram is reflecting only presence/absence of  $H_{eb}$  and  $H_{ec}$  and not their value. Therefore also a small  $H_{eb}$  and  $H_{ec}$  (which might not be seen at color scale in the right panel in Fig. 3.13) lead to partial rotation (blue region in Fig. 3.14).

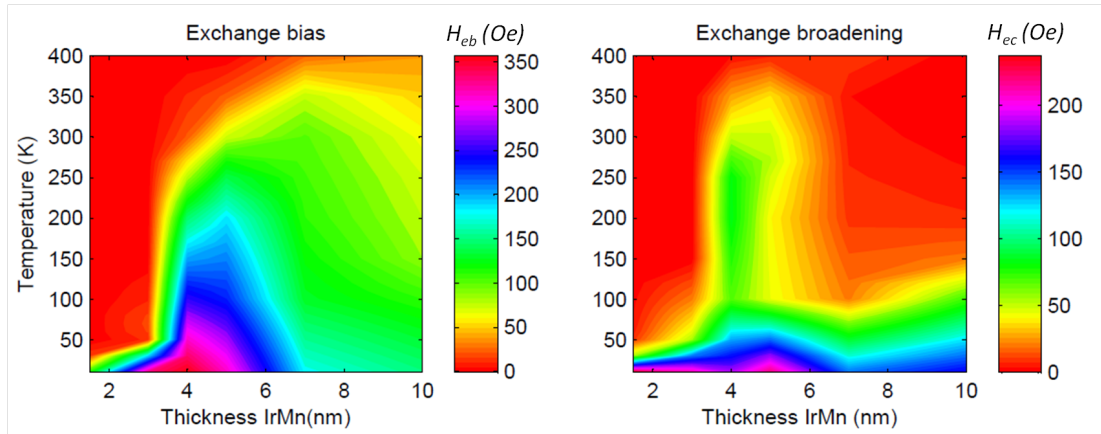


Figure 3.13: Exchange bias and exchange broadening in IrMn/NiFe as a function of IrMn thickness and temperature measured from non-patterned wafers of size  $\sim 3 \times 5 \text{ mm}^2$  after cooling in 0.5 T magnetic field from 400 K.

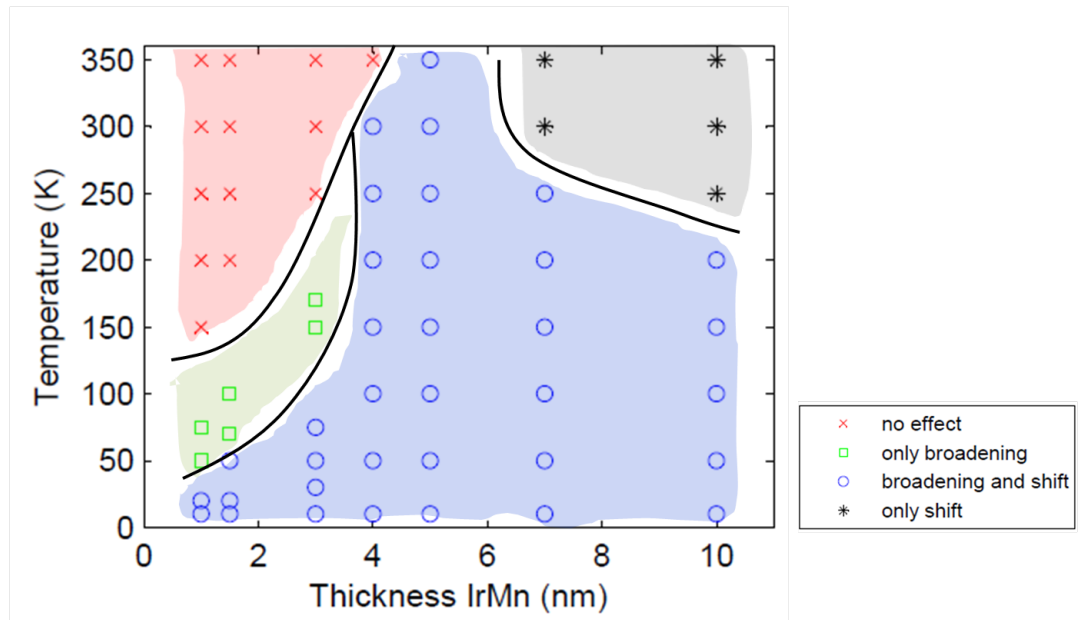


Figure 3.14: Phase diagram of the exchange coupling effect. Measured at non-patterned samples of size  $\sim 3 \times 5 \text{ mm}^2$  with different IrMn thickness at different temperature after cooling in magnetic field 0.5 T in sample plane from 400 K.

### 3.4.2 TAMR Measurements

The diagram presented in Fig. 3.14 summarized the exchange coupling as measured by SQUID magnetometry, which is an indirect method relying on the FM and its coupling with the AFM. As was discussed in the introduction chapter, the orientation of AFM moments can be directly detected by the tunneling anisotropy magnetoresistance. A TAMR device structure is sketched in left panel of Fig. 3.15: a MgO tunneling barrier is separating the IrMn and top Pt electrode. The top and bottom electrodes allow wire-bonding without affecting the tunneling pillar ( $2\text{-}50\ \mu\text{m}^2$ ), typically we measured tunneling structures with dimensions  $3\times 6\ \mu\text{m}^2$  which showed most robust transport properties. The resistance was measured using a four-point geometry at constant bias voltage of 20 mV applied to the top electrode. The tunneling barrier is expected to show a non-linear  $I(V)$  dependence when measured across the barrier; a typical  $I(V)$  characteristic is shown in the right panel in Fig. 3.15. To highlight the non-linearity of the  $I(V)$  characteristic also the derivative is shown in the figure.

The tunneling resistance is sensitive to the density of states and the chemical potential of the electrodes [4] near to the barrier, therefore the AFM layer is the active element in this structure. This means that the relative orientation of AFM moments leads to a variation of the TAMR signal and therefore can serve as a direct detection of a change of the AFM moments orientation. We have measured TAMR response on devices fabricated from the same wafers that were characterized by SQUID, and we have shown a clear correspondence, as will be presented in the following.

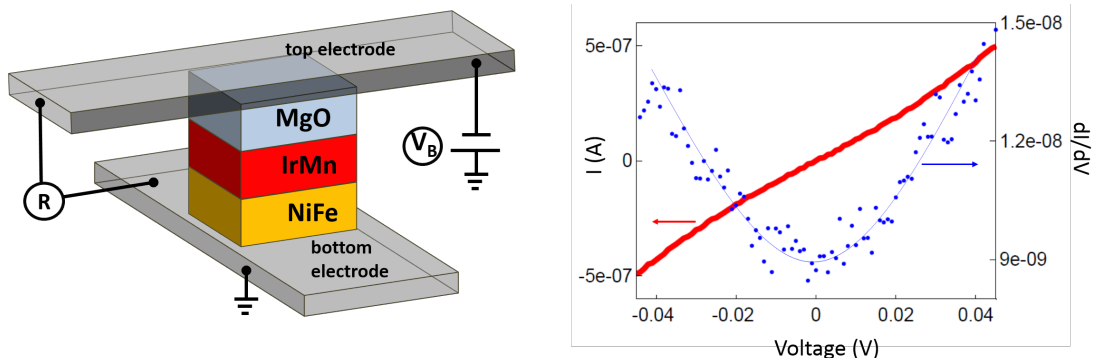


Figure 3.15: Left: Schematic illustration of the tunnel junction pillar between the top and the bottom electrode. Voltage and current contacts were connected to the same electrode. Wire-bonding pads were spatially far from the sensitive tunnel junction. Right: A typical  $I(V)$  characteristic of a TAMR device measured from a MTJ with an area of  $3\times 6\ \mu\text{m}^2$ . The non-linearity is clearly seen in  $dI/dV$  (blue line).

**Correspondence between Magnetometry and TAMR** TAMR was measured during in-plane magnetic field sweep while biasing the junction with a constant voltage, typically 20 mV. As the TAMR signal varies with the orientation of the AFM moments below the barrier we can expect several types of behavior depending on the exchange coupling on the IrMn/NiFe interface. This

is illustrated in Fig. 3.16, where data of the TAMR device with 3 nm IrMn is presented in several phases of the diagram in Fig. 3.14 for different temperatures corresponding to different scenarios according to Fig. 3.14. When no exchange coupling effect is present (corresponding to SQUID data shown in Fig. 3.16 (a)), the AFM moments can not be manipulated and no TAMR signal variation is observed, as shown in Fig. 3.16 (b). A similar situation occurs when IrMn is coupled to NiFe, however, it is too rigid to be manipulated. This is the situation described in Fig. 3.14 by black points and it is typical for thick IrMn. In these two cases the signal of TAMR is not affected by the external magnetic field sweep.

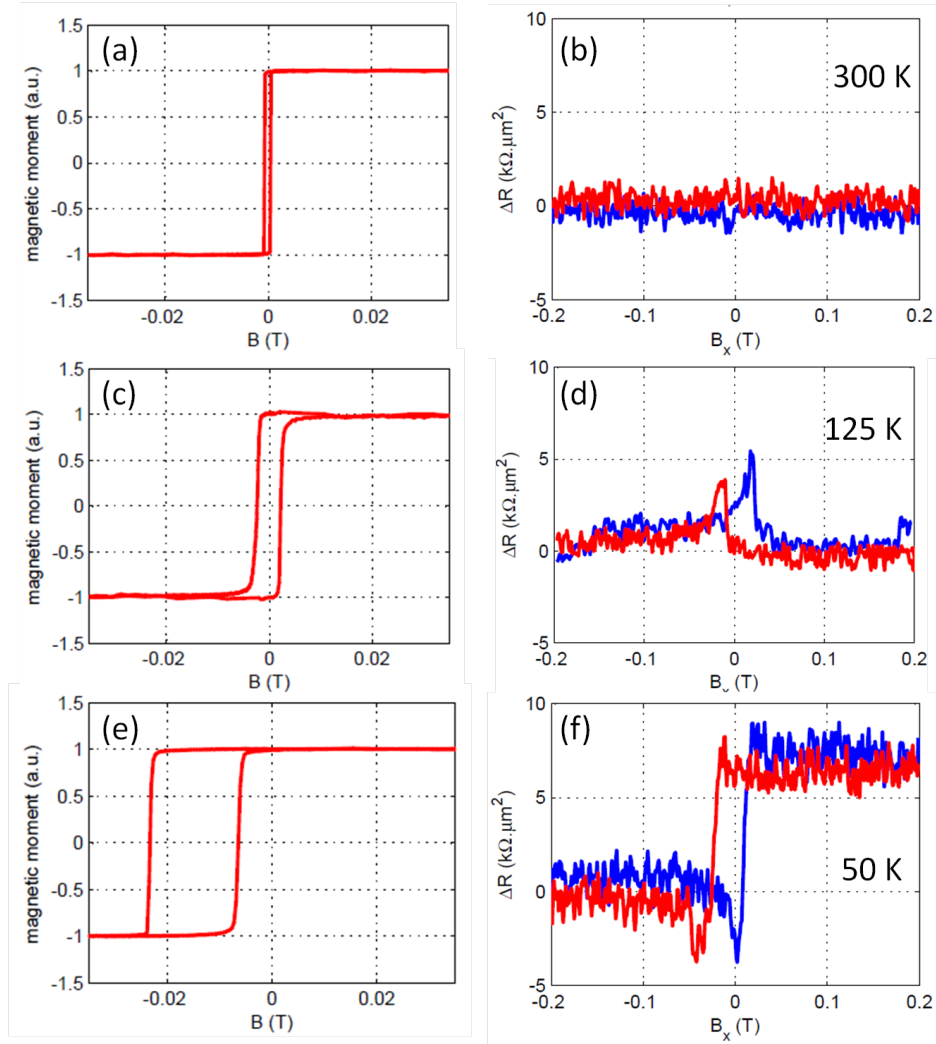


Figure 3.16: Corresponding TAMR and SQUID signals on IrMn 3 nm sample. SQUID data are examples representing different phases of the diagram: (a) no exchange coupling effect (400 K), (b) only broadening (120 K) and partial rotation (50 K). Transport data measured at (b) 300 K, (d) 125 K, (f) 50 K. Applied voltage at TAMR junction was 0.02 V and MTJ area of  $3 \times 6 \mu\text{m}^2$  was used. Two colors of the TAMR signal correspond to two directions of in-plane magnetic field sweep.

The next phase describes the case of IrMn layer with low anisotropy. An example of SQUID data is shown in Fig. 3.16 (c), where only exchange broadening is observed. Corresponding TAMR signal is shown in Fig. 3.16 (d). As can

be seen from the SQUID data, the AFM moments are fully rotating with the FM, consequently, the orientation of the IrMn moments changes by  $180^\circ$  when magnetic field sweeps from positive to negative values. As was explained in the introduction, these two states are indistinguishable by their resistance. Only during moment reversal in the close vicinity to zero magnetic field, when the moments are rotating, the TAMR signal varies. This is what is observed in Fig. 3.16 (d), the TAMR values measured at high positive and negative magnetic fields are identical and the only variation occurs around zero magnetic field.

The last discussed phase corresponds to M(H) with non-zero  $H_{ec}$  and  $H_{eb}$  as shown in Fig. 3.16 (e), i.e. the blue points in Fig. 3.14. The TAMR signal is shown in Fig. 3.16 (f). In this case the moments are dragged by NiFe and rotated only partially to a metastable position. Therefore, the orientation of the AFM moments for two magnetic field directions is different. The TAMR signal has two states for two polarities of the magnetic field and exhibits spin-valve like behavior.

In order to complement our data we performed measurements when a magnetic field with an amplitude higher than the saturation field was rotating. Because the magnetic field is higher than  $H_C$ , the magnetization of NiFe follows the magnetic field. If IrMn and NiFe are coupled the AFM moments are dragged by the FM. The results are summarized in Fig. 3.17 and are consistent with the presented magnetic sweep data. At low temperature (Fig. 3.17 (a) and (b)) TAMR signals at  $0^\circ$  and  $180^\circ$  are not identical, in other words two indistinguishable states exist when magnetic field changes from positive to negative value. This corresponds to the partial rotation of the AFM as depicted by blue color in Fig. 3.14. At 50 K (Fig. 3.17) the 3 nm IrMn sample (c) again exhibit two different states when magnetic field rotates  $180^\circ$ , however, the thin IrMn 1.5 nm (d) already shows identical state at positive and negative fields. This corresponds to the green region in Fig. 3.14 where AFM moments are fully rotated. At 100 K both 3 nm and 1.5 nm IrMn fully follow the NiFe and thus the TAMR signal at  $0^\circ$  and  $180^\circ$  is identical (Fig. 3.17 (e) and (f)).

### 3.4.3 Discussion of Results in Context of Existing Models

In the MB model (explained in Chap. 2.1.2)  $H_{eb}$  should vanish when  $K_u^{AFM}t_{AFM}/J_{eb} < 1$ . It is known that  $K_u^{AFM}$  decreases when temperature increases [133] which is generally consistent with our data; in the left panel in Fig. 3.13 we observe  $H_{eb} = 0$  for higher temperature in thin samples. The anisotropy  $K_u^{AFM}$  of the IrMn also depends on the thickness of the film. In the left panel in Fig. 3.13 can be seen that with increasing thickness the exchange bias persists up to higher temperatures.

The measured data point to some limitations of existing exchange coupling models. The MB model tends to overestimate the strength of coupling. In the MB model exchange coupling constant  $J_{EB}$  can be estimated from Eq. 2.15 leading to, for example,  $J_{EB} \sim 0.4$  erg/cm<sup>2</sup> for the 3 nm IrMn sample at low temperature. The estimated effective interface coupling constant  $J_{eb}$  is smaller than the exchange constants in the AFM and FM materials alone.

The major failure of the MB model is, however, to explain simultaneous presence of  $H_{eb}$  and  $H_{ec}$  as we observed in our data (blue color in Fig. 3.14). This is

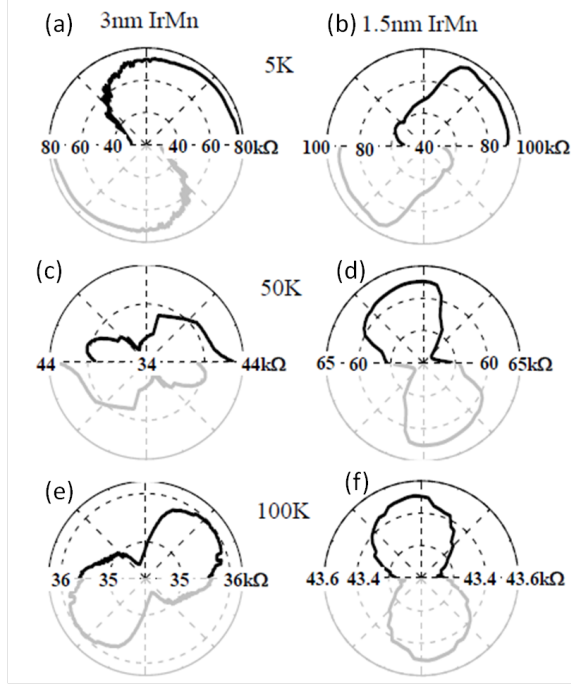


Figure 3.17: TAMR when magnetic field is rotated with amplitude higher than the coercive field of NiFe for different temperature and IrMn thickness as indicated. The magnetic field was rotated between  $0^\circ$  and  $180^\circ$  (black line), to highlight the symmetry of the effects the inversion symmetry images are added (grey line). After [6].

because the model can not describe the partial rotation of the AFM moments (remember that one of the assumptions is validity of Stoner-Wohlfart single domain model in both FM and AFM). Our TAMR measurements, however, demonstrate the ability of AFM moments to rotate to distinct metastable AFM spin states that are not fully rotated by  $180^\circ$ . The strength of TAMR signal at low temperatures indicates that the AFM moments can be effectively manipulated. This and the pinning to a metastable state could explain the decreased  $H_{eb}$  compared to the MB model expectation.

It can be seen in Fig. 3.16 that TAMR signal exhibits hysteretic behavior both in panel (d) and (f). The coercivity of the TAMR signal can not be directly correlated to  $H_{ec}$  measured by SQUID due to the fact that SQUID averages over the large unpatterned sample, unlike TAMR that is measured on the small area below the tunneling barrier. Some trends can, however, be observed; for example, increase of TAMR coercivity which corresponds to increase of coercivity in right panel in Fig. 3.13. The study of TAMR signal correspondence with magnetometry is, however, limited to the fact that TAMR can be measured only in a relatively narrow window of IrMn thicknesses.

The Mauri model explains the reduced  $H_{eb}$  by creation of domain walls on the AFM/FM interface. Although, this could be true for our thick IrMn samples, this model is unlikely to be valid for our thinnest IrMn samples since they are thinner than the expected domain wall width in IrMn [134, 135]. The Malozemoff and Radu models assume uncompensated spins on the AFM/FM interface as a correction to the simplest exchange bias model. This could explain our SQUID

measurement, our transport measurement is, however, sensitive to the interface between IrMn and tunneling barrier and therefore cannot be explained by these models.

To summarize, by studying the AFM moments manipulation in a FM/AFM/oxide stack by two methods, sensitive either to FM or AFM moments, we could approach not only the AFM/FM interface but also the AFM/insulator interface and complement the existing models that were previously discussed in literature.

### 3.4.4 Thermal Induced Magnetization Fluctuation

In the previous work by Park et al. [5] strong TAMR signal based on IrMn was observed at low temperature; for most of technological applications, however, a room temperature spin-valve signal would be important. Recently, a weak TAMR signal at 300 K was observed in Pt/Co/IrMn/ $\text{AlO}_x$ /Pt system with perpendicular coupling [136]. We have focused to identify the thickness of IrMn which would allow two state spin-valve like signal at room temperature in IrMn/NiFe structures. It can be seen in Fig. 3.14 that AFM moments in  $\sim 4$  nm thick IrMn exhibit partial rotation which corresponds to a two state TAMR signal. Indeed, at 300 K we observed TAMR signal, however, the metastable states were not stable, as can be seen in Fig. 3.18 (c) where raw data show random oscillations between two states when recorded in time. This is caused by the increased temperature at which thermally activated magnetic fluctuations do not allow to stabilize the two states, which are independent on the applied magnetic field. This means that the exchange spring created on the AFM/FM interface is not transferred through the full thickness of IrMn and the AFM moments on the IrMn/MgO interface can not be manipulated by the FM layer.

To confirm that the two states are of TAMR origin we took advantage of characteristic voltage dependence of the TAMR signal. The TAMR signal is not equal at every applied voltage, instead it reaches a maximum at a negative voltage. A typical TAMR signal when 20 mV is applied at low temperature is shown in Fig. 3.18 (a). The corresponding voltage characteristic of the TAMR signal for the same sample is shown in Fig. 3.18 (b) showing the characteristic asymmetry with respect to zero voltage.

Due to the magnetic fluctuations the TAMR signal at 300 K cannot be evaluated by subtracting two resistance states as in the previous case. We can, however, define a TAMR-like ("TAMR") signal by subtracting two measurements (independent of the magnetic field applied). We can measure this signal at different voltage applied to obtain the voltage dependence of TAMR-like signal. The results is shown in Fig. 3.18 (d). It can be seen that it has the characteristic asymmetry.

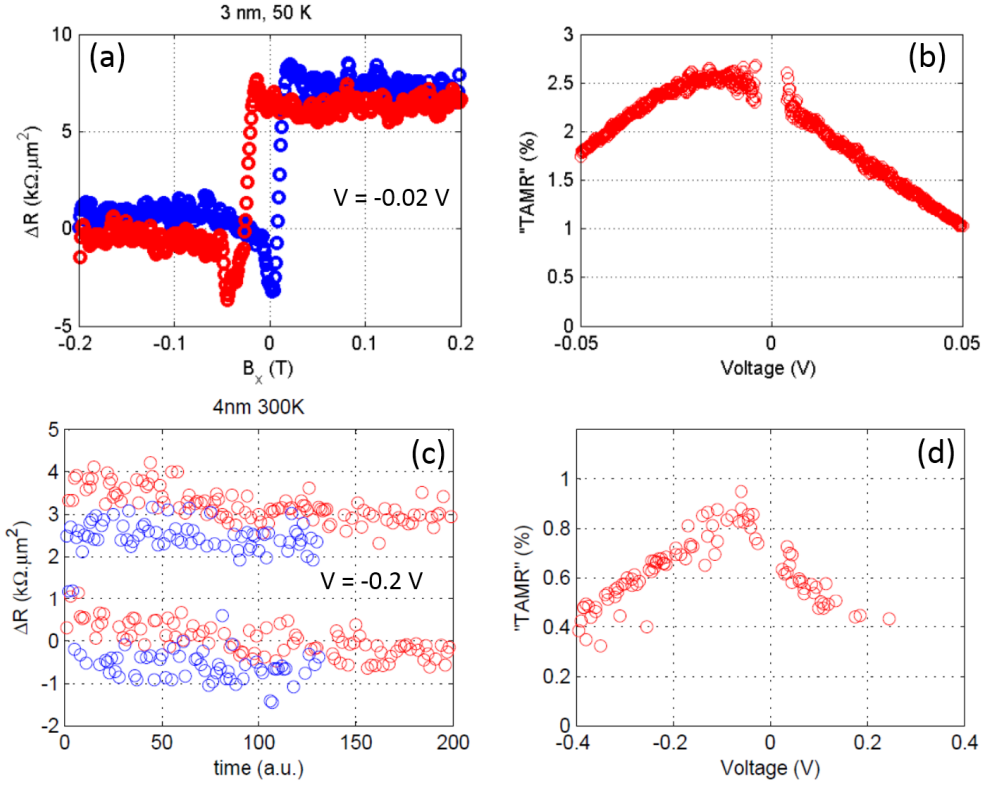


Figure 3.18: Thermal fluctuation of TMR at room temperature. (a) TMR measured at 50 K in sample with 3 nm IrMn when biasing with 0.02 V. (b) Voltage characteristic of TMR signal at 50 K in 3 nm IrMn sample. (c) TMR signal measured at 300 K in the 4 nm IrMn sample. Random switching between two metastable states due to the increased thermal fluctuation. (d) Voltage characteristic of TMR signal at 300 K in 4 nm IrMn sample. Blue and red points in panel (a) and (b) correspond to magnetic field sweep in opposite direction, in panel (b) they illustrate the independence of the signal on the magnetic field.

### 3.4.5 Summary of the Exchange Spring Based AFM Manipulation

In summary, we have systematically studied the exchange spring effect for various IrMn thickness at different temperatures. We developed a method to correlate magnetometry (sensitive to FM layer) and transport data (sensitive to AFM layer) in order to study the orientation of AFM moments. We have identified a region where IrMn moments can be manipulated. Within this region we found the range of IrMn thickness that leads to only partial rotation of IrMn and can be therefore used in a spin-valve structure where IrMn serves as an active element of a spintronic device. We also pointed out that at higher temperatures thermally induced magnetization fluctuations complicate the stabilization of the AFM moments. The measured data complement existing exchange coupling models as discussed above.

### 3.5 AFM Moments Manipulation by Field Cooling

It was shown in the previous section that the AFM moments can be manipulated by the exchange spring effect and afterwards detected by TAMR. Different TAMR states (spin valve-like signal) were defined by the orientation of IrMn moments (i.e. the AFM served as an active element in the MTJ), the FM layer had to be present in order to manipulate the AFM moments. Although the FM layer was only a tool to manipulate the AFM moments, many of the AFM spintronic advantages, as relative insensitivity of AFM moments to an external field or possibility of higher integration density, would be affected by its presence. In this section we will describe another way of AFM moments manipulation which does not require the FM element.

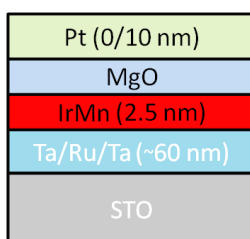


Figure 3.19: Schematic illustration of the stack of the layers used for cooling-in-field experiments.

We prepared a stack of layers (shown in Fig. 3.19) comprising no FM and we show that metastable states corresponding to different spin configurations of the AFM can be set by cooling the sample and crossing the critical temperature  $T_N$  in an external magnetic fields with different orientations. The detection method by TAMR remains same, we only remove the FM from the stack as illustrated in left panel in Fig. 3.20. The devices show tunneling  $I(V)$  characteristics (right panel in Fig. 3.20) typical for standard MgO magnetic tunneling junctions with the same MgO thickness.

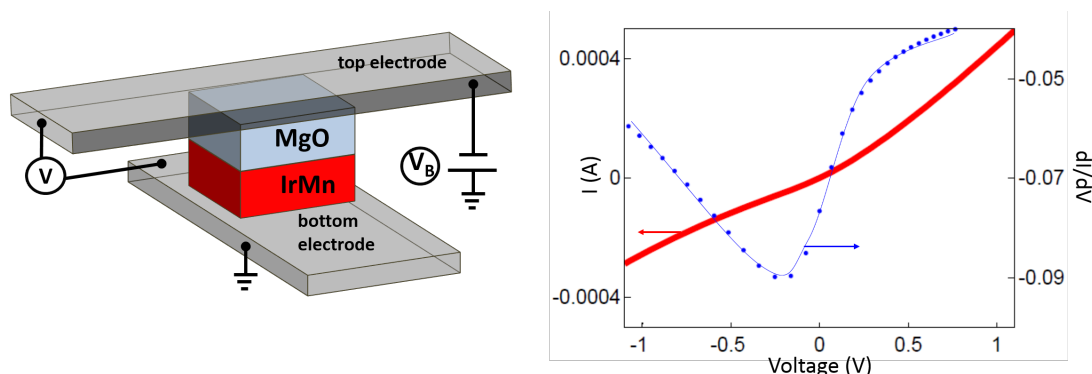


Figure 3.20: Left: Sketch of a TAMR device used for field cooling experiments. Right:  $I(V)$  characteristic and the corresponding  $dI/dV$  showing non-linear dependence.

In order to reduce the Néel temperature of IrMn the thickness of the layer

was only 2 nm. The Néel temperature below 300 K was required in order to be able to measure the transport properties across the transition from paramagnetic to AFM state in the cryostat with temperature range 5 K - 300 K.

The estimated Néel temperature was 173 K. The critical temperature was confirmed by an independent experiment done by M. Molina-Ruiz and A. Lopen-dia (ICMAB, Barcelona, Spain). They determined  $T_N$  by the Quasi-adiabatic nanocalorimetry measurement. This technique directly measures the specific heat of the sample, enabling the observation of the critical behavior in the specific heat near  $T_N$ . The Néel temperature inferred from the inflexion point of the specific heat singularity is approximately 173 K, therefore  $T_N$  was significantly reduced compared to the bulk IrMn  $T_N \geq 1000$  K. More details about the method can be found in [20].

We have measured magnetoresistance while cooling down in applied external magnetic field, the result of cooling in different magnetic fields are shown in Fig. 3.21. The resistance by area (RA) product measured at 20 mV while cooling in magnetic field perpendicular to the sample surface  $H_z = 2$  T (red line) and the magnetic field in the plane of sample  $H_x = 2$  T (green line) are shown. It can be clearly seen that the RA product is identical until approximately 170 K where the splitting of the two lines appears. The difference in resistance after cooling in two different magnetic fields is  $\sim 10$  % at 120 K. When magnetic field is applied perpendicular to the sample surface but with an opposite polarity  $H_z = -2$  T (black symbols in Fig. 3.21) the RA product is same compared to cooling in  $H_z = 2$  T, in agreement with the anisotropic magnetoresistance origin of the measured signal. Note that the strong temperature dependence of the TAMR signal is caused by the STO substrate that is changing its properties with temperature.

Since the difference between TAMR signals for different field cooling disappears above  $T_N$  and since we observe a negligible magnetoresistance when the temperature is stabilized below  $T_N$  (as shown in the right panel in Fig. 3.21), the observed magnetoresistance cannot be explained by a magnetization-independent tunneling transport phenomena as, for example, effect of Lorentz force.

It is shown in the right panel of Fig. 3.21 that once the sample is cooled below the critical temperature, the magnetic orientation of the AFM moments is stable and it cannot be changed by an external magnetic field up to 2 T applied in any direction. This demonstrates that the measured signal is insensitive to relatively high magnetic fields and it originates in AFM moments that become rigid once they are cooled below their critical temperature.

The difference between the two temperature sweeps with different magnetic field applied is shown in Fig. 3.22. In the same figure, the results on nanocalorimetry are shown. It can be seen in Fig. 3.22 that the critical temperature estimated by nanocalorimetry (red line) and transport measurement (black line) are in good agreement.

Several MTJs with same stack of layers was measured, all of the having similar RA and reproducible splitting when field-cooled in in-plane and out-of-plane magnetic fields. A typical difference between two metastable resistance states varied between 2% to 10% at 120 K. The highest values were found in devices with the largest RA.

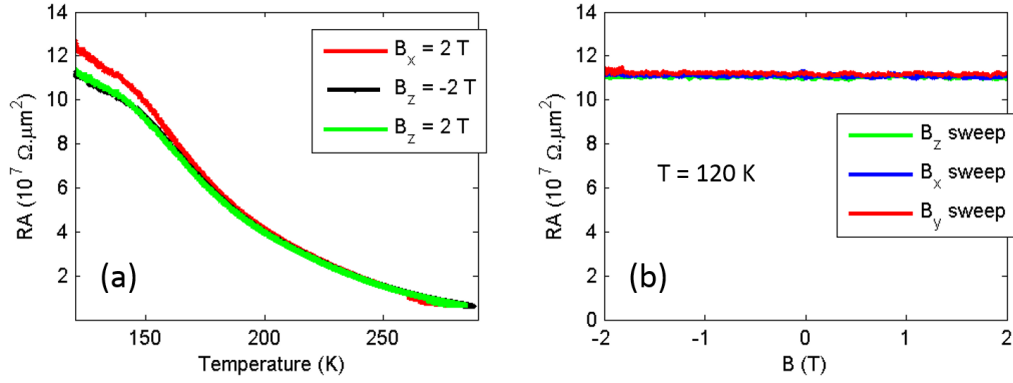


Figure 3.21: TAMR while cooling in field. (a) TAMR signal measured on a sample with area  $3 \times 6 \mu\text{m}^2$  with bias voltage 0.02 V. The signal is insensitive to the magnetic field until the temperature drops to  $T_N$ , where the signal starts to split for different magnetic field orientations. (b) When AFM moments are cooled to the low temperature they can not be manipulated anymore by any external field.

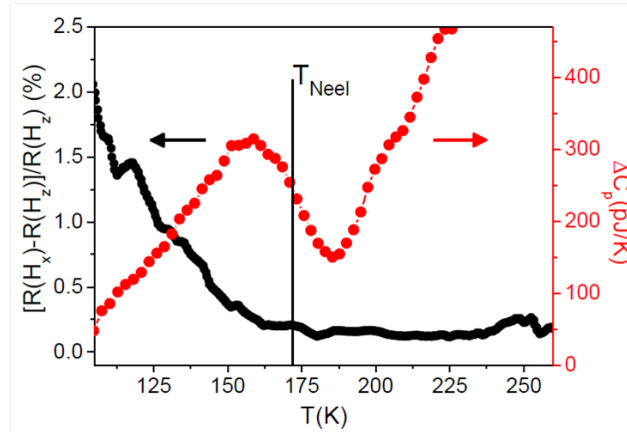


Figure 3.22: Critical temperature estimation by nanocalorimetry and transport measurement. After [7].

### 3.5.1 Summary of Field Cooling Based AFM Manipulation

We have demonstrated the possibility of manipulating AFM moments by cooling AFM material through its  $T_N$  in an external magnetic field. When applying an external magnetic field in different orientations we measured splitting of TAMR signal appearing at  $T_N$ . We demonstrated a proof of concept experiment showing an electrically readable magnetic memory device which contains no ferromagnetic elements and in which information can be written and stored in AFM material.

## 3.6 AFM Moments Manipulation by Current Induced Torques

In the previous two sections we have described two ways of AFM moments manipulation which, however, had limitations either in using a FM layer to manipulate the AFM or in using the slow field cooling procedure. The last discussed method of manipulating IrMn moments does require neither a FM nor a field cooling procedure. It is based on fully electric manipulation of the magnetic moments by current induced spin torques.

### 3.6.1 Current induced torques on AFM moments

In the Chap. 2.4.2 we have introduced current induced torques. In particular we have discussed the spin transfer torque that is commonly used in FMs and also the recent discovery of spin orbit torques that rely on the spin-orbit coupling in the material. The spin orbit torques can be present both in bulk AFMs with broken inversion symmetry of the two sublattices or in thin AFM films where the symmetry is broken by an interface [4].

All these effects were studied in FM materials, however, only limited number of theoretical works considered spin torques acting on AFM [137, 138, 111] and only very recently some of the effects were demonstrated experimentally in AFM materials [110, 126, 139].

Spin torque can be represented as an effective field acting on magnetic moments, eventually manipulating them. The important requirement for AFM moment manipulation by spin torques is the existence of Néel ordered effective fields which couple to AFM moments [137]. This type of effective field can not be understood as a uniform magnetic field, instead it has locally varying direction depending on the orientation of AFM moments.

**Spin-transfer torque in AFMs** The non-relativistic spin transfer torques acting on AFM moments are studied theoretically [138, 140]. STT contains anti-damping and field-like terms and only the first can effectively couple to the AFM moments [137]. Non-reversal switching of a biaxial AFM should be possible, however, no experimental evidence of STT acting on AFM moments was demonstrated yet.

**Spin-orbit torques in bulk AFMs** Very recently theory prediction [111] and first experiments [110] suggested the possibility of switching AFM coupled moments in materials with locally broken bulk inversion symmetry of the magnetic sublattices, as  $\text{Mn}_2\text{Au}$  or  $\text{CuMnAs}$ . In this case inverse spin galvanic effects are responsible for the current induced effective fields.

**Spin-orbit torques in thin AFM films** In thin films the locally (microscopically) broken inversion symmetry of the material is not the only scenario when a torque can be observed. The inversion symmetry in a system comprising thin films can be broken globally (macroscopically) by the interfaces between the layers. The AFM layer can be sandwiched between two different non-magnetic

metals resulting in anti-damping like spin orbit torque acting on the AFM moments.

The second scenario of current induced torques in a thin AFM film includes a multilayered system of an AFM adjacent to a non-magnetic heavy metal. As a result of strong spin-orbit coupling vertical spin current is generated in the heavy metal due to the spin Hall effect and injected to the adjacent AFM. The spin current generates an anti-damping like torque acting on AFM moments.

### 3.6.2 Samples

The samples studied in this chapter are ultrathin polycrystalline IrMn films. IrMn does not show inversion asymmetry in the bulk, however, the inversion symmetry in our samples was broken by two IrMn interfaces Ta/IrMn/CoFeB or Ta/IrMn/MgO. This structural inversion asymmetry can generate antidamping spin-orbit torque. The second effect we can expect in our samples is SHE spin current generated in Ta and injected to IrMn.

Experimentally we have studied several samples with the stack of layers schematically shown in Fig. 3.23 consisting of MgO/IrMn/Ta, MgO/CoFeB/IrMn/Ta and reference sample without IrMn CoFeB/Ta.



Figure 3.23: Schematic illustration of the stack of the layers used for spin orbit torque experiments.

In order to access both paramagnetic and antiferromagnetic phase of IrMn, we have selected the ultrathin 1 nm IrMn which has critical temperature suppressed below 200 K. Moreover, the small thickness of the AFM is favorable for detecting spin-torques generated at the NM/AFM interface. The stacks of layers and their thicknesses were confirmed by XRR, as shown in Chap. 3.3.1. The coupling between the AFM and FM layers was confirmed by the observation of a weak positive exchange bias and small broadening as expected for a thin IrMn/CoFeB interface. The wafers were patterned into Hall bars as described in Chap. 3.2.3, a typical longitudinal Hall bar resistance is  $\sim 1.5 \text{ k}\Omega - 2.5 \text{ k}\Omega$ . The resistance did not vary significantly in the measured temperature range, as shown in Fig. 3.24.

### 3.6.3 Detection of current induced torques

Various techniques can be used for sensitive detection of non-ohmic current induced effects. Although some of them employ optical methods [141] or ferromagnetic resonance [126], the majority of techniques relies on transport measurements. Several transport based experimental methods were developed. One

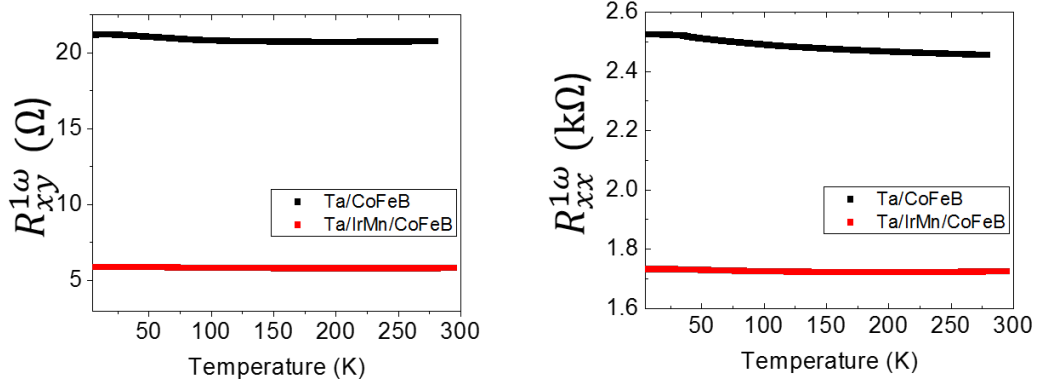


Figure 3.24: Ohmic resistance as a function of temperature measured on transverse (left) and longitudinal (right) contacts. Data of the trilayer sample with Ta/IrMn/CoFeB (red points) and the reference sample Ta/CoFeB (black points) are shown. The small non-zero  $R_{xy}$  is an artifact originating in lithography and will be discussed.

measures the dependence of the coercive field on an in-plane dc-current [97, 142]. Another method measures the equilibrium magnetization direction as a function of external magnetic field using dc current [115, 143, 144]. We have employed the second harmonic technique [145, 97, 116, 146, 118] which is sensitive to non-linear changes in the measured voltage that are caused by current induced changes in resistance.

Spin torques generated by an alternating electric current  $I_{AC}$  tilt the magnetization  $\mathbf{M}$  from its stable position  $\mathbf{M}_0$  by a small amount. We detect the torque via two magnetotransport effects, which were explained in Chap. 2., anisotropic magnetoresistance (AMR) and anomalous Hall effect (AHE). We recall that AMR is an even function of magnetization and can be measured both in FMs and AFMs. AHE is an odd function of magnetization and can be measured only in FMs.

In general, spin torques can be represented as an effective magnetic field  $H_{\text{eff}}$ . Since the spin torques in our case are generated by an AC excitation current  $I_{AC} \sim I_0 \sin(\omega t)$ , the effective field is also varying with the alternating current  $H_{\text{eff}}(I_0) \sin(\omega t)$  and due to the low (non-resonant) frequency the magnetization follows the effective field. The effective field contains antidamping-like and field-like contributions, which were described in Chap. 2.4.2. Another contribution to current dependent effective field is the Oersted field  $H_{\text{Oersted}}$  generated by the current in the sample. The total effective field is therefore  $\mathbf{H}_{\text{eff}} = \mathbf{H}_{\text{AD}} + \mathbf{H}_{\text{F}} + \mathbf{H}_{\text{Oersted}}$ .

In addition, a strong external field  $H_{\text{ext}}$  to saturate the FM layer is applied during the experiment, the total magnetic field  $H$  acting on a sample is

$$\mathbf{H} = \mathbf{H}_{\text{ext}} + \mathbf{H}_{\text{anis}} + \mathbf{H}_{\text{eff}}(\mathbf{I}_{\text{AC}}), \quad (3.1)$$

where  $H_{\text{anis}}$  is the anisotropy field reflecting the magnetic properties of a sample.

AMR and AHE are functions of the magnetization orientation, the magnetization follows the total magnetic field  $H$ . The small current induced change in

magnetoresistance  $R$  can therefore be written for small  $H_{\text{eff}}$  as

$$R(H) \sim R(H_0) + \left. \frac{dR}{dH} \right|_{H_0} H_{\text{eff}}(I_0) \sin(\omega t), \quad (3.2)$$

where  $H_0$  is the current independent part of the total magnetic field (comprising the external magnetic field and the anisotropy field).

The measured voltage is according to the Ohm's law

$$V_{\text{meas}} = R(H)I_{AC} \sim I_0 \left. \frac{dR}{dH} \right|_{H_0} \frac{H_{\text{eff}}(I_0)}{2} + I_0 R \sin(\omega t) - I_0 \left. \frac{dR}{dH} \right|_{H_0} \frac{H_{\text{eff}}(I_0)}{2} \cos(2\omega t) \quad (3.3)$$

where the first term on the right side of the equation is a DC offset, the second term is the first harmonics corresponding to the ohmic response of the sample and the last term corresponds to the second harmonics which is proportional to the current generated effective field. Note that the DC offset also contains information about  $H_{\text{eff}}$ , however, in a standard transport measurement additional artifacts can be present in DC offset and it is difficult to separate them from the current induced effects. Note that the resistance variation with AC current has to be linear or cubic in current to be detected in second harmonics. Changes in magnetoresistance proportional to quadratic power of current would be detected in the third harmonic.

### 3.6.4 Second Harmonics Detection

As explained in the previous section, the second harmonic technique is sensitive to current polarity dependent changes of magnetoresistance. In this section we will describe the used experimental setup. The schematic picture is shown in Fig. 3.25. The sample is excited by an AC current source at low frequency, typically 123 Hz. Four lock-in amplifiers are connected to measure longitudinal  $R_{xx}(1\omega, 2\omega)$  and transverse  $R_{xy}(1\omega, 2\omega)$ . The lock-in amplifiers measuring  $R_{xy}^{2\omega}$  and  $R_{xx}^{2\omega}$  are set to measure at double frequency phase shifted by  $90^\circ$  with respect to the AC excitation. This signal we will refer to as a second harmonic signal  $R^{2\omega}$ . One more lock-in is used to measure the effective current in the device.

The first and second harmonic signal was measured while magnetization was rotated in three planes as shown in Fig. 3.25. Note that when magnetic field rotates in-plane the magnetization follows exactly the magnetic field. However, when magnetic field is rotated to the out-of-plane direction, the angle of the magnetization and magnetic field is not always identical, as will be discussed in more details later.

### 3.6.5 Artifacts Caused by Sample Fabrication

**Contacts asymmetry** Small defects in Hall bars fabrication can lead to artifacts in the transport measurement. An artifact in the measured voltage can be caused by a small asymmetry between the two transverse contacts as illustrated in left panel in Fig. 3.26 or asymmetry in two longitudinal contacts as illustrated in right panel in Fig. 3.26. The asymmetry in transverse contacts leads to non-zero Hall signal in zero magnetic field  $asV_{xx}$  as can be seen, for example, in left

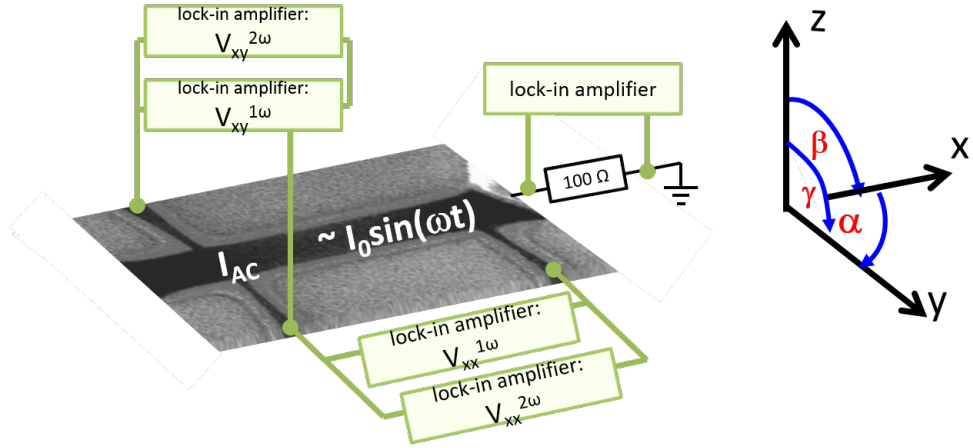


Figure 3.25: Electron microscope image of the Hall bar device with a schematic picture of the experimental setup for second harmonic measurements and the definition of the angles of magnetization rotation:  $\alpha$  for magnetization rotation in-plane of the sample,  $\beta$  and  $\gamma$  for the two planes perpendicular to the sample plane.

panel in Fig. 3.24. The asymmetry in longitudinal contacts can lead to a small transverse contribution  $asV_{xy}$  measured on the longitudinal contacts. This effect is especially strong in situations when the transverse signal is much stronger than the longitudinal, for example in case of strong AHE and relatively weak AMR effect.

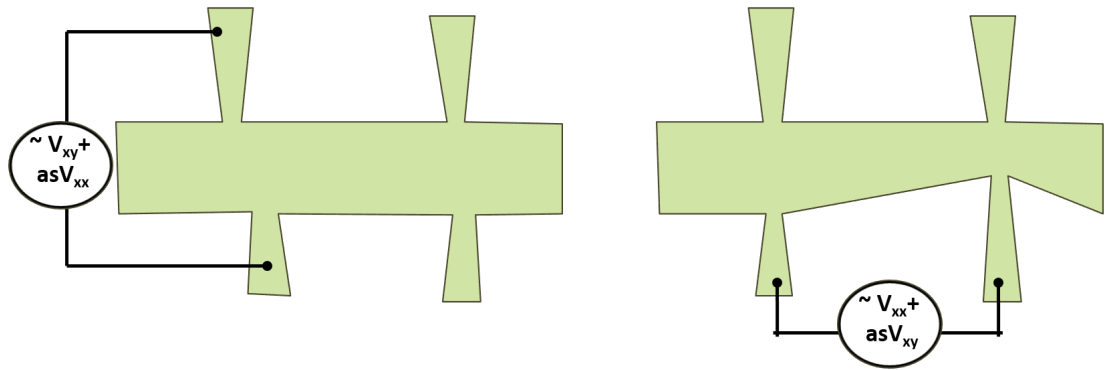


Figure 3.26: Schematic picture of artifacts caused by contacts asymmetry. Left: Transverse voltage consists of Hall voltage and small contribution from contacts asymmetry  $asV_{xx}$ . Right: Longitudinal voltage consists of longitudinal voltage and small contribution from contacts asymmetry  $asV_{xy}$ .

**Thermal gradients** Another important source of artifacts are thermal gradients generated in a Hall bar. Electrical current  $I_{AC}$  in the Hall bar causes Joule heating, which leads to thermal gradients within the sample. The Joule heating is modulated with the double frequency as the excitation current and therefore thermal gradients are also modulated by that frequency. The thermovoltage is proportional to the periodically changing thermal gradient and it causes period-

Magnetization direction	$\Delta T_x$	$\Delta T_y$	$\Delta T_z$
x (along current)	0	0	$V_y$
y	0	0	$V_x$
z	$V_y$	$V_x$	0

Table 3.1: Contribution to transverse and longitudinal voltage from various thermal gradients.

ically changing charge redistribution. Depending on the magnetization orientation and charge redistribution direction (i.e. thermal gradient direction) electrical voltage can be generated.

In principle three thermal gradients, shown in Fig. 3.27, can occur: an out-of-plane thermal gradient ( $\Delta T_z$ ), an in-plane gradient along the Hall bar ( $\Delta T_x$ ) and an in-plane gradient transverse to the bar ( $\Delta T_y$ ). The main source of  $\Delta T_z$  is Joule heating of the thin metallic layers and the heat transfer to the heat reservoir, in our case the silicon substrate. The different conductivity of the different metallic layers has only a small effect compared to the heat transfer via the substrate. Depending on the direction of magnetization, different thermal gradients can contribute either to the longitudinal ( $V_x$ ) or transverse ( $V_y$ ) voltage, as summarized in Tab. 3.1

The major source of in-plane gradients  $\Delta T_x$  and  $\Delta T_y$  are imperfections of the Hall contacts as illustrated in Fig. 3.27 (b),(c). These imperfections are results of local variation of sample processing (etching, developing resist etc.) and they generate laterally varying current density and therefore laterally varying heating of the Hall bar. Thermovoltage generated by  $\Delta T_x$  can contribute to the transverse voltage when magnetic field rotates to out-of-plane of the Hall bar. A thermovoltage caused by  $\Delta T_y$  could potentially contribute to the longitudinal signal when magnetic field rotates to out-of-plane, however, this was not observed in our measurements.

**Thermal Contributions to the Second Harmonics** The second harmonics does not measure only contributions from the current generated effective field but also contributions from thermal effects. The current induced Joule heating is also modulated by the AC current. The generated heat is transferred either to the substrate or to a colder part of the structure creating out-of-plane or in-plane thermal gradient. The thermoelectric effects, discussed in Chap. 2.3, can appear as a voltage varying at  $2\omega$  which contributes to the measured signal. The total voltage measured by a lock-in amplifier is

$$V_{\text{meas}}^* = R(H)I_{AC} + V_{\text{th}} \quad (3.4)$$

where  $V_{\text{th}} \sim k_S \Delta T$  is a thermovoltage generated by a thermal gradient  $\Delta T$  and  $k_S$  is a Seebeck coefficient. The thermal gradient generated by Joule heating is proportional to  $I_{AC}^2$  thus the measured thermovoltage scales quadratically with current amplitude. When measuring resistance, however, the signal generated by thermal effects increases linearly with current amplitude.

When magnetization rotates in one of the three planes (x-y, x-z, y-z), thermovoltage generated by  $\Delta T_x, \Delta T_y$  or  $\Delta T_z$  due to the anomalous Nernst effect and spin Seebeck effect can be detected in transverse and longitudinal contacts as

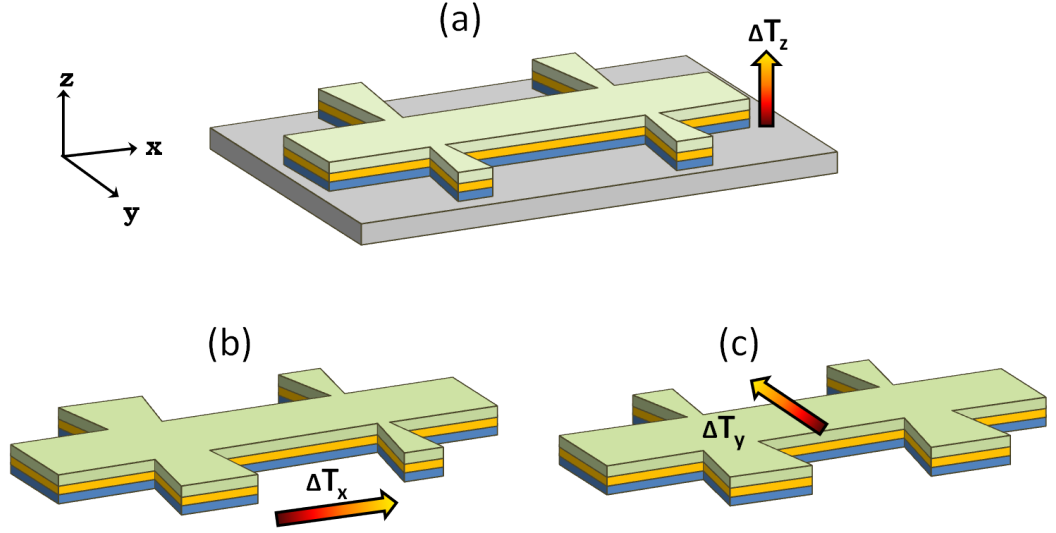


Figure 3.27: Schematic picture of potential sources of thermal gradients in a Hall bar. (a) An out-of-plane thermal gradient is generated by different heat transfer from the thin metallic layers to the substrate and to the He-gas of the cryostat.  $\Delta T_z$  generates signal in both longitudinal and transverse contacts (a). (b) An in-plane thermal gradient along the Hall bar is created by asymmetry between the longitudinal contacts as shown in the figure. (c) An in-plane gradient perpendicular to the Hall bar is caused by asymmetry of the transverse contacts.

summarized in Fig. 3.28. By green color is marked the geometry in which the contribution from the particular thermal gradient is expected.

$\Delta T_x$			$\Delta T_y$			$\Delta T_z$		
$B_{xy}$	$V_{xx}$	$V_{xy}$	$B_{xy}$	$V_{xx}$	$V_{xy}$	$B_{xy}$	$V_{xx}$	$V_{xy}$
$B_{xz}$	$V_{xx}$	$V_{xy}$	$B_{xz}$	$V_{xx}$	$V_{xy}$	$B_{xz}$	$V_{xx}$	$V_{xy}$
$B_{yz}$	$V_{xx}$	$V_{xy}$	$B_{yz}$	$V_{xx}$	$V_{xy}$	$B_{yz}$	$V_{xx}$	$V_{xy}$

Figure 3.28: Contribution to the signal from the anomalous Nernst effect and the spin Seebeck effect when magnetic field rotates in one of the three rotation planes. By green color is marked the geometry in which the contribution from a particular thermal gradient is expected.

In summary, the second harmonic signal contains contributions from current induced effective fields, both with antidamping-like and field-like symmetry. In addition to that, second harmonics also contains current induced thermovoltage such as spin Seebeck effect or anomalous Nernst effect. To separate them, the symmetry of the signal under applied magnetic field needs to be studied.

### 3.6.6 Samples with Ta/IrMn/CoFeB

In this section samples containing CoFeB will be discussed. We have prepared trilayer Ta/IrMn/CoFeB and a reference bilayer Ta/CoFeB into Hall bars. Samples with a FM layer can be analyzed with respect to the rotation of the CoFeB magnetization. Transverse  $R_{xy}$  and longitudinal  $R_{xx}$  resistances were recorded while sweeping and rotating the magnetic field in the three planes, as shown in Fig. 3.25.

In general, the following effects contribute to the measured signal: Anomalous Hall effect (AHE) and transverse AMR (tAMR) to  $R_{xy}$ ; non-crystalline anisotropy magnetoresistance (ncAMR) and crystalline anisotropy magnetoresistance (cAMR) to  $R_{xx}$ . The cAMR in our polycrystalline samples is caused by broken symmetry in the z-direction and cAMR is therefore present only when magnetization rotates to out-of-plane. Note that the tAMR contains only ncAMR contribution (no cAMR is measured on  $R_{xy}$  contacts).

tAMR and AMR contribution to the signal when magnetization rotates in-plane are shown in Fig. 3.29 (a) and (b) for both the bilayer and trilayer samples. The AMR amplitude is 4.3  $\Omega$  for the reference sample without IrMn and 2.5  $\Omega$  for the trilayer sample, the corresponding tAMR signal has an amplitude of 1.2  $\Omega$  and 0.6  $\Omega$ , respectively. The tAMR and AMR amplitudes are consistent with the dimensions of the Hall bar that contains 3.5 squares. When rotating the magnetization to out-of-plane direction, the  $R_{xy}$  signal is dominated by the AHE, as shown in Fig. 3.29 (c). The  $R_{xx}$  signal when magnetic field rotates out-of-plane (Fig. 3.29 (d)) contains contribution from cAMR and ncAMR.

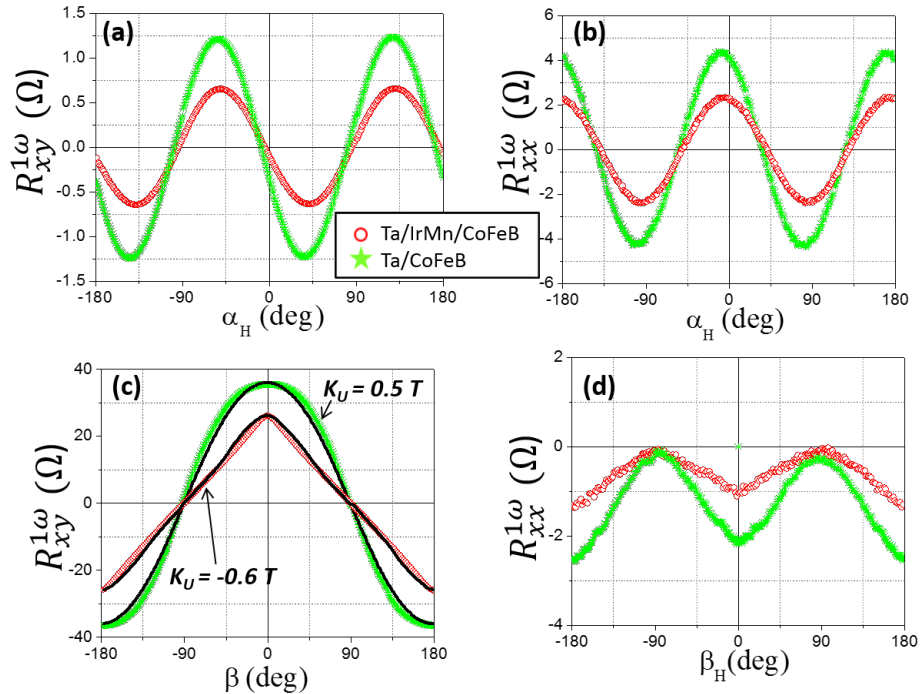


Figure 3.29:  $R_{xy}$  and  $R_{xx}$  signals measured for different planes of magnetic field rotation measured on Ta/IrMn/CoFeB and Ta/CoFeB samples. When magnetic field rotates in-plane ( $\alpha_H$ ) magnetization follows. When magnetic field rotates to out-of-plane ( $\beta_H$ ) the magnetization does not fully follow the magnetic field.

It can be also seen in Fig. 3.29 (c) that, due to the anisotropy of the samples, the magnetization does not fully follow the 1 T magnetic field when rotating out-of-plane, consequently the signal plotted versus magnetic field angle  $\beta_H$  is not perfectly cosine-like function. The anisotropy constant obtained from both the transport and magnetometry data is  $K_u = 0.5 T$  for Ta/CoFeB sample and  $K_u = -0.6 T$  for Ta/IrMn/CoFeB sample. The easy axis of the FM in the trilayer sample is in-plane, the easy axis of the FM in the bilayer sample is out-of-plane. The anisotropy constants were confirmed by SQUID magnetometry.

Since the applied external magnetic field is not strong enough to saturate magnetization along the field direction we have corrected the effect of the anisotropy for deviations from the magnetic field direction when magnetization is rotated out-of-plane. We recalculate the magnetic field angle to the corresponding magnetization angles as illustrated in Fig. 3.30.

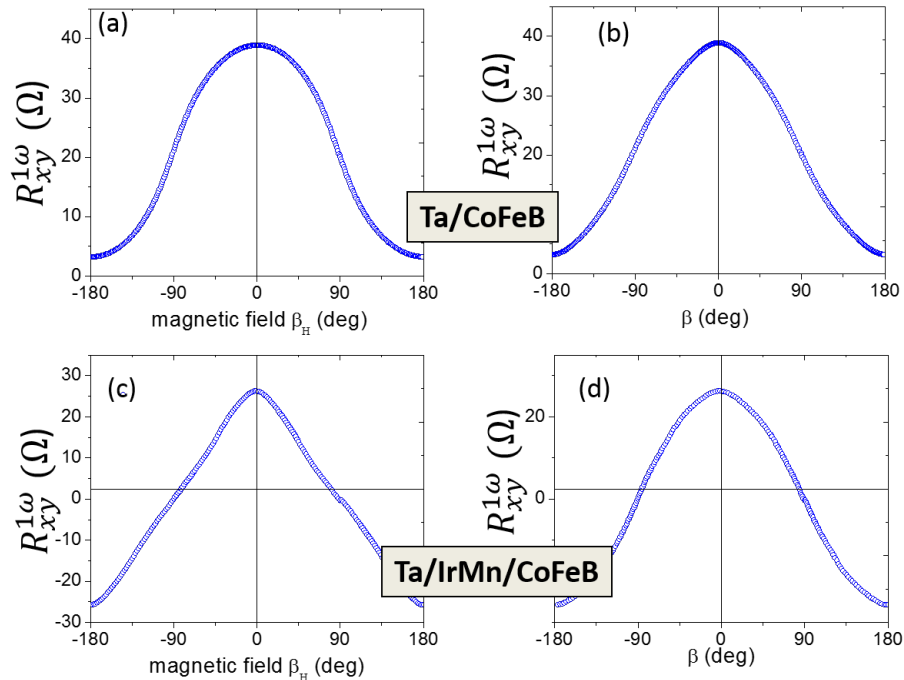


Figure 3.30: (a),(c): The  $R_{xy}$  signal as a function of the magnetic field angle  $\beta_H$  when rotating in the x-z plane for samples Ta/CoFeB and Ta/IrMn/CoFeB, respectively. (b),(d) The same signal plotted as a function of magnetization angle  $\beta$ .

### Symmetry of Effects contributing to the Second Harmonics

In order to analyze the measured signal in the second harmonics we first summarize signals that are expected to contribute, and their corresponding symmetry. We consider the following angular dependencies of magnetotransport effects: ncAMR is determined by the angle between the magnetization and current and has maximum/minimum when the magnetization is along the current direction; cAMR depends on the angle of magnetization from the z-direction and it has a maximum for the out-of-plane magnetization direction. AHE is maximal when

magnetization points out-of-plane of the sample,  $\beta = 0^\circ$ , and minimal when  $\beta = 180^\circ$ , when magnetization is in-plane of the sample the amplitude of AHE is zero. tAMR has symmetry of AMR with maximum/minimum at  $-45^\circ / +45^\circ$ .

When magnetization rotates in-plane of the sample ncAMR and tAMR contributes to the measured signal. When magnetization rotates in x-z plane,  $R_{xy}$  signal is dominated by the AHE and the  $R_{xx}$  signal contains contribution from both cAMR and ncAMR, which in our particular case nearly cancel each other. When magnetization rotates in y-z plane,  $R_{xy}$  is dominated by the AHE and  $R_{xx}$  contains only cAMR contribution.

By considering the symmetry of the magnetotransport coefficients described above and their variation under magnetic field the symmetry of their contribution to the second harmonics can be derived. The details of the derivation can be found in the Appendix A.5. In Tab. 3.2 and 3.3 we show only the final result consisting of the summary of effects contributing to the second harmonics under external magnetic field rotation and their symmetry.

$R_{xy}^{2\omega}$	$\alpha$	$\beta$	$\gamma$
$R_{\text{AHE}}$	$r_{\text{AHE}}H_{AD} \cos \alpha$	$\bar{r}_{\text{AHE}}H_{AD} \sin \beta$	$-\bar{r}_{\text{AHE}}H_F \sin \gamma \cos \gamma$
$R_{\text{tAMR}}$	$r_{\text{ncAMR}}2H_F \cos(2\alpha) \cos \alpha$	$\bar{r}_{\text{ncAMR}}2H_F \text{sgn}(\sin \beta)$	$-\bar{r}_{\text{ncAMR}}2H_{AD} \text{sgn}(\sin \gamma) \cos \gamma$
thermal	$r_{\text{SSE}}\Delta T_{\text{oop}} \cos \alpha$	$r_{\text{SSE}}\Delta T_{\text{oop}} \sin \beta$ $+r_{\text{ANE}}\Delta T_{\text{ip}} \cos \beta$	$r_{\text{ANE}}\Delta T_{\text{ip}} \cos \gamma$

Table 3.2: Contributions to the second harmonic signal in  $R_{xy}$  resulting from the various effects discussed in the text.

$R_{xx}^{2\omega}$	$\alpha$	$\beta$	$\gamma$
$R_{\text{ncAMR}}$	$-r_{\text{ncAMR}}2H_F \sin(2\alpha) \cos \alpha$	$-\bar{r}_{\text{ncAMR}}2H_{AD} \sin(2\beta)$	0
$R_{\text{cAMR}}$	0	$-\bar{r}_{\text{cAMR}}H_{AD} \sin(2\beta)$	$2\bar{r}_{\text{cAMR}}H_F \sin(2\gamma) \cos \gamma$
thermal	$r_{\text{SSE}}\Delta T_{\text{oop}} \sin \alpha$	0	$r_{\text{SSE}}\Delta T_{\text{oop}} \sin \gamma$

Table 3.3: Contributions to the second harmonic signal in  $R_{xx}$ .

These tables summarize the expected contribution to the second harmonic signal including the angular dependency when the magnetization rotates in one of the three planes. The  $r_i$  and  $\bar{r}_i$  coefficients are calibrated using the first harmonic AHE and AMR measurements by considering the total magnetic field including applied magnetic field and the anisotropy field. The anisotropy field is not negligible when magnetization rotates to out-of-plane direction, as was show above. The current induced effective fields  $H_{AD}$  and  $H_F$  can be obtained from the measured second-harmonic transport signals by decomposing the data into the individual angle-dependent terms expected from Tab. 3.3 and Tab. 3.2.

## Measured data on Ta/IrMn/CoFeB Hall bars

In this section we show and discuss the first ( $R^{1\omega}$ ) and the second ( $R^{2\omega}$ ) harmonic signal measured on the trilayer Ta/IrMn/CoFeB and the reference bilayer Ta/CoFeB.

**Magnetic Field Sweep** In order to confirm the magnetic origin of the second harmonic resistance signals, we performed transport measurements while sweeping the magnetic field in-plane of the sample. The data measured on transverse contacts for two different current densities are shown in Fig. 3.31.  $R_{xy}^{1\omega}$  for the two different current densities, the visible difference is caused by temperature drift of the measurement during the low current density measurement.

The  $R_{xy}^{2\omega}$  signal clearly increases with increasing current density, moreover the data reflect also the hysteretic magnetization switching. The switching field is broader than what we observed in SQUID in left panel in Fig. 3.9, which is due to the different domain structure and pinning in the bare wafer (used in a SQUID experiment) and a patterned Hall bar measured in a transport experiment. The weak exchange bias measured in SQUID reaches values only few Oersted which is below the resolution of magnetic field in the cryostat.

At higher magnetic fields the second harmonic signal slowly decreases to zero as expected for an effective field that is decreasing with the amplitude of the applied external magnetic field.

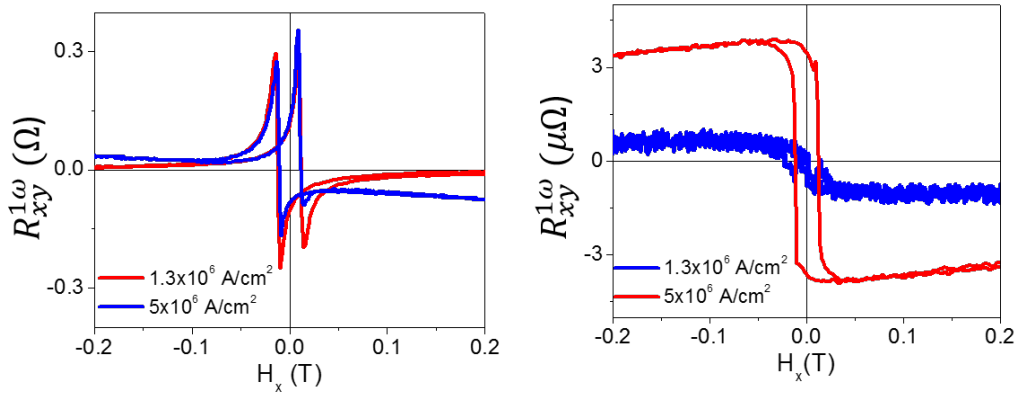


Figure 3.31: First (left panel) and second (right panel) harmonic signal measured on transverse contacts at two current densities. The second harmonic signal increased with current density. Both  $R_{xy}^{2\omega}$  and  $R_{xx}^{2\omega}$  follow a hysteretic variation corresponding to the magnetization reversal in the patterned bar structure.

**Magnetic Field Rotations** Transverse and longitudinal signals were systematically measured when magnetic field higher than saturating field was rotated in all three planes, shown in Fig. 3.25. First and second harmonic signals were recorded at various current densities at 300 K and 5 K. For one particular current density  $j = 3.5 \times 10^6$  A/cm<sup>2</sup> at 5 K, first harmonics and corresponding second harmonics for all three planes of magnetization rotation are shown in Fig. 3.32 and Fig. 3.33 for Ta/IrMn/CoFeB and reference Ta/CoFeB samples, respectively.

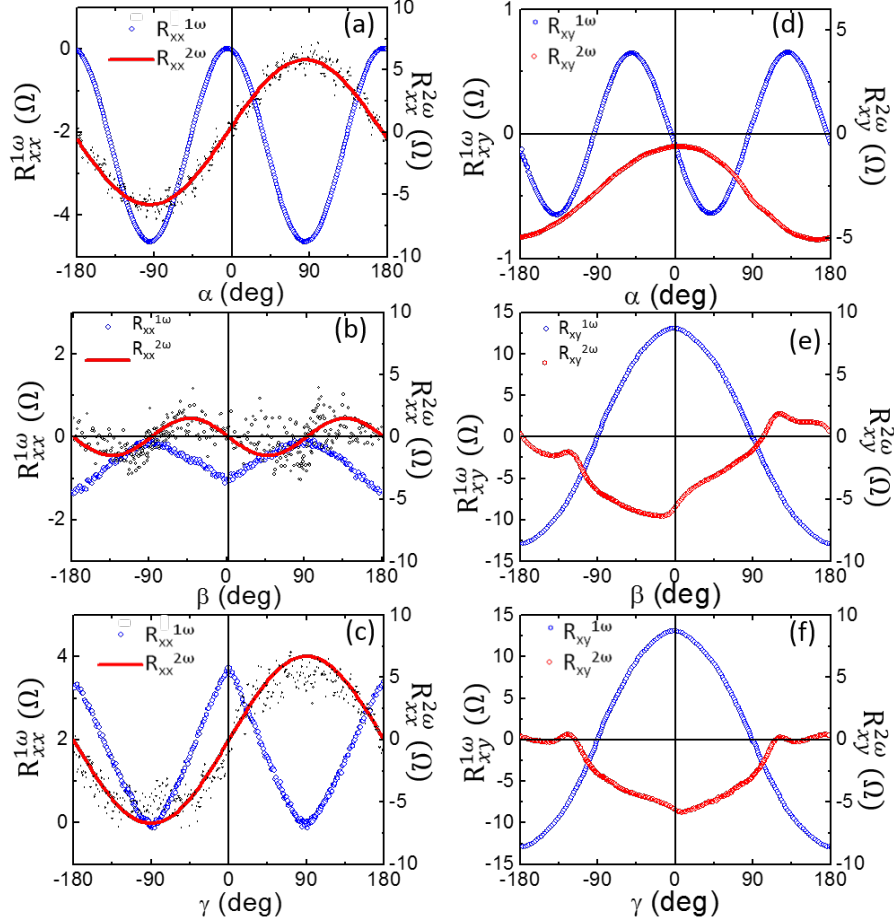


Figure 3.32: Sample Ta/IrMn/CoFeB - an example of measured data. First harmonics (blue) and second harmonics (red) when magnetization rotates in all three planes measured on longitudinal (panels (a)-(c)) and transverse (panels (d)-(f)) contacts. Data are measured at 5K at  $j = 3.5 \times 10^6$  A/cm<sup>2</sup>.

Data were measured at 5 K when IrMn is AFM and at 300 K, above  $T_N$  of 1 nm, in paramagnetic phase of IrMn. For  $\alpha$  rotation the data measured at two temperatures are shown in Fig. 3.34. Note that the relative amplitudes of signals measured at 300 K in Figs. 3.34(a),(d) scale with the aspect ratio of the transverse and longitudinal dimensions of the Hall bar. This all suggests that the  $R_{xx}^{2\omega}$  and  $R_{xy}^{2\omega}$  signals above  $T_N$  are dominated by the same mechanism. It could be in principle due to the Anomalous Nernst effect (ANE) or the spin Seebeck effect (SSE). Both effects have the same symmetry. However, it can be seen in Fig. 3.34 that the sign of this effect is opposite in the Ta/IrMn/CoFeB and Ta/CoFeB samples which implies that the effect is due to the SSE.

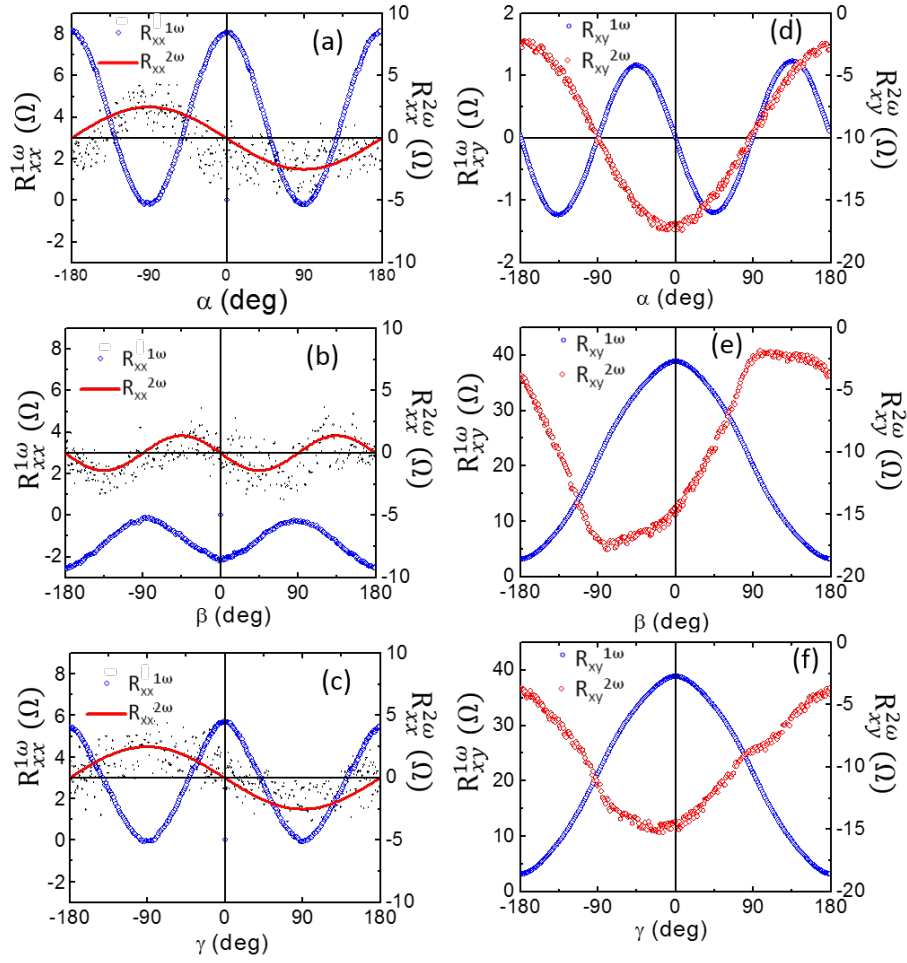


Figure 3.33: Reference sample Ta/CoFeB without IrMn - an example of measured data. First harmonics (blue) and second harmonics (red) when magnetization rotates in all three planes measured on longitudinal (panels (a)-(c)) and transverse (panels (d)-(f)) contacts. Data are measured at 5K at  $j = 3.6 \times 10^6$  A/cm<sup>2</sup>.

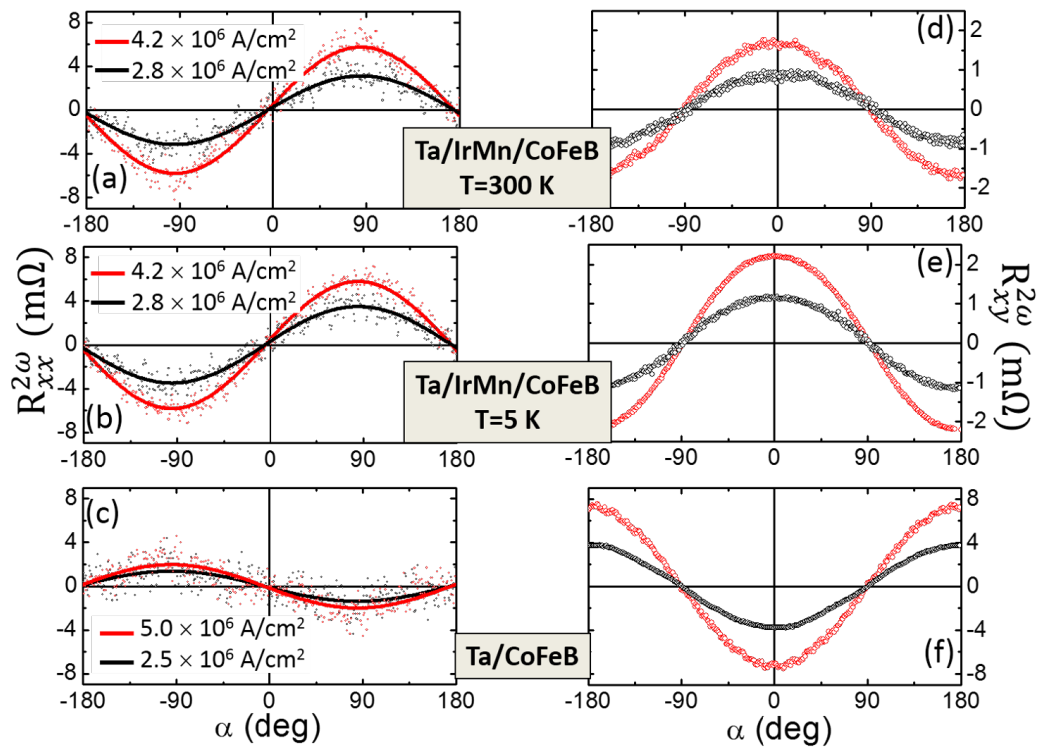


Figure 3.34: An example of data measured at 5 K and 300 K where IrMn is AFM and paramagnetic, respectively. Second harmonics for two different current densities when magnetization rotates in-plane of the sample.

## Analysis of Measured Data

The first harmonic signal contains the contribution described above in the section, tAMR in  $R_{xy}^{1\omega}(\alpha)$ , AHE in  $R_{xy}^{1\omega}(\beta)$  and  $R_{xy}^{1\omega}(\gamma)$ , cAMR in  $R_{xx}^{1\omega}(\gamma)$  and ncAMR in  $R_{xx}^{1\omega}(\alpha)$  and  $R_{xx}^{1\omega}(\beta)$ . The second harmonic signal measured on longitudinal contacts (Fig. 3.32, 3.33, panels (a)-(c)) is for all three angles of magnetization rotation dominated by a single harmonic function. The second harmonic signal measured on transverse contacts is more complex, in particular for the out-of-plane rotation planes ( $\beta$ ,  $\gamma$ ). In order to analyze separately the different angular frequencies of the magnetization rotation, the second harmonic signal in  $R_{xy}^{2\omega}$  was decomposed into Fourier series.

**Fourier Analysis of the Second Harmonic Signal** Because the second harmonic transverse signal ( $R_{xy}^{2\omega}$ ) can be complex due to various contributions, the analysis of measured data was made by Fourier analysis. Data, which are periodic with respect to the magnetic field rotation, were decomposed into sums of sines and cosines

$$f(\xi) = \sum_{n=1}^N (a_n \sin(n\xi) + b_n \cos(n\xi)) + \text{offset}. \quad (3.5)$$

where coefficients  $a_n$  and  $b_n$  are defined as

$$a_n = \frac{1}{\pi} \int_0^{2\pi} f(\xi) \sin(n\xi) d\xi; \quad b_n = \frac{1}{\pi} \int_0^{2\pi} f(\xi) \cos(n\xi) d\xi \quad (3.6)$$

where  $f(\xi)$  is the measured signal and  $\xi = \alpha, \beta, \gamma$  are the angles of rotation.

The coefficients  $a_n$  and  $b_n$  are reflecting which angular frequencies are contributing to our signal. After the Fourier decomposition we look at each of these coefficients (until  $N=5$ ) as a function of current density dependence  $j$ . The results of the decomposition are shown in Fig. 3.35-3.37.

Those Fourier components that are linearly increasing with current are highlighted by solid line in Fig. 3.35-3.37. By comparing these results with Tab. 3.2 we can see that the measured data are consistent with the expected contributions: for the in-plane rotation (Fig. 3.35) the only  $j$ -dependent contributions is  $\cos \alpha$ , which corresponds to SSE and  $H_{AD}$ . In the  $\beta$ -rotation (Fig. 3.36) the linearly increasing contribution is  $\sin \beta$  as expected from Tab. 3.2 for SSE and  $H_{AD}$ .

In the  $\gamma$ -rotation (Fig. 3.37) no linearly increasing contribution can be clearly identified because of the small amplitude of tAMR compared to the large AHE. All other terms, except for the  $\cos \beta$  and  $\cos \gamma$  components, are negligible which implies that we do not observe a sizable  $H_F$  field in our measurements.

The strong  $\cos \beta$  and  $\cos \gamma$  contributions are attributed to the in-plane thermal gradient. As expected for the ANE, generated in the FM due to the temperature gradient along current direction, the terms have the same sign in the Ta/IrMn/CoFeB and Ta/CoFeB samples. The different scaling with applied current, compared to the out-of-plane thermal gradient effect, might reflect the different Joule heating characteristics in the geometry when electrons drift along the thermal gradient. The drifting electrons between the warmer and colder longitudinal contacts will tend to equilibrate the system, resulting in the weak net

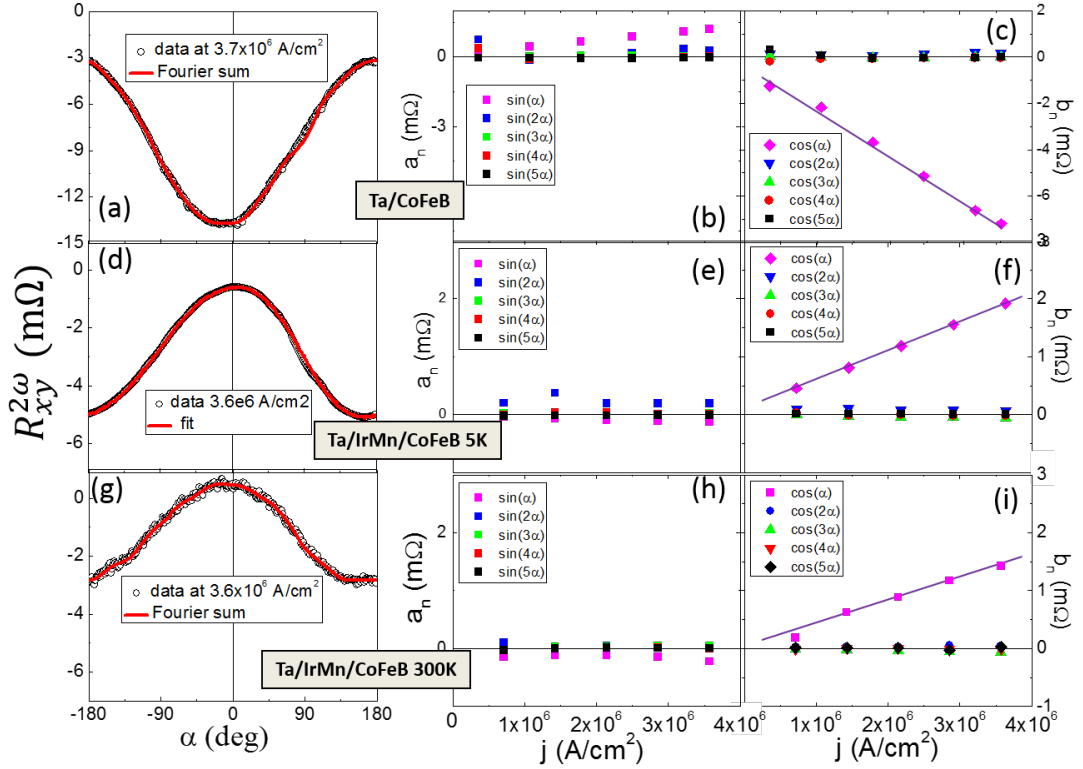


Figure 3.35: Analysis of  $\alpha$ -rotation for reference sample Ta/CoFeB ((a)-(c)) and sample Ta/IrMn/CoFeB below ((d)-(f)) and above ((g)-(i))  $T_N$  (IrMn). Left column: The  $R_{xy}^{2\omega}(\alpha)$  signal (black circles) when magnetization is rotated in-plane and the corresponding Fourier sum fitting (red line). Middle and right columns: Inferred Fourier coefficients as a function of the current density.

dependence of the corresponding  $R_{xy}^{2\omega}$  component on current. The observed angular dependence does not contain terms with frequency corresponding to a current induced torque acting on the CoFeB FM due to the interface iSGE field of Rashba symmetry or Oersted field (which has the same symmetry). The same argument is valid for  $R_{xx}^{2\omega}$  where the only  $j$ -dependent term is proportional to  $\sin \alpha$ , indicating that only a thermal contribution is present. Moreover, for the estimated Oersted field of 0.1 mT, the applied field of 1 T, and for the AMR amplitude in our sample, the  $R_{xx}^{2\omega}$  signal due to the Oersted field is  $\sim 10^{-4} \Omega$ , i.e., within the noise in Fig. 3.34 (a)-(c).

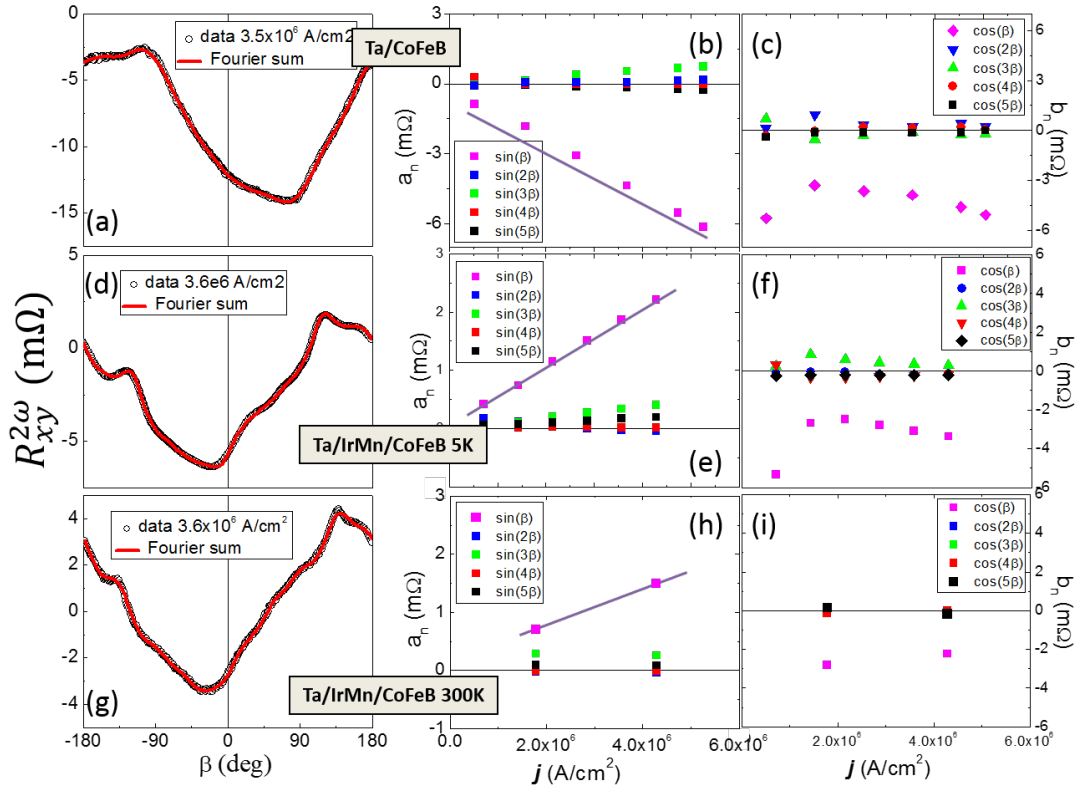


Figure 3.36: Analysis of  $\beta$ -rotation for reference sample Ta/CoFeB ((a)-(c)) and sample Ta/IrMn/CoFeB below ((d)-(f)) and above ((g)-(i))  $T_N$  (IrMn). Left column: The  $R_{xy}^{2\omega}(\beta)$  signal (black circles) when magnetization is rotated in-plane and the corresponding Fourier sum fitting (red line). Middle and right columns: Inferred Fourier coefficients as a function of the current density.

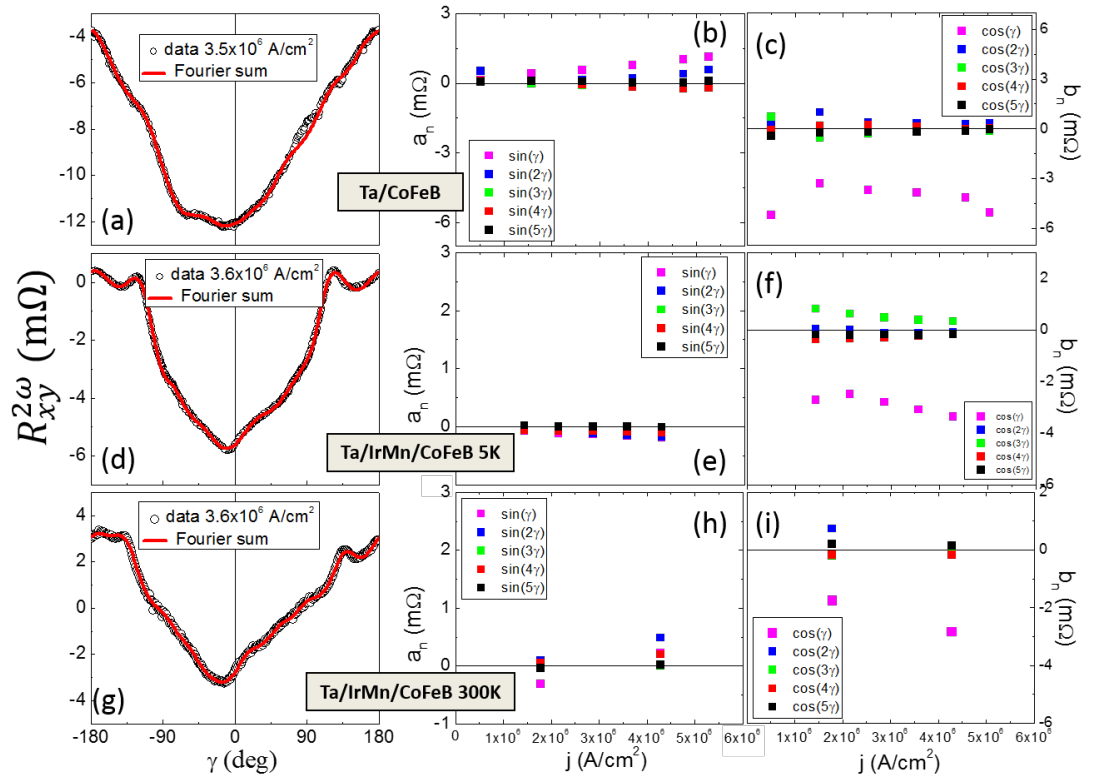


Figure 3.37: Analysis of  $\gamma$ -rotation for reference sample Ta/CoFeB ((a)-(c)) and sample Ta/IrMn/CoFeB below ((d)-(f)) and above ((g)-(i))  $T_N$  (IrMn). Left column: The  $R_{xy}^{2\omega}(\gamma)$  signal (black circles) when magnetization is rotated in-plane and the corresponding Fourier sum fitting (red line). Middle and right columns: Inferred Fourier coefficients as a function of the current density.

**Antidamping-like Field Evaluation** The longitudinal signals  $R_{xx}^{2\omega}(\alpha)$  and  $R_{xx}^{2\omega}(\gamma)$  are dominated by  $\sin \alpha$  and  $\sin \gamma$  in both samples Ta/IrMn/CoFeB and Ta/CoFeB. Following Tab. 3.3 it can be seen that neither antidamping-like effective field  $H_{AD}$  nor Rashba effective field  $H_F$  would generate this signal via AMR. In the same table it can be seen that the sin-like function could be explained by thermal effects. As mentioned earlier SSE can (unlike ANE) explain the change of the sign between the samples with and without IrMn. SSE is generated by  $T_z$  which injects a spin current from CoFeB into the adjacent layer where the spin current is converted to measured voltage due to the inverse SHE. As was shown in literature Ta and IrMn has opposite spin Hall angle [115, 82] which is in agreement with our data in Fig 3.35 and 3.37, where the  $R_{xx}^{2\omega}$  has opposite amplitude for the bilayer and trilayer samples. The thermal gradient is generated by Joule heating and therefore should scale quadratically with current. The measured voltage is, however, divided by applied current and thus the thermal contribution increases linearly with current density. This is in agreement with our measurement.

Although the data measured in  $R_{xx}^{2\omega}$  do not contain information about the current induced torques, we could use them in further analysis. The dominant contribution in  $R_{xy}^{2\omega}(\alpha)$  is  $\cos \alpha$  function, as can be seen in Fig. 3.35(c). Following Tab. 3.2 we can see that  $\cos \alpha$  dependency corresponds to the sum of SSE and  $H_{AD}$  via AHE. However, in Fig. 3.34 it was shown that for  $\alpha$ -rotation at 300 K the amplitude of  $R_{xx}^{2\omega}(\alpha)$  and  $R_{xy}^{2\omega}(\alpha)$  scale with the number of squares in the Hall bar. Therefore the transverse second harmonic signal  $R_{xy}^{2\omega}(\alpha)$  at 300 K reflects only SSE.

When the same measurement is repeated below the  $T_N$  of IrMn the situation changes. The  $R_{xx}^{2\omega}(\alpha)$  remains unchanged since SSE is generated by Joule heating induced thermal gradient which does not change significantly between 300 K and 5 K. This implies that the SHE in IrMn is not different at 5 K and 300 K. The  $R_{xy}^{2\omega}(\alpha)$  signal is, however, different at 5 K. The transverse and longitudinal signal do not scale anymore when taking the number of squares into account and therefore another contribution is present at 5 K. From the symmetry arguments an antidamping-like field driven by an out-of-plane current-induced field and detected by  $R_{xy}^{2\omega}$  via the AHE can explain the observed low temperature data.

To link our measured data to the previously studied system, the same analysis was done for reference sample Ta/CoFeB which shows similar behavior at high and low temperature. Also in this sample the  $R_{xy}^{2\omega}(\alpha)$  and  $R_{xx}^{2\omega}(\alpha)$  in Fig. 3.34 do not scale with the Hall bar aspect ratio and the missing term is attributed to  $H_{AD}$ . It can be seen already in Fig. 3.35 (c) and (f) that the sign of the  $H_{AD}$  amplitude is opposite for the samples Ta/CoFeB and Ta/IrMn/CoFeB.

A more systematic comparison of the current induced effects can be done. Only the SSE contributes to  $R_{xx}^{2\omega}(\alpha)$ . In case of  $R_{xy}^{2\omega}$  both SSE and current induced field due to the out-of-plane oriented antidamping field  $H_{AD}$  contribute to the term with  $\cos \alpha$  symmetry, the thermal part can be removed by subtracting the  $\sin \alpha$  component of  $R_{xx}^{2\omega}$  data (by taking the Hall bar aspect ratio into account). We express the remaining  $R_{xy}^{2\omega}$  signal in terms of the out-of-plane current induced field  $H_{AD}$ .

The antidamping-like effective field in units of  $\text{m}\Omega$  was recalculated to units of  $\text{mT}$  by first determining the out-of-plane tilt angle  $\Delta\theta$  using the measured

AHE amplitude as a calibration. Note that in our notation (Fig. 3.25)  $\theta = 90^\circ$  corresponds to magnetization in-plane, therefore a small tilt from the sample plane leads to  $\theta = 90^\circ - \Delta\theta$ . Then  $H_{AD}$  was inferred by taking into account the out-of-plane anisotropy field  $H_U$  and the applied external magnetic field  $H_{ex}$ . For this we use the angular dependency of the total energy

$$E_{\text{tot}} = MH_{\text{ex}} \sin \theta + \frac{MH_U}{2} \cos^2 \theta + MH_{AD} \cos \theta \quad (3.7)$$

where  $\theta$  is out-of-plane angle of the magnetization. The anisotropy field of our samples is -0.6 T and +0.5 T for the samples with and without IrMn, respectively. The energy minimum is calculated from

$$\frac{dE}{d\theta} = 0 = MH_{\text{ex}} \cos \theta - MH_U \cos \theta \sin \theta - MH_{AD} \sin \theta. \quad (3.8)$$

To evaluate the  $H_{AD}$  from the in-plane rotation ( $\alpha$ ) we can simplify the Eq. 3.8 by considering  $\theta \sim 90^\circ$ , therefore  $\sin \theta \sim 1$  and  $\cos \theta \sim \Delta\theta$ . Equation 3.8 can be then simplified to

$$H_{AD} \sim \Delta\theta(H_{\text{ex}} - H_U). \quad (3.9)$$

The summary of SSE and  $H_{AD}$  evaluation is in Fig. 3.38. The SSE and  $H_{AD}$  were evaluated from all three magnetization rotation planes giving similar values as shown in Fig. 3.38.

The data in Fig. 3.38 confirm the opposite sign of the SSE and of  $H_{AD}$  in the Ta/CoFeB and Ta/IrMn/CoFeB stacks which we associated above with the opposite sign of the SHE angles in Ta and IrMn. They also confirm the linear dependence of the SSE and  $H_{AD}$  signals on the amplitude of the applied current, and vanishing  $H_{AD}$  in the high-temperature phase of IrMn. The fact that the  $H_{AD}$  signal appears in the Ta/IrMn/CoFeB stack only below  $\sim 100$  K may be related to antidamping torque on AFM coupled moments in IrMn below  $T_N$ .

**Discussion** As mentioned above the SSE signal did not change significantly between 5 K and 300 K implying temperature independent inverse SHE in IrMn. The  $H_{AD}$  generated by SHE is, however, present only at low temperature in Ta/IrMn/CoFeB sample and it oscillates around zero until the  $T_N$  as shown in Fig. 3.39. The reason for the different temperature dependencies of the two contributions is in the sample stack we use. The SSE is generated in CoFeB and injected to IrMn, where is most of the spin current absorbed. The SHE causing the current induced torque is, on the other hand, generated in both Ta and IrMn and acting on CoFeB. The spin-current from Ta and IrMn compensate each other at higher temperatures (note that they have opposite spin Hall angle). At low temperature we see strong increase of the torque on CoFeB, which, considering its sign, comes from IrMn. The suppression of SHE generated in Ta can be explained by spin current absorption by IrMn AFM moments.

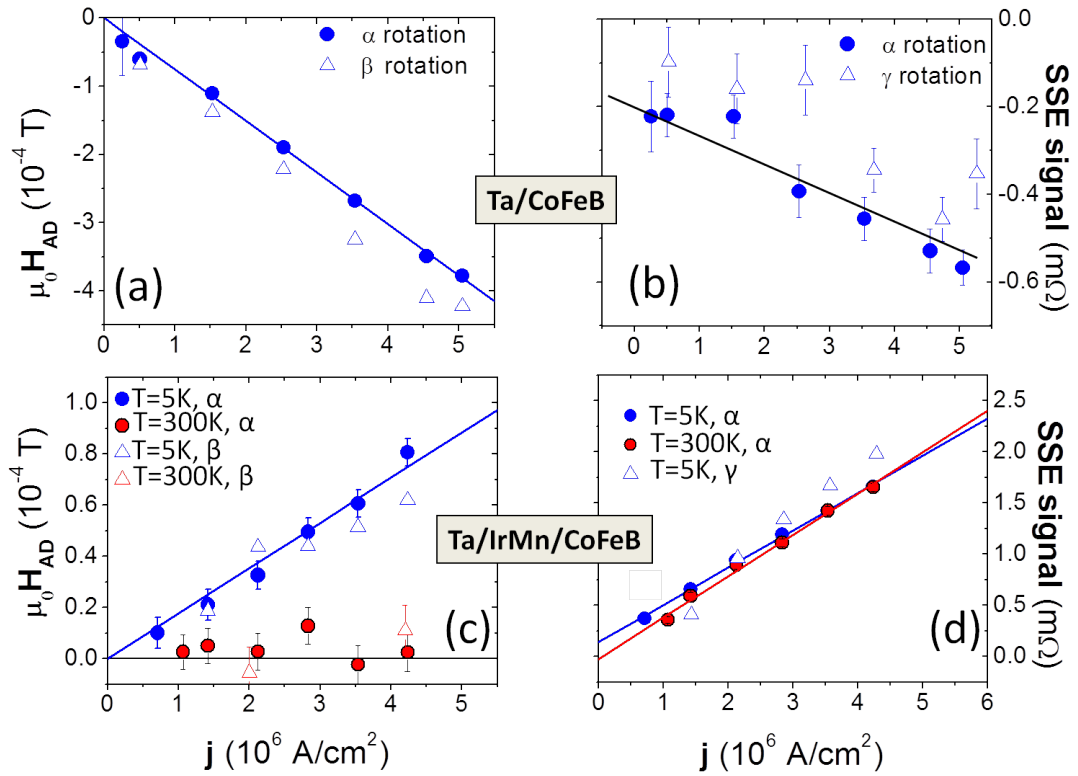


Figure 3.38: (a) Current density dependence of the current induced effective out-of-plane field  $\beta$  rotation (triangles). (b) Current density dependence of the SSE contribution recalculated for one square obtained from  $\alpha$ -rotation (blue dots) and  $\gamma$ -rotation (triangles). (c,d) Same as (a,b) for the Ta/IrMn/CoFeB sample at 5 K (blue) and 300 K (red).

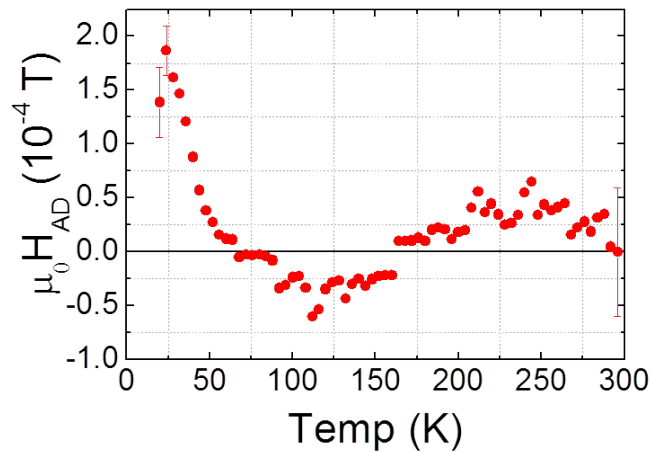


Figure 3.39: Temperature dependence of antidamping-like effective field measured on sample Ta/IrMn/CoFeB. The strong increase of current induced torque coincides with expected  $T_N$  of thin IrMn.

### 3.6.7 Samples with Ta/IrMn

It was shown in the previous section that the current induced torque acts on AFM coupled moments at low temperature. In the next experiment we therefore focused on a structure consisting only from interface Ta/IrMn. In this case we, however, can not expect the AHE of the FM layer as a sensitive detector and we have to use directly IrMn which also should show AMR. To manipulate IrMn moment to different orientation we have used a method described in the chapter 3.5 - cooling in magnetic field. Due to the ultrathin thickness of IrMn layer we could cross the  $T_N$  and study the current induced effect both in AFM and paramagnetic phase of IrMn. The wafer had following stack of layers: Ta( $5 \pm 0.2$  nm)/IrMn( $1.3 \pm 0.3$  nm)/MgO( $1.4 \pm 0.2$  nm)/AlO<sub>x</sub>(10 nm). The same Hall bar design shown in Fig. 3.25 was used to measure the first and second harmonic signal while the Hall bar was cooled in different magnetic field orientations through  $T_N$ . The  $R_{xy}^{1\omega}$  and  $R_{xy}^{2\omega}$  signal was measured when cooling the sample in 2 T magnetic field in-plane and out-of-plane of the sample. A clear onset of non-zero differences  $\Delta R_{xy}^{1\omega}$  and  $\Delta R_{xy}^{2\omega}$  between the two field cooling direction can be seen in Fig. 3.40, indicating the appearance of ncAMR and current induced torque on AF-coupled moments in IrMn. The  $R_{xy}^{2\omega}$  signal is independent on magnetic field orientation at high temperature and it becomes field sensitive below the expected  $T_N$ . This implies magnetic origin of the signal and a current induced torque acting on IrMn AFM moments giving rise to the second harmonic signal.

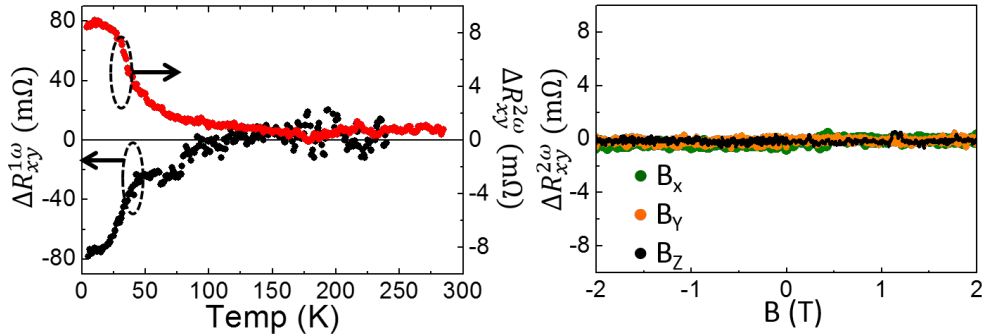


Figure 3.40: Current induced effects in Ta/IrMn sample with no ferromagnet. Left: Difference between cooling Hall bar with 2 T magnetic field in-plane and out-of-plane of the sample. Splitting of first (black) and second (red) harmonics on transverse contacts at expected  $T_N$  of thin IrMn. Right: Once the AFM moments are cooled below  $T_N$  they can not be manipulated by external magnetic field in any direction.

Once the AFM moments are cooled below the  $T_N$  they should be rigid and insensitive to an external magnetic field. To prove that our signal originates in AFM moments we have measured at low temperature the second harmonic signal while sweeping magnetic field in all three directions. The results can be seen in Fig. 3.40 (right). The signal is completely insensitive to the applied field.

The measurements on Ta/IrMn samples were repeated on several samples, all showing splitting of the first and second harmonic signal at similar temperature. However, the values of the  $R_{xy}^{2\omega}$  varied from sample to sample and thus any detailed

analysis, as in the previous section, could not be performed. We assume the irreproducibility is caused by different domain structure in every cooling cycle.

### **3.6.8 Summary of Current Induced Manipulation of AFM Moments**

We have studied current induced torques acting on polycrystalline IrMn interfaced with Ta. By systematic measurement of second harmonic signal and symmetry analysis we could identify a contribution from antidamping-like effective field which acts on CoFeB in contact with IrMn. We further found different behavior of the Ta/IrMn/CoFeB system above and below the  $T_N$  of IrMn. Samples without FM exhibit splitting at  $T_N$  of the second harmonic signal depending on the orientation of the cooling field. All the experiment could be consistently explained by current induced torque absorbed by IrMn moments.

# 4. New Materials for Antiferromagnetic Spintronics

In Chap. 3 we have discussed the ways of manipulation with the AFM ordered moments. The material which we used throughout all the experiments of Chap. 3 was metallic alloy  $\text{Ir}_{0.2}\text{Mn}_{0.8}$ , widely used in electronic industry for MTJ fabrication. However, one of the strong motivations for the AFM spintronics research is surprisingly large number of materials which at room temperature exhibit AFM ordering simultaneously with semiconductor electronic structure. Such materials - when industrially available - have potential to open important additional routes to spintronic functionality: first, their magnetic properties are likely to be controllable by electric gating; second, they could allow us to integrate nonvolatile magnetic memory with semiconductor logic in one material. In this chapter we focus on first experimental characterization of one representative of this new class of materials - CuMnAs. After explaining its relationship to common semiconductors we perform and discuss basic characterization of chemically synthesized CuMnAs in the second section of this chapter. In the last section epitaxially grown CuMnAs indicating first spintronic functionality is presented.

## 4.1 Route to AFM Semiconductors

Common binary semiconductors of III-V type can be thought of as being derived from elemental group IV semiconductors by transferring one proton between two neighboring atoms. It turns out that compounds derived in this way retain many of the properties of their parents, such as, e.g., similar crystal and electronic structures. By applying this proton transfer rule repeatedly, one can find more distant relatives. Thus, for example, from binary compound of III-V type family of well known semiconductors of II-VI type, as well as family of less known semiconductors of I-II-V type (such as LiMgP, LiZnAs, etc.) can be derived. In the latter case the proton has been transferred to the interstitial space of the zinc-blend crystal lattice, Fig. 4.1(a) and (b), forming lattice of half-Heusler alloys (generally orthorhombic), or a topologically equivalent tetragonal lattice.

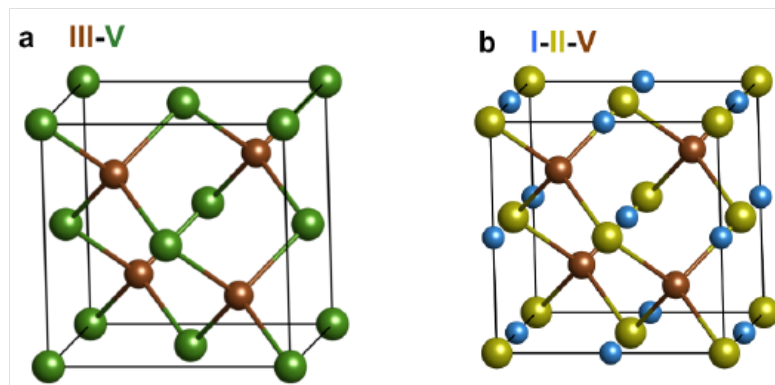


Figure 4.1: Crystal structure of discussed materials. After [24].

Compounds containing unpaired spins may exhibit long-range magnetic ordering. In case of ferromagnets the magnetic atoms can either be the constituting elements of the compound (such as EuO etc), or they can be randomly distributed as impurities in a host lattice (such as Mn in the prototypical diluted magnetic semiconductor (Ga,Mn)As). In the latter case the FM ordering is mediated by itinerant carriers. In contrast, diluted AFMs are unlikely because the AFM materials require the magnetic atoms to form a regular (sub)lattice. Examples of such materials are MnTe among the II-VI semiconductors, or LiMnAs among the I-II-V semiconductors. Some of these materials have already been prepared in thin films by molecular beam epitaxy. Among them, LiMnAs seemed to be particularly appealing for its high  $T_N$ , similar electronic structure to GaAs ( $\Delta E_G \sim 1.5\text{eV}$ ) and good lattice match to other zinc-blend materials (InAs). However, presence of the extremely diffusive and reactive Li turned out to be serious issue both for the fabrication technology and for the long-term stability of the material. To overcome this problem, attempts have been made to replace alkali metal Li by group I(b) elements. Recently, first successful epitaxial growth of CuMnAs has been demonstrated [24]. Theoretically, this material has been predicted to be a robust antiferromagnet, however, with a band gap close to zero (with the uncertainty typical for ab-initio calculations), as shown in Fig. 4.2. In the next paragraphs we examine its basic properties experimentally.

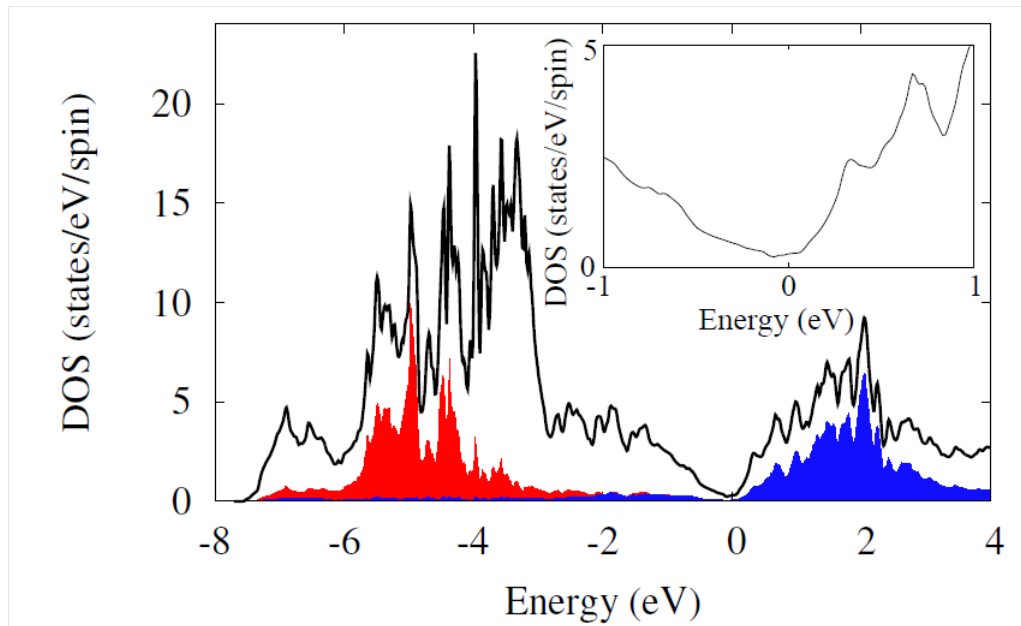


Figure 4.2: CuMnAs density of states diagram. The red (lower energy) and blue (higher energy) color corresponds to DOS projected on spin up (spin down) states of the 1st (2nd) Mn sublattice. Inset shows detail of DOS around zero energy. After [109].

## 4.2 Bulk Orthorhombic CuMnAs

### 4.2.1 Technology of Fabrication

Samples were prepared by O. Stelmakhovych (MFF UK) by direct synthesis from elements mixed in the stoichiometric 1:1:1 ratio using high purity Cu, Mn and As. Samples were heated up to 1000 °C at a rate 1 °C/min and annealed for 1 day. The stoichiometric ratio was confirmed by elemental analysis by energy dispersive X-Ray spectroscopy. The resulting product was silver gray solid rock, an example is shown in the left panel in Fig. 4.3. After synthesis samples were polished using sandpaper and subsequently with diamond paste (starting from 15  $\mu\text{m}$  to 1  $\mu\text{m}$  diameter Buehler MetaDi monocrystalline diamond suspension) in a 90 minutes mechanical polishing. Samples were cleaned using acetone and ethanol. Bars for transport measurement were cut for conductivity measurement, an example of a bar for measurement of longitudinal resistance is in the right panel in Fig. 4.3.

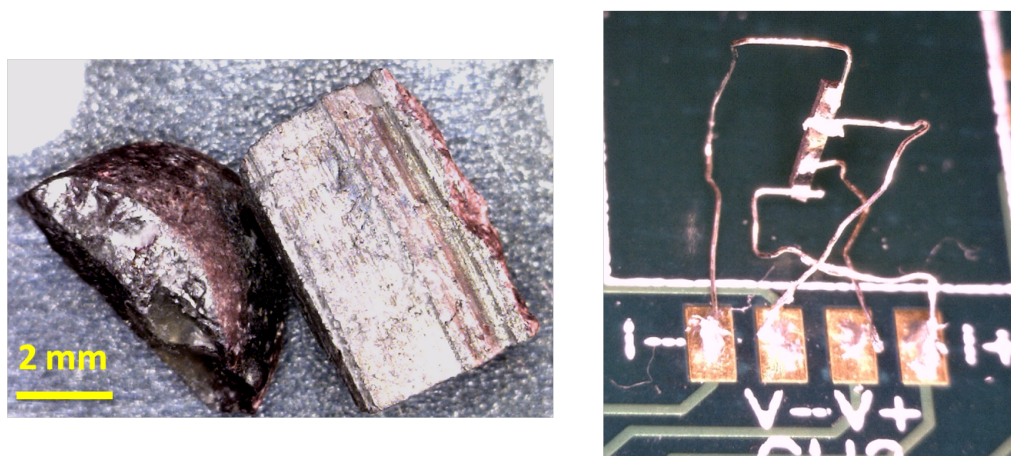


Figure 4.3: Left: Example of the chemically synthesized CuMnAs. Right: Example of a transport bar for a 4-point resistivity measurement prepared from the bulk material by polishing, cutting and soldering the contacts.

### 4.2.2 Structural Analysis

The bulk samples were characterized by XRD by X. Marti (MFF UK). The results are shown in Fig. 4.4. XRD indicated that the samples are highly textured although far from single crystalline. To compare the XRD image with the powder diffraction, intensity is radially integrated, therefore the two-dimensional graph is reduced to a one dimensional plot (blue curve). It confirms that all reflections correspond to CuMnAs orthorhombic Pnma structure in agreement with powder diffraction patterns (red line) obtained from the ICSD database.

### 4.2.3 Magnetic Characterization

The polished and bulk samples were characterized by SQUID magnetometry. For measurement at up to 800 K a high temperature inset of SQUID magnetometer was used. For temperatures above 400 K the sample could not be mounted in standard plastic straw used for SQUID measurement, instead the measured

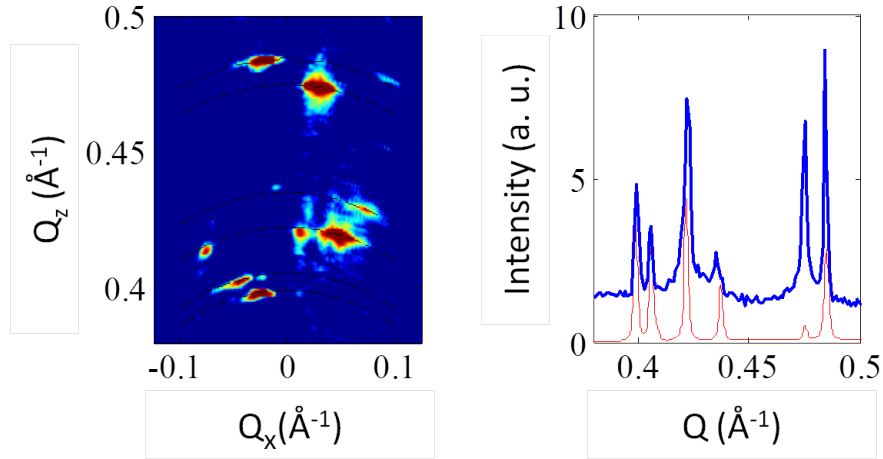


Figure 4.4: Left: XRD patterns of CuMnAs rods collected in co-planar geometry. Data indicates that the sample is constituted by large grains, despite it is not a single crystal. Right: All peaks observed, integrated in  $Q$ -slices (thick line), correspond to CuMnAs powder diffraction patterns (thin line). Measured by X. Marti (unpublished).

sample was mounted in aluminum foil. This allowed us to measure the susceptibility in the range between 5 K and 800 K. The susceptibility measured in 0.5 T is shown in the left panel in Fig. 4.5, a clear peak indicating the critical  $T_N$  of CuMnAs can be seen. In the right panel in Fig. 4.5 is shown magnetization loop measured at 300 K showing no net magnetic moment.

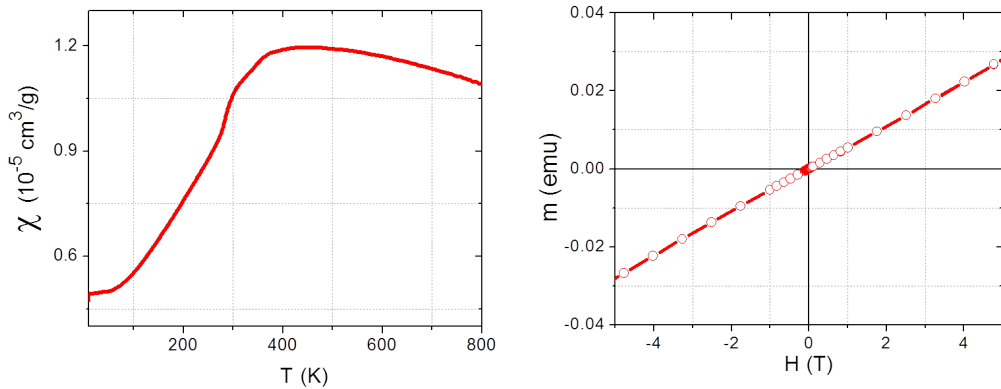


Figure 4.5: Left: Magnetic susceptibility of CuMnAs. The peak in susceptibility corresponds to  $T_N$ . Right: Magnetization loop at 300 K shows no net magnetic moment.

#### 4.2.4 Transport Characterization

The pieces of bulk CuMnAs measured in transport setup up to 400 K show a kink at temperature similar to SQUID measurement. The temperature dependent resistivity is shown in Fig. 4.6, in the same figure, SQUID data are plotted in

order to compare the position of the kink. The critical temperature of bulk orthorhombic CuMnAs was estimated to 380 K.

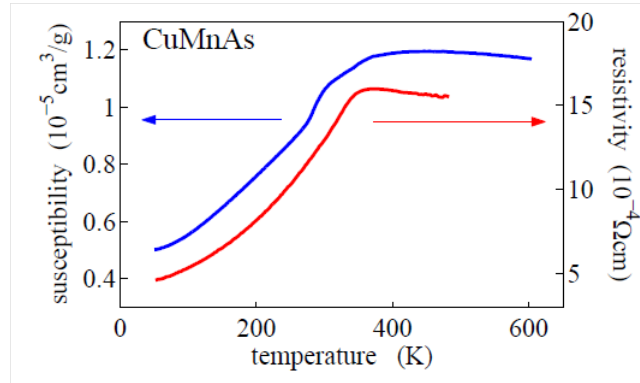


Figure 4.6: Resistivity of CuMnAs. The peak in resistivity (red line) is in good agreement with measured SQUID data (blue line). After [109]

LC15385B

### 4.3 Epitaxial CuMnAs

The orthorhombic crystal structure of the bulk chemically synthesised CuMnAs, shown in left panel of Fig. 4.7, is incommensurable to any common semiconductor substrate. However, it turned out that when grown by molecular beam epitaxy, the CuMnAs film crystallizes in tetragonal crystal structure, as shown in right panel of Fig. 4.7. The in-plane lattice constant matches that of GaP or Si and differs only by 4 % from the As-sublattice of GaAs. Spin orientation was measured by neutron diffraction by P. Wadley (University of Nottingham, UK) and spins are indicated by arrows in Fig. 4.7.

The lattice parameters are  $a = b = 3.820 \text{ \AA}$  and  $c = 6.318 \text{ \AA}$  for the relaxed material grown on GaAs.

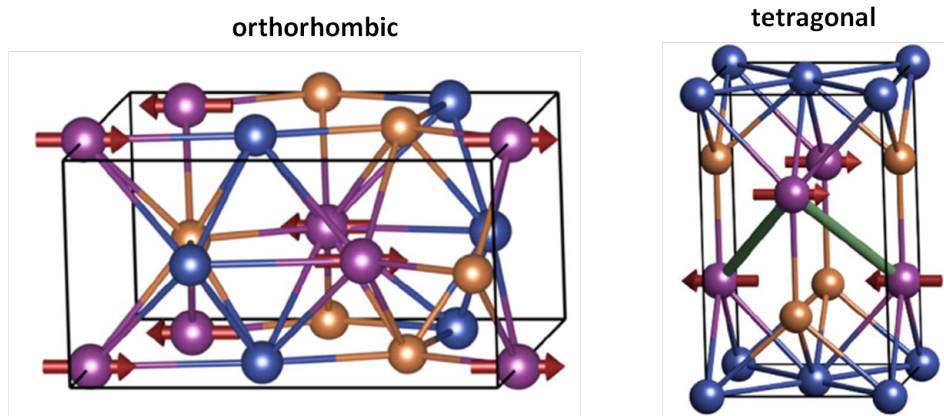


Figure 4.7: Unit cell structure of orthorhombic bulk CuMnAs (left) and epitaxial tetragonal CuMnAs. Spin orientation is indicated by arrows. After [24]

### 4.3.1 Magnetic Characterization

The epitaxial CuMnAs layers were grown at the University of Nottingham by molecular beam epitaxy. The CuMnAs layers were grown on the zincblende GaAs[001] substrate. The growth parameters, in particular the material fluxes, were varied in order to find the optimum growth conditions. The samples were measured in SQUID for their saturated magnetic moment. As seen in Fig. 4.8, all samples grown with Cu flux lower than some critical value exhibit net magnetization, i.e. contain a FM compound. This is attributed to FM MnAs inclusions, the amount of which increases linearly with increasing deficit of Cu. In the optimum, stoichiometric, point the FM compound vanishes and the material shows no magnetization (except of the diamagnetic GaAs substrate), in agreement with an AFM magnetic state.

The absence of net magnetic moment in stoichiometric sample indicated that the sample is indeed compensated AFM. Further confirmation was made by neutron diffraction which confirmed the presence of long range AFM order [24]. The structurally forbidden peak (indicating AFM order) disappeared at 500 K, above the expected  $T_N$ .

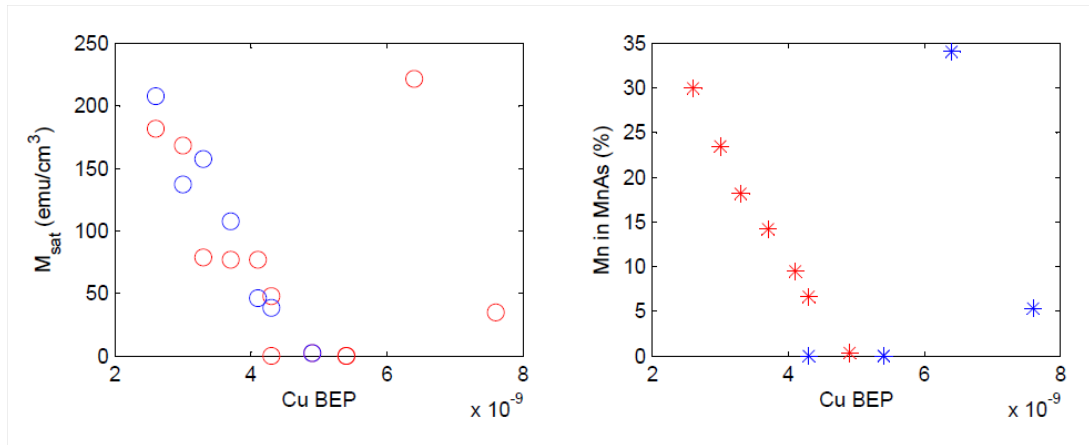


Figure 4.8: Left: Magnetic moment of samples with different copper flux (beam equivalent pressure, BEP) measured at 300 K. Right: Ratio of Mn contributing to MnAs at 300 K. The ratio of Mn contributing to MnAs was estimated by assuming magnetization of MnAs  $\sim 650$  emu/cm<sup>3</sup>

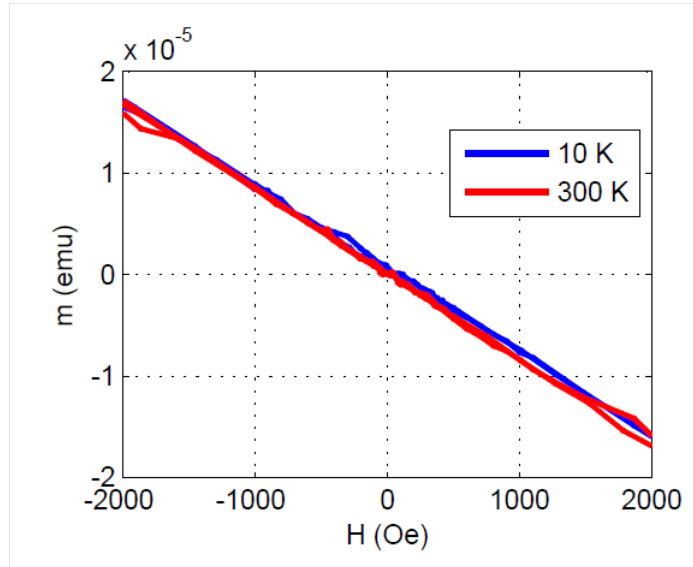


Figure 4.9: Magnetic characterization of CuMnAs with optimal parameters. No net magnetic moment can be observed indicating that only negligible amount of Mn atoms forms FM MnAs. The linear background reflects the diamagnetic silicon substrate.

### 4.3.2 Structural Analysis

The structural properties were studied by combined X-Ray experimental and computational method by P. Wadley (University of Nottingham) [147]. The space group was determined as  $P4/nmn$  and the lattice parameters are  $a = b = 3.820 \text{ \AA}$  and  $c = 6.318 \text{ \AA}$ .

The epitaxial layers were also studied by diffraction by D. Kriegner (JKU, Linz) up to 500 K confirming the stability of the material as shown in Fig. 4.10. The (002) Bragg reflection is seen unchanged after heating to 500 K (top blue line in Fig. 4.10). Furthermore, the tetragonal arrangement was confirmed by J. Gazquez (Oak Ridge National Lab) in Z-contrast scanning transmission electron microscopy along CuMnAs [100] direction. The result is shown in Fig. 4.11, showing well ordered atomically resolved tetragonal structure of CuMnAs.

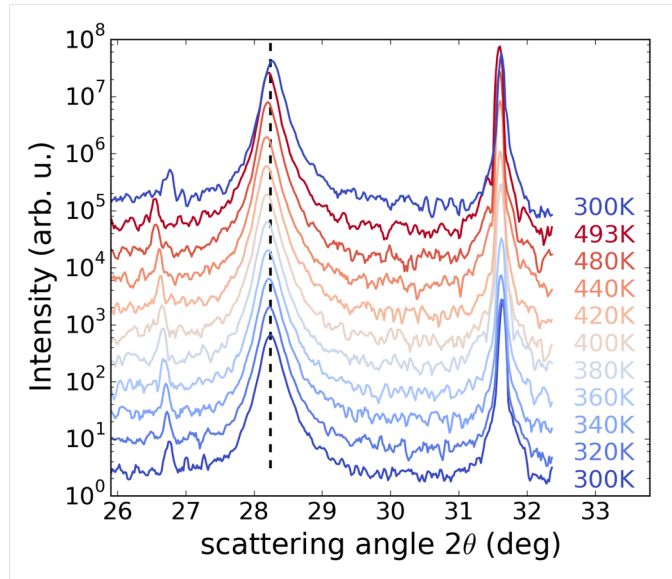


Figure 4.10: XRR study of CuMnAs structure after heating to 500 K. Measurement performed by D. Kriegner (JKU, Linz) with Cu  $K\alpha_1$  radiation (unpublished).

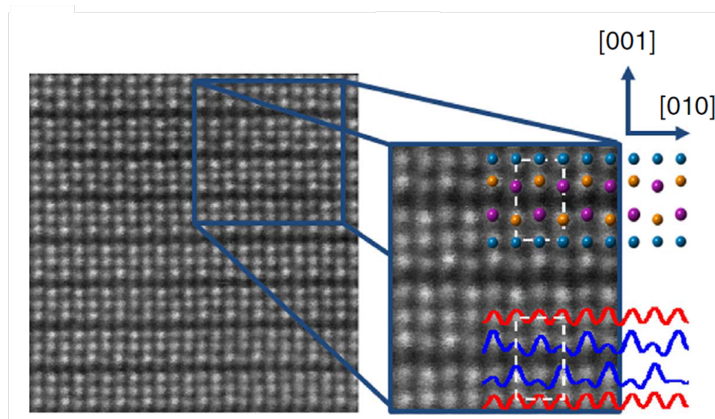


Figure 4.11: Z-contrast scanning transmission electron microscopy image of CuMnAs. The bright atoms correspond to As and they form a triangular structure confirming the X-Ray results. After [24]

### 4.3.3 Transport Characterization

A Hall bar fabricated from stoichiometric CuMnAs sample was measured in temperature range 4 K - 300 K showing increasing resistivity with increasing temperature. This confirms the density of state calculation [24] suggesting the tetragonal CuMnAs is on the boundary between a semiconductor and a semimetal. Carrier density estimated from the Hall measurement is  $1.1 \times 10^{22} \text{ cm}^{-3}$ , close to the number of atoms in the lattice. This is typical for metals and semimetals, consistent with the prediction of the zero band gap.

## 4.4 Exchange Coupling on CuMnAs/Fe Interface

The above mentioned experiments indicate that the stoichiometric CuMnAs is a room temperature AFM. In order to confirm its AFM order and to demonstrate the basic functionality of the new material, an epitaxial bilayer of CuMnAs(30 nm)/Fe(3 nm) was prepared by in-situ growth and exchange coupling on the interface was magnetically studied. Because of the high critical temperature  $T_N$  the SQUID was equipped by a high temperature insert. This allowed us to perform measurements in the temperature range 300 K - 800 K.

CuMnAs/Fe sample was measured in a standard exchange bias procedure. The sample was heated to temperature close to the  $T_N$  of the AFM, cooled in magnetic field to lower temperature (in our case 300 K) and then several magnetization loops were measured. The same procedure was repeated with the cooling field of the opposite polarity. In left panel of Fig. 4.12 we show an exchange bias shift measured at 300 K after cooling in +0.5 T and -0.5 T. The plotted data show a magnetization loop measured directly after cooling in field, and the final (trained) magnetization loop. The exchange shift clearly persists after training and remains symmetric with respect to zero magnetic field.

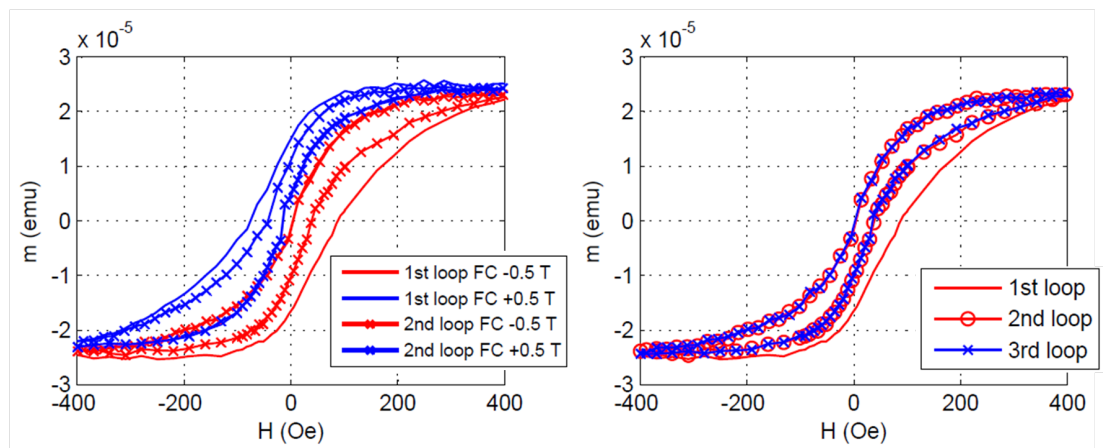


Figure 4.12: Left: Exchange bias at CuMnAs/Fe interface. Right: Effect of training.

The effect of training was further studied after one particular cooling in negative magnetic field. The results are shown in Fig. 4.12 (right). The first measured loop (solid line) shows clear exchange bias and exchange broadening. Both  $H_{\text{eb}}$

and  $H_{ec}$  are reduced after the second (trained) magnetization loop but still the  $m(H)$  is clearly shifted with respect to zero magnetic field. Any further magnetization loop measured (3rd to 10th) did not change the exchange coupling anymore, as indicated by stars in Fig. 4.12 (right). This result shows that the exchange coupling is robust and once the sample is cooled in magnetic field the exchange shift can not be erased by magnetic field cycles.

The measured exchange shift  $H_{eb}$  was reproducible over several samples and reached 20 - 30 Oe. Although this value is not large, it can not be explained by a residual magnetic field in the superconductive magnet which is typically less than 5 Oe, as can be found in the specifications of the instrument. Note that also the stable exchange shift after the first training cycle is not consistent with expected remnant field that should disappear after magnetic field cycling.

#### 4.4.1 Temperature Dependence of Exchange Bias

Another important characteristics of exchange bias is the field cooling procedure. In order to observe symmetric and robust exchange coupling sample needs to be cooled from high enough temperature in vicinity or above  $T_N$  of the AFM. We have systematically measured exchange bias after cooling from different temperatures. As can be seen in Fig. 4.13, the characteristic  $H_{eb}$  is observed only after cooling from 430 K - 440 K (Fig. 4.13 (d),(e)). When cooling from temperature lower than that, the exchange coupling appears but does not exhibit symmetric shift when measured after cooling in magnetic field with opposite polarity.

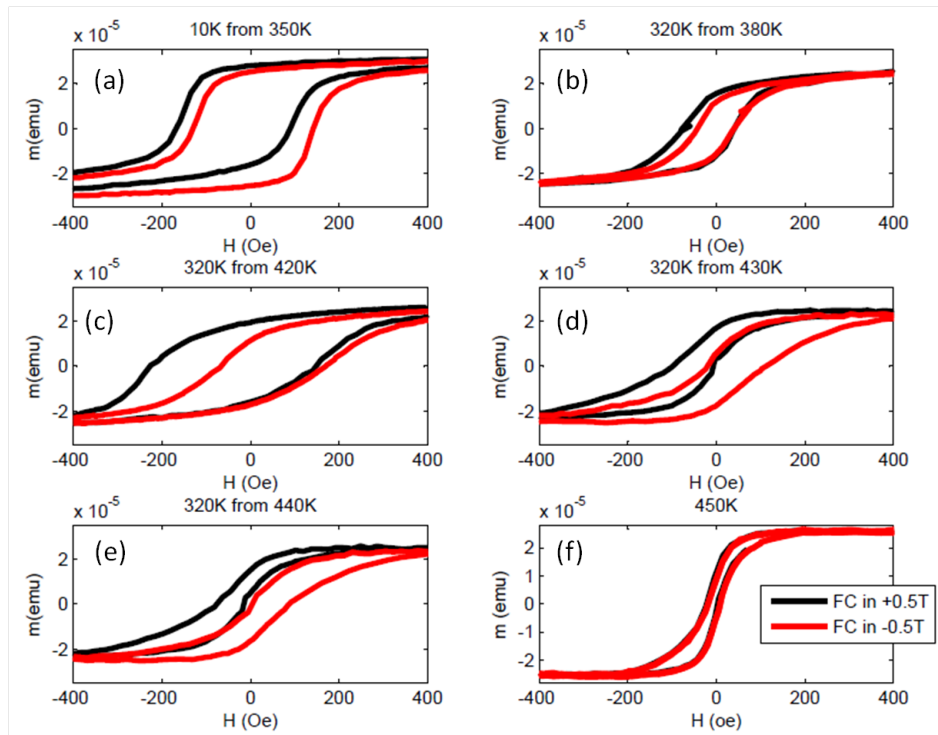


Figure 4.13: Temperature dependence of exchange bias.

When the sample is cooled from 450 K the exchange bias suddenly disappears and the sample does not exhibit any exchange coupling in any field cooling

procedure anymore (Fig. 4.13 (f)). This can be attributed to the interface degradation at elevated temperatures. As was observed also in other systems with thin epitaxial Fe layer [148] high temperature can lead to permanent damage of the interface, and consequently to disappearance of the exchange coupling effect. The permanent structural changes of the interface were confirmed by temperature dependent XRD by D. Kriegner (JKU, Linz). The result of XRD measurements is shown in Fig. 4.14. It can be seen that up to 440 K the sample does not exhibit any significant changes. Once, however, heated above 450 K, the (002) diffraction peak develops a shoulder and finally splits into two distinct peaks which remain when the sample is again measured at 300 K. Complementary XRR measurements performed during the heating confirm that at the same time the roughness of the CuMnAs/Fe interface changes irreversibly. Note, however, that the structural changes are exclusively affecting the interface, because, as shown in Fig. 4.10, CuMnAs itself is not affected at 500 K and the Fe layer does not exhibit clear decrease of magnetic moment in SQUID.

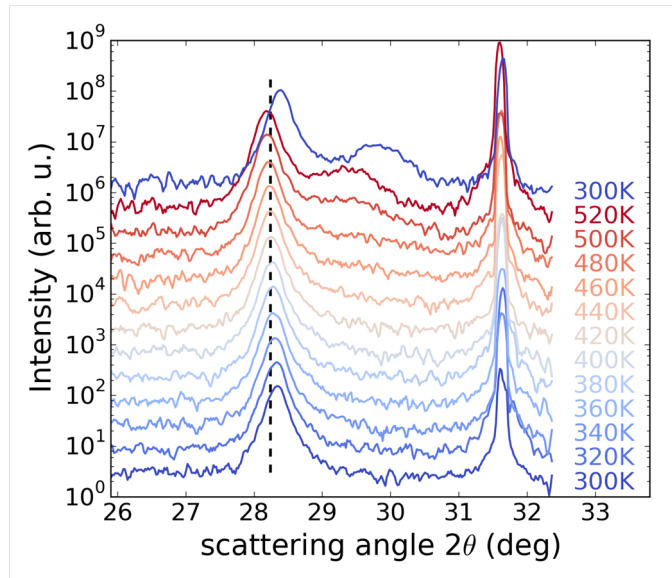


Figure 4.14: Temperature dependent XRD of the epitaxial bilayer CuMnAs/Fe. Structural change is observed when temperature increases above 450 K. The change is irreversible as can be seen from data measured after cooling sample back to 300 K. Measured by D. Kriegner, JKU Linz (unpublished).

#### 4.4.2 Other Possible Sources of $m(H)$ Shift

As already mentioned the remnant magnetic field in superconductive coil can be excluded for several reasons. First argument is the robustness of the  $m(H)$  shift after second and higher training loop. Another argument against the remnant field is the effect of starting temperature from where the sample is cooled: remnant field should not be affected, while for exchange coupling crossing  $T_N$  is one of the requirements. Last argument to be mentioned is the interface origin of exchange shift, as shown in the previous section - the exchange coupling can be destroyed by temperature induced changes on the interface, which could not be explained by any persisting field in the magnetic coils.

Other possible origin of exchange bias and exchange broadening could be spin-glass phase on the CuMnAs/Fe interface. It is, however, known that spin glass system exhibits only poor reproducibility when a field cooling experiment is repeated. This is because of its multiple stable spin arrangements and a random character of settling to these minima (as was described in the introduction). Moreover training effect in spin glass/FM coupled system has usually very strong effect and does not settle to a stable value after first training loop. All this is in contrast with what was observed in CuMnAs/Fe interface.

## 4.5 Summary of CuMnAs Characterization

In this chapter a new material was described combining antiferromagnetic and semimetallic-semiconductor properties. The epitaxially grown stoichiometric CuMnAs was shown to have zero net magnetic moment, and when prepared with Fe, to exhibit exchange coupling effect. This is not only a proof of AFM ordered spins in CuMnAs but also it serves as a first demonstration of a functionality of the material. Exchange coupling was a first way of manipulating AFM moments discussed in the previous chapter. Although the thickness of CuMnAs studied in this chapter is too high, the proof of exchange coupling with a FM is an important first step towards experiments similar to those performed in polycrystalline IrMn/NiFe in Chap. 3.

**Future prospects of AFM Semiconductors** Beside the exchange coupling two other ways to manipulate AFM moments were studied in Chap. 3: cooling in magnetic field through  $T_N$  and current induced torques. Recently, the two methods have been demonstrated also in other AFM materials (including semiconductors).

One of the discussed techniques of AFM moments manipulation in IrMn was cooling in magnetic field through the  $T_N$  which sets the orientation of AFM moments. This was already showed in another metallic AFM material - FeRh [8] and very recently also in an antiferromagnetic semiconductor MnTe [22].

The last discussed way of AFM moment manipulation in the previous chapter was by the current induced torques, which was also recently observed in CuMnAs [110]. Although the mechanism behind these experiments is different than in case of IrMn, the potential of AFM spins manipulation was shown and seems to open a new route to possible application of AFM spintronics.

# Conclusion

The motivation for this thesis was to contribute to the emerging field of antiferromagnetic spintronic research. In the two presented experimental chapters we have focused on two problems that are actively studied: manipulation of the antiferromagnetically coupled moments in a well known antiferromagnetic material and development of new AFM materials suitable for AFM spintronics. The problems studied in this thesis may serve as a proof of principle of several important concepts which can be employed in future work towards a device based on AFM materials.

In Chapter 3 we investigated ways how to manipulate antiferromagnetic moments. Three different methods were presented and experimentally studied on nanostructures comprising a thin film of metallic AFM, in our case a well known  $\text{Ir}_{0.2}\text{Mn}_{0.8}$ .

The first presented way of manipulation of AFM spins is by the exchange spring effect. This effect relies on the exchange coupling on the FM/AFM interface; when an external magnetic field is applied, the magnetization of the FM layer is manipulated and, under certain conditions, it can manipulate also the AFM moments. We have shown that the exchange spring effect strongly depends on the AFM thickness and the temperature of the measurement. Based on these factors we have identified four different regions in the phase space of temperature and AFM thickness.

The first region exists above blocking temperature of the exchange bias and exchange broadening, where no AFM spins manipulation can be observed. The second region covers the situation typical for a bulk AFM: the anisotropy of AFM is strong and the coupling on the AFM/FM interface results in an additional exchange field that causes increase of exchange bias. The AFM is, however, robust and the AFM moments cannot be manipulated. These two situations typically occur in very thin ( $\sim 1.5$  nm) or very thick (above 10 nm) AFM layers at higher temperatures. In the range of thicknesses between these two limits, which covers the remaining two regions, the AFM moments can be manipulated. Depending on thickness and temperature the AFM moments are either fully rotating with the FM or they can be only partially rotated into a meta-stable state.

The wafers were studied by magnetometry and by TAMR transport experiments and we have demonstrated that the data from these two methods can be correlated [6]. Magnetometry was used to identify the most suitable thickness of IrMn for a TAMR structure to exhibit spin-valve like signal at 300 K. We determined the range of IrMn thicknesses ( $\sim 4$  -6 nm) where the AFM moments can be rotated to meta-stable state at 300 K, and we have demonstrated that TAMR signal is present. Unfortunately, we also discovered that due to the thermally induced magnetic noise the IrMn moments can not be stabilized in this orientation; instead, random switching of AFM moments was observed.

The second method of AFM moments manipulation relied on cooling an AFM sample through the Néel temperature in magnetic field. We have shown that in a sample comprising no FM layer AFM moments could be successfully manipulated and TAMR signal was measured. The onset of magnetoresistance was in agreement with the Néel temperature of a thin IrMn as was confirmed by an in-

dependent measurement [7]. By the presented experiment we have demonstrated the concept of AFM memory device containing no FM part.

The third method of AFM moment manipulation was based on spin orbit torques. We have focused on experimental demonstration of current induced torque on thin polycrystalline AFM interfaced with a proper heavy metal with strong spin-orbit coupling, in our case Ta. According to theory prediction [111], spin polarization caused by spin Hall effect in Ta should create a torque on adjacent AFM moments. For sensitive measurement of non-ohmic effects we have employed the second harmonic technique and we systematically analyzed the potential contributions to the signal originating in current induced effective fields and thermal gradients in the sample. We have shown that these contributions can be separated by a symmetry analysis of the measured signal. In samples of Ta/CoFeB and Ta/IrMn/CoFeB we experimentally demonstrated the presence of the spin Seebeck effect and antidamping-like torque on CoFeB. Interestingly, in the sample with IrMn, the antidamping-like torque on CoFeB was suppressed above the Neél temperature of IrMn indicating that IrMn acts as an ordinary heavy metal. Due to the opposite spin Hall angle of Ta and IrMn spin current generated by spin Hall effect in these two heavy metals is competing and the torque on CoFeB oscillates around zero. However, once the IrMn is antiferromagnetic, the torque on CoFeB is clearly increased. Considering the sign of the effect, spin current from IrMn is dominating and the spin current from Ta is suppressed. This indicates that the spin current from Ta can be absorbed by IrMn moments.

To confirm the ability of AFM moments to absorb current induced torque we have performed similar experiment with a sample comprising no FM layer. The sample was cooled through the Neél temperature and it was shown that the second harmonic signal appears at the Neél temperature and the signal splits depending on the magnetic field orientation. Although the splitting was consistently present in all measured samples, the reproducibility was limited due to the grain and domain structure of IrMn films which did not settle to identical arrangement under the same field cooling. Once the sample was cooled below the critical temperature the second harmonic signal remained unchanged confirming the AFM origin which is expected to be relatively insensitive to an external field below  $T_N$ . By these experiments we have demonstrated another possible way of AFM moments manipulation which does rely neither on an exchange coupled FM layer nor on cooling in an external field [139].

The three presented methods suggest a potential solution to one of the hurdles in AFM spintronics - control of the orientation of AFM moments. The exchange spring and cooling in field already demonstrated its functionality by being used as a manipulation tool in TAMR spin-valve. In the exchange spring based device the presence of a FM layer, however, would limit the potential of AFM spintronics. The cooling in magnetic field is, on the other hand, time and energy consuming and the presented experiment was only important to show the potential of AFM only based device. Moreover the TAMR structure is very sensitive to material thickness and temperature. The current induced torque manipulation would be an elegant way to overcome these troubles, however, more research needs to be done to have better control over the AFM moments orientation and eventual tilting or switching in practical devices.

While in the third chapter we have studied methods potentially interesting for AFM spintronics, in the chapter 4 we have focused on new materials for AFM spintronics, in particular on an AFM semimetal CuMnAs. It was shown that the material can be prepared in either orthorhombic bulk state by chemical synthesis [109] or in tetragonal epitaxial state [24]. In both cases we presented magnetometry data proving the AFM ordering in the sample and lack of net magnetic moments. The stoichiometric epitaxial CuMnAs was also prepared in a bilayer with Fe and it was shown that the two materials are exchange coupled. Although the observed exchange coupling was relatively weak, we performed several control experiments to confirm its origin at AFM/FM interface and to exclude potential artifacts. We also studied thermal stability of the material and the interface, and we have shown that the CuMnAs/Fe interface is destroyed by heating to temperatures above 450 K. These results were also confirmed by temperature dependent X-ray. The results present a new promising material for AFM spintronics and its first simple functionality.

Merging the two problems studied in chapter 3 and 4 is the next important step in the AFM research. Although much thinner CuMnAs would be required to exploit practically the exchange spring effect, the ability of a new AFM material to couple with a FM is an important proof of concept experiment. The other studied methods of AFM moments manipulation should be also applicable not only to metals; very recently first experiments exploiting both cooling in field [22] and current induced torques [110] in antiferromagnetic semiconductors/semimetals appeared. The effects studied in the chapter 3 therefore should not be limited to the  $\text{Ir}_{0.2}\text{Mn}_{0.8}$  only; instead, they could be useful for the whole broad family of AFM materials.

# A. Appendix

## A.1 Measurement Instruments

### A.1.1 SQUID

Quantum Design Superconducting quantum interference device (SQUID) [149] MPMS XL-7 was employed to measure magnetic moment of a sample. SQUID consists of two Josephson junctions including two superconductors coupled by a small insulating layer called 'weak link'. A schematic picture of the circuit is in the left panel in Fig. A.1. Magnetic flux measured by pickup coils generates a persistent current in the ring. The current is distributed equally between two Josephson junctions in absence of a magnetic signal. When magnetic signal appears, flux through the pick-up coil generates a current through a coil in one Josephson junction and a difference in output voltage across the Josephson junctions is measured as an electric signal.

For more sensitive measurement up to  $10^{-7}$  emu reciprocating sample option (RSO) was employed. The schematic principle of RSO measurement is in the right panel in Fig. A.1. This technique is based on a small periodic displacement of a sample inside SQUID at low frequency, the movement of the sample results in AC signal which is detected by the SQUID coils adding the high AC SQUID sensitivity to a DC measurement.

For measurements in SQUID at temperatures above 400 K an oven option can be installed, which enables measurements in the temperature range 310 K - 800 K. The SQUID oven is inserted into the sample chamber, therefore it reduces the dimension of a sample that can be measured. The oven option can be combined with the RSO option for sensitive measurements up to high temperatures.

**Sample mounting for SQUID** Samples are mounted in plastic straws during measurements within the temperature range 5 K - 400 K. Combinations of multiple straws allows for orienting the sample in a desired directions including out-of-plane direction. Samples are mounted in an aluminum foil and connected by a wire to a special metallic sample holder for SQUID measurements at temperatures above 400 K.

### A.1.2 Transport Measurements

Quantum Design Physical Property Measurement System (PPMS) and Oxford Instruments (OI) cryostat furnished with a 3D vector magnet were used to perform the magneto-transport measurements. Both systems are flow He cryostats equipped by superconductive coils capable of magnetic fields of up to 9 T in PPMS and magnetic field rotation of 2 T. Temperature of the system could be regulated by two mechanisms: first, by adjusting a needle valve between the sample space and the liquid He reservoir; second by a heating element with its own PID controller. Temperature in the OI cryostat was monitored simultaneously by an in-build thermometer and a calibrated Cernox resistor attached to the cold

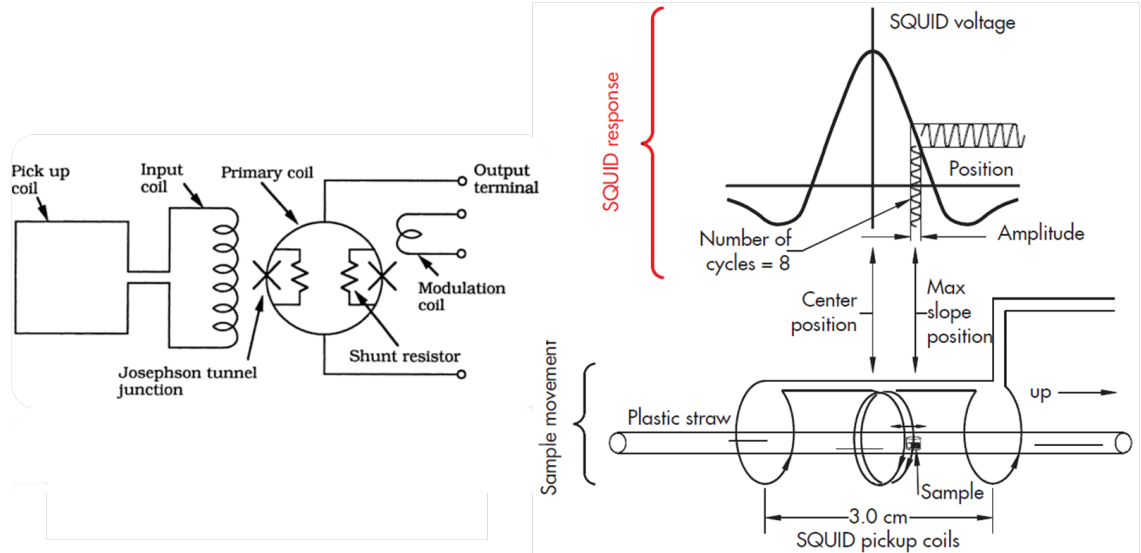


Figure A.1: Principle of SQUID measurement. Left: SQUID consists of two Josephson junction, each with two superconductors coupled by a weak link. Right: A schematic sketch of RSO measurement. After [149, 150]

finger of the sample rod. PPMS system is capable to measure in the range 5 K - 400 K, OI cryostat between 4.2 K - 300 K.

Both cryostats use a vertical loading mechanism; a sample holder with rotator was used for measurements in PPMS in order to apply magnetic field along different directions with respect to the sample. Details about sample mounting into various sample holders for transport measurement are in the Appendix A.3. Quantum Design software was used to control temperature, magnetic field and rotation angle in PPMS. LabVIEW and MATLAB programs controlled the conditions and measurement in the OI cryostat. PPMS is equipped with its own measurement units that were used to measure resistance and temperature. The OI cryostat was accompanied by several additional instruments to apply voltage or current, process and read the signal. Various combinations of following instruments were used: Agilent Parameter Analyzer, Keithley SMU units, Keithley VMU units, HP AC current source, HP function generator, Stanford lock-in amplifiers, voltage pre-amplifier.

## A.2 List of Presented Samples

### A.2.1 Exchange Spring Experiments

The wafers were grown in Hitachi, Japan on silicon wafers. For magnetometry measurements the wafer was divided into 4 parts: one was not annealed, second was annealed at 270°, third at 300° and fourth at 350°. Same wafers were grown for TAMR experiments, only finished with 10 nm Pt serving as the top electrode. TAMR pillars were fabricated in Hitachi, Japan. Three different areas

of pillars were provided:  $1 \times 2 \mu\text{m}^2$ ,  $3 \times 6 \mu\text{m}^2$  and  $5 \times 10 \mu\text{m}^2$ . Many devices from each wafer were measured showing similar properties.

wafer	Ta/Ru/Ta (nm)	NiFe (nm)	IrMn (nm)	MgO (nm)
J010	5/50/5	10	1.5	2.5
J020	5/50/5	10	3	2.5
W02043	5/50/5	10	3	2.5
W02044	5/50/5	10	4	2.5
W02045	5/50/5	10	5	2.5
W02046	5/50/5	10	7.5	2.5
W02047	5/50/5	10	10	2.5
W02048	5/50/5	0	10	2.5

Table A.1: Samples for exchange spring experiments.

### A.2.2 Field Cooling Experiments

The wafers were grown and TAMR pillars were fabricated in LNESS, Como, Italy. Wafers were annealed at  $350^\circ$ . The area of the pillars ranged  $4\text{-}100 \mu\text{m}^2$ . Many devices from each wafer were measured showing similar properties.

wafer	Ta/Ru/Ta (nm)	IrMn (nm)	MgO (nm)
SIMM08	5/50/5	2	2.5
SIMM09	5/50/5	0	2.5

Table A.2: Samples for field cooling experiments.

### A.2.3 Current Induced Torques Experiments

The wafers were grown in Hitachi, Japan on silicon wafers. Wafers were annealed at  $350^\circ$ . After SQUID characterization, Hall bars of dimensions  $2 \times 7 \mu\text{m}^2$  were fabricated at Academy of Science, Prague; the fabrication is described in appendix C.

wafer	Ta (nm)	IrMn (nm)	CoFeB (nm)	MgO (nm)	$\text{AlO}_x$ (nm)
W02927	5	1	0	2.5	10
W02930	2	1	1	2.5	10
W03157	2	0	1	2.5	10

Table A.3: Samples for filed cooling experiments.

### A.2.4 Epitaxial CuMnAs

Samples were prepared at the University of Nottingham, UK.

wafer	Cu flux	caping	% in MnAs
mn717	$4.3 \times 10^{-9}$	0	5.9
mn718	$4.1 \times 10^{-9}$	0	7.1
mn719	$3.7 \times 10^{-9}$	0	17
mn720	$3.0 \times 10^{-9}$	0	21
mn721	$2.6 \times 10^{-9}$	0	32
mn722	$3.3 \times 10^{-9}$	0	24
mn723	$4.9 \times 10^{-9}$	0	0.3
mn673	$7.6 \times 10^{-9}$	0	5.3
mn672	$4.3 \times 10^{-9}$	0	0
mn666	$5.4 \times 10^{-9}$	0	0
mn674	$6.4 \times 10^{-9}$	0	34
mn667	$5.4 \times 10^{-9}$	0	0
mn724	$4.9 \times 10^{-9}$	2 nm Fe	-

Table A.4: Epitaxial CuMnAs samples.

### A.3 Sample Mounting for Transport Measurement

Samples were mounted to three different sample holders as illustrated on the photography in Fig. A.2. Samples were glued by a silver paste and wire-bonded by Aluminum wires on wedge wire-bonder. Special care was taken to avoid electrostatic effects which could cause the sample damage, a grounding wrist band was always used during sample manipulation. For the most sensitive samples (tunnel junctions) even more precautions were taken - all the contact pads were shorted by a wire before the sample was glued. Only after the samples was wire-bonded and connected with to a grounded sample rod, shorting wires were removed.

### A.4 Lithography Processing

The Hall bars for detection of current induced effects were prepared from wafers sputtered according our requirements in Hitachi, Japan. The fabrication process included several steps that are listed in the following.

- **Contacts paths.** After cleaning by acetone in ultrasound bath, PMMA resist was spinned on the bare wafer. By electron beam lithography the contact paths and aligning marks were defined. PMMA was developed by MBIK (in 1:3 solution with IPA) and potential small residual layer of the resist were removed in an oxygen plasma. The oxide layers ( $\text{MgO}$ ,  $\text{AlO}_x$ ) were removed by maD331 optical developed and HCl (1:30 solution with water). Directly after oxide removal, sample was place into evaporator. 150-300 nm of Aluminum was evaporated at working pressure  $\sim 10^{-6}$  Torr. Lift off in an acetone bath was made without use of ultrasound.
- **Hall bar.** Hall bars were defined in HSQ negative resist by electron beam lithography. After exposition the resist was 5 minutes annealed at 300 K

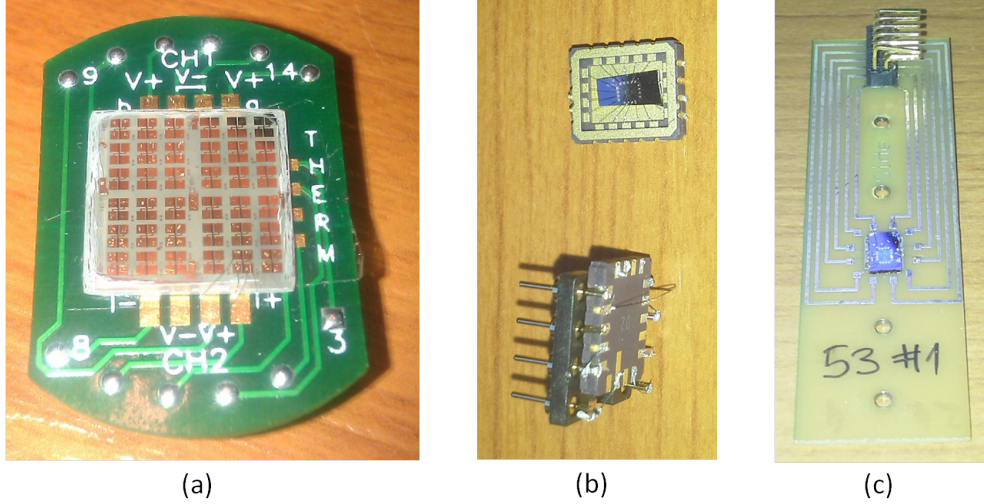


Figure A.2: Sample mounting for transport measurements. (a) Sample holder for PPMS with an array of samples for TAMR junctions. The sample holder is mounted to a sample rod that allows to rotate the sample  $180^\circ$  around one axis. (b) Sample holder used for OI cryostat for type I sample rod with 8 contacts. Thermal contacts is provided by pins connecting the chip carrier and the socket. (c) PCB sample holder for IO cryostat for type II sample rod. On both side of cold finger one PCB with 12 contacts can be mounted, therefore 24 contact is available.

before developing by TMAH. Metallic layers were removed everywhere except of the Hall bar and contacts by Argon plasma etching for 7-10 minutes when Aluminum and HSQ resist served as a mask.

- **Contact pads.** In the last step contact pads were defined in PPMA by electron lithography followed by 5 nm Chrom and 70 nm Gold deposition.

## A.5 Expected Contribution to Second Harmonic Signal

In this section we will describe our analysis of the potential contributions to the second harmonic signal when magnetic field is rotated in the three planes. For this purpose we will introduce more suitable angles valid for arbitrary field directions as shown in Fig. A.3.

We consider following angular dependency of magnetotransport effects: ncAMR is determined by the angle between the magnetization and current and has maximum/minimum when magnetization is along the current direction; cAMR depends on the angle of magnetization from the z-direction and it has a maximum for the out-of-plane magnetization direction. AHE is maximal when magnetization points out-of-plane of the sample and minimal when magnetization rotates  $180^\circ$ . tAMR has symmetry of AMR with maximum/minimum at  $-45^\circ/ +45^\circ$ . When magnetization rotates in-plane of the sample ncAMR and tAMR contributes to the measured signal. When magnetization rotates in x-z plane,  $R_{xy}$  signal is dominated by AHE and the  $R_{xx}$  signal contains contribution from both

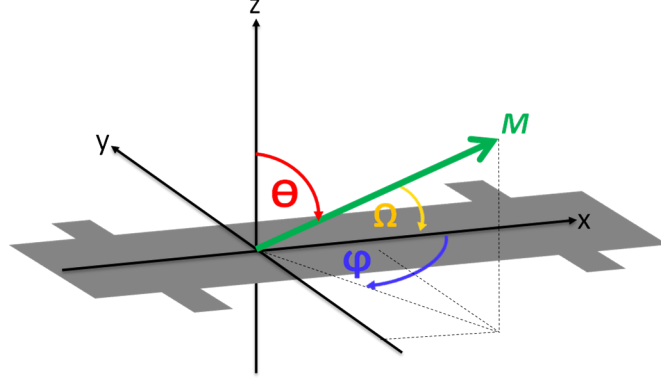


Figure A.3: Definition of angles for general evaluation of terms contributing to second harmonics.  $\mathbf{M}$  is magnetization,  $\theta$  and  $\phi$  are the spherical coordinates of the magnetization and the  $\Omega$  is angle between magnetization and current direction ( $\mathbf{x}$ ).

cAMR and ncAMR, which in our particular case nearly cancel each other. When magnetization rotates in y-z plane,  $R_{xy}$  is dominated by AHE and  $R_{xx}$  contains only cAMR contribution. Formally these effects can be summarized as

$$R_{\text{AHE}} = r_{\text{AHE}} \cos \theta \quad (\text{A.1})$$

$$R_{\text{tAMR}} = r_{\text{ncAMR}} |\sin \theta| \sin(2\phi) \quad (\text{A.2})$$

$$R_{\text{ncAMR}} = r_{\text{ncAMR}} \cos(2\Omega) \quad (\text{A.3})$$

$$R_{\text{cAMR}} = r_{\text{cAMR}} \sin^2 \theta, \quad (\text{A.4})$$

where  $\theta$ ,  $\phi$ ,  $\omega$  are the angles of the magnetization as defined in Fig. A.3. Prefactors  $r_{\text{AHE}}$ ,  $r_{\text{nc}}$ ,  $r_{\text{c}}$  correspond to magnitudes of AHE, ncAMR and cAMR.

The magnetization follows total magnetic field that is given by sum of external magnetic field  $H_0$  and current induced effective field  $H_{\text{eff}}$ . The contribution to  $H_{\text{eff}}$  are of two origins. First is the Rashba effective field  $H_{\text{RA}}$  which is independent on the magnetization direction and in our geometry acts in the  $\mathbf{y}$  direction because  $H_{\text{RA}} \sim \mathbf{j} \times \mathbf{z}$ . The second effective field is originating in anti-damping like torque (AD) and the corresponding effective field  $H_{\text{AD}}$  depends on the magnetization direction as  $H_{\text{AD}} \sim \mathbf{M} \times \mathbf{j} \times \mathbf{z} = \mathbf{M} \times \mathbf{y}$ . Both the  $H_{\text{RA}}$  and  $H_{\text{AD}}$  are current density dependent.

Therefore the vector  $H_{\text{eff}}$  is

$$\mathbf{H}_{\text{ef}} = \begin{pmatrix} -M_z \cdot H_{\text{AD}} \cdot j \\ H_{\text{RA}} \cdot j \\ M_x \cdot H_{\text{AD}} \cdot j \end{pmatrix} = \begin{pmatrix} -\cos(\theta) \cdot H_{\text{AD}} \cdot j \\ H_{\text{RA}} \cdot j \\ \sin(\theta) \cos(\phi) \cdot H_{\text{AD}} \cdot j \end{pmatrix} \quad (\text{A.5})$$

Magnetization direction is given by a vector  $\mathbf{m}$

$$\mathbf{m} = \begin{pmatrix} H_0 \sin \theta_H \cos \phi_H - H_{\text{AD}} j \cos \theta_H \\ H_0 \sin \theta_H \sin \phi_H + H_{\text{RA}} j \\ H_0 \cos \theta_H + H_{\text{AD}} j \sin \theta_H \cos \phi_H \end{pmatrix} \quad (\text{A.6})$$

where  $H_0$  is the amplitude of applied field and  $\theta_H$  and  $\phi_H$  are angles of the external magnetic field.

The second harmonics signal detects a small variations of the resistance caused by the AC current, therefore it is proportional to  $dR/dj$ , which, following Eq.A.1-A.4, is given by

$$\frac{dR_{\text{AHE}}}{dj} = -r_{\text{AHE}} \sin \theta \frac{d\theta}{dj} \quad (\text{A.7})$$

$$\frac{dR_{\text{tAMR}}}{dj} = r_{\text{nc}} \left\{ \cos \theta \operatorname{sgn}(\sin \theta) \sin(2\phi) \frac{d\theta}{dj} + 2 |\sin \theta| \cos(2\phi) \frac{d\phi}{dj} \right\} \quad (\text{A.8})$$

$$\frac{dR_{\text{ncAMR}}}{dj} = -2r_{\text{nc}} \sin(2\Omega) \frac{d\Omega}{dj} \quad (\text{A.9})$$

$$\frac{dR_{\text{cAMR}}}{dj} = 2r_{\text{c}} \sin \theta \cos \theta \frac{d\theta}{dj}. \quad (\text{A.10})$$

The angles  $\phi$  and  $\theta$  can be expressed in Cartesian coordinates as

$$\theta = \arccos\left(\frac{m_z}{\sqrt{m_x^2 + m_y^2 + m_z^2}}\right) \quad (\text{A.11})$$

$$\phi = \arctan\left(\frac{m_y}{m_x}\right), \quad (\text{A.12})$$

the current induced fields can be normalized as  $h_{AD} = H_{AD}/H_0$ ,  $h_{RA} = H_{RA}/H_0$ .

The current induced change of the magnetization angle in our system is very small (cannot be detected by the first harmonics) and only can be measured in the second harmonic signal. This means that in the following we will assume  $\theta_H \sim \theta$  and  $\phi_H \sim \phi$ . After considering  $h_{AD} \ll 1$  and  $h_{RA} \ll 1$ , we obtain

$$\frac{d\theta}{dj} = -h_{AD} \cos(\phi) \operatorname{sgn}(\sin(\theta)) + h_{RA} \cos(\theta) \sin(\phi) \quad (\text{A.13})$$

$$\frac{d\phi}{dj} = \frac{h_{RA} \cos(\phi) + h_{AD} \cos(\theta) \sin(\phi)}{\sin(\phi)} \quad (\text{A.14})$$

$$\frac{d\Omega}{dj} = \frac{h_{AD} \cos(\theta) + h_{RA} \sin(\phi) \cos(\phi) \sin^2(\theta)}{\sqrt{1 - \sin^2(\theta) \cos^2(\phi)}} \quad (\text{A.15})$$

$$(\text{A.16})$$

When we insert these equations into the Eq. A.7-D.10 we obtain the following general expressions for the contributions to the second harmonic signal

$$\frac{dR_{\text{AHE}}}{dj} = -r_{\text{AHE}} (h_{AD} \sin \theta \cos \phi - h_{RA} \cos \theta \sin \phi) \quad (\text{A.17})$$

$$\begin{aligned} \frac{dR_{\text{tAMR}}}{dj} &= r_{\text{ncAMR}} (-h_{AD} \cos \theta \cos \phi \sin(2\phi) + h_{RA} \sin(2\phi) \sin \phi \cos^2(\phi) \\ &\quad + 2 \cos(2\phi) \operatorname{sgn}(\sin \theta) (h_{RA} \cos \phi + h_{AD} \cos \theta \sin \phi)) \end{aligned} \quad (\text{A.18})$$

$$\frac{dR_{\text{ncAMR}}}{dj} = -2r_{\text{ncAMR}} \sin(2\Omega) \frac{h_{AD} \cos \theta + h_{RA} \sin \phi \cos \phi \sin^2 \theta}{\sqrt{1 - \sin^2 \theta \cos^2 \theta}} \quad (\text{A.19})$$

$$\frac{dR_{\text{cAMR}}}{dj} = r_{\text{cAMR}} (-h_{AD} \cos \phi + h_{RA} \cos \theta \sin \phi) \quad (\text{A.20})$$

Rotation plane	angle	$\phi$	$\theta$	$\Omega$
XY	$\alpha$	$\alpha \equiv \phi$	90	$\phi$
XZ	$\beta$	0	$\beta \equiv \theta$	90- $\theta$
YZ	$\gamma$	90	$\gamma \equiv \theta$	90

Table A.5: Angles for particular planes of rotation.

The transverse ( $R_{xy}$ ) and longitudinal ( $R_{xx}$ ) signals were measured for field rotations in three planes. The in-plane rotation of magnetic field ( $xy \equiv \alpha$ ), the out-of-plane to along the bar rotation ( $xz \equiv \beta$ ) and the out-of plane to perpendicular to the bar ( $yz \equiv \gamma$ ). For the particular rotation the general expressions A.17-A.20 can be simplified by considering that some angles are constant, as summarized in Tab. A.5.

Apart of the current induced torques, current induced heating is also reflected in the second harmonic signal. In principle we have to consider two thermal gradients, first in z direction  $\Delta T_{oop}$  (caused by heat transfer from the metallic layers), second in x direction  $\Delta T_{ip}$  (caused by geometry of the device).  $\Delta T_{oop}$  can contribute to the magnetization dependence of the second-harmonic  $R_{xy}$  and  $R_{xx}$  signals without having induced any tilt of the magnetization out of the equilibrium direction. This can be due to the Anomalous Nernst effect (ANE) or the spin Seebeck effect (SSE). Both effects have the same symmetry with the maximum contribution when the magnetization is in-plane.  $\Delta T_{ip}$  can contribute to the second-harmonic  $R_{xy}$  signal via the ANE. The maximum contribution in this case is for the out-of-plane magnetization.

Apart of current induced field, Oersted field generated by the current can be present. The Oersted field would have the same symmetry as Rashba field and therefore in the following tables Rashba field and Oersted field are included under common name  $H_F$ .

By taking all above into account we can summarize the expected signal in second harmonics into Tab. A.6 and Tab. A.7.

$R_{xy}^{2\omega}$	$\alpha$	$\beta$	$\gamma$
$R_{AHE}$	$r_{AHE} H_{AD} \cos \alpha$	$\bar{r}_{AHE} H_{AD} \sin \beta$	$-\bar{r}_{AHE} H_F \sin \gamma \cos \gamma$
$R_{tAMR}$	$r_{ncAMR} 2H_F \cos(2\alpha) \cos \alpha$	$\bar{r}_{ncAMR} 2H_F \text{sgn}(\sin \beta)$	$-\bar{r}_{ncAMR} 2H_{AD} \text{sgn}(\sin \gamma) \cos \gamma$
thermal	$r_{SSE} \Delta T_{oop} \cos \alpha$	$r_{SSE} \Delta T_{oop} \sin \beta$ $+ r_{ANE} \Delta T_{ip} \cos \beta$	$r_{ANE} \Delta T_{ip} \cos \gamma$

Table A.6: Contributions to the second harmonic signal in  $R_{xy}$  resulting from the various effects discussed in the text.

$R_{xx}^{2\omega}$	$\alpha$	$\beta$	$\gamma$
$R_{ncAMR}$	$-r_{ncAMR} 2H_F \sin(2\alpha) \cos \alpha$	$-\bar{r}_{ncAMR} 2H_{AD} \sin(2\beta)$	0
$R_{cAMR}$	0	$-\bar{r}_{cAMR} H_{AD} \sin(2\beta)$	$2\bar{r}_{cAMR} H_F \sin(2\gamma) \cos \gamma$
thermal	$r_{SSE} \Delta T_{oop} \sin \alpha$	0	$r_{SSE} \Delta T_{oop} \sin \gamma$

Table A.7: Contributions to the second harmonic signal in  $R_{xx}$ .

These tables summarize the expected contribution to the second harmonics signal including the angular dependency when the magnetization rotates in one

of the three planes. The  $r_i$  and  $\bar{r}_i$  coefficients are calibrated using the AHE and AMR measurements by considering the total magnetic field including applied magnetic field and the anisotropy field. The anisotropy field is not negligible when magnetization rotates to out-of-plane direction, as was show above. The current induced effective fields  $H_{AD}$  and  $H_F$  can be obtained from the measured second-harmonic transport signals by decomposing the data into the individual angle-dependent terms expected from Tab. A.7 and Tab. A.6.

# List of Publications

- [1] H. Reichlova, D. Kriegner, V. Holy, K. Olejnik, V. Novak, M. Yamada, K. Miura, K. Miura, S. Ogawa, H. Takahashi, T. Jungwirth, and J. Wunderlich, “Current induced torques in structures with ultra-thin irmn antiferromagnet.” accepted PRB.
- [2] D. Kriegner, K. Vyborny, K. Olejnik, H. Reichlova, V. Novak, X. Marti, J. Gazquez, V. Saidl, P. Nemeč, V. Volobuyev, G. Springholz, V. Holy, and T. Jungwirth, “Multiple stable anisotropic magnetoresistance memory in antiferromagnetic MnTe.” <http://arxiv.org/abs/1508.04877>.
- [3] R. B. M. Filho, D. A. B. Barbosa, H. Reichlova, X. Marti, A. S. d. Menezes, A. P. Ayala, and C. W. A. Paschoal, “Role of rare-earth ionic radii on the spin-phonon coupling in multiferroic ordered double perovskites,” *Mater. Res. Express*, vol. 2, p. 075201, Jul 2015.
- [4] C.-L. Jia, L. Jin, D. Wang, S.-B. Mi, M. Alexe, D. Hesse, H. Reichlova, X. Marti, L. Bellaiche, and K. W. Urban, “Nanodomains and nanometer-scale disorder in multiferroic bismuth ferrite single crystals,” *Acta Materialia*, vol. 82, pp. 356–368, Jan 2015.
- [5] N. Tesarova, O. T., V. Novak, K. Olejnik, J. Subrt, H. Reichlova, C. T. Ellis, A. Mukherjee, J. Lee, G. M. Sipahi, and et al., “Systematic study of magnetic linear dichroism and birefringence in (ga,mn)as,” *Physical Review B*, vol. 89, Feb 2014.
- [6] R. X. Silva, H. Reichlova, X. Marti, D. A. B. Barbosa, M. W. Lufaso, B. S. Araujo, A. P. Ayala, and C. W. A. Paschoal, “Spin-phonon coupling in  $\text{gd}(\text{co}_{1/2}\text{mn}_{1/2})\text{o}_3$  perovskite,” *Journal of Applied Physics*, vol. 114, no. 19, p. 194102, 2013.
- [7] P. Wadley, V. Novak, R. Champion, C. Rinaldi, X. Marti, H. Reichlova, J. Zelezny, J. Gazquez, M. Roldan, M. Varela, and et al., “Tetragonal phase of epitaxial room-temperature antiferromagnet cumnas,” *Nature Communications*, vol. 4, Aug 2013.
- [8] D. Petti, E. Albisetti, H. Reichlova, J. Gazquez, M. Varela, M. Molina-Ruiz, A. F. Lopeandia, K. Olejnik, V. Novak, I. Fina, and et al., “Storing magnetic information in irmn/mgo/ta tunnel junctions via field-cooling,” *Appl. Phys. Lett.*, vol. 102, no. 19, p. 192404, 2013.
- [9] P. Nemeč, V. Novak, N. Tesarova, E. Rozkotova, H. Reichlova, D. Butkovicova, F. Trojanek, K. Olejnik, P. Maly, R. Champion, and et al., “The essential role of carefully optimized synthesis for elucidating intrinsic material properties of (ga,mn)as,” *Nature Communications*, vol. 4, p. 1422, Jan 2013.
- [10] F. Maca, J. Masek, O. Stelmakhovych, X. Marti, H. Reichlova, K. Uhlirova, P. Beran, P. Wadley, V. Novak, and T. Jungwirth, “Room-temperature antiferromagnetism in cumnas,” *Journal of Magnetism and Magnetic Materials*, vol. 324, pp. 1606–1612, Apr 2012.

- [11] N. Tesarova, P. Nemeč, E. Rozkotova, J. Subrt, H. Reichlova, D. Butkovicova, F. Trojanek, P. Maly, V. Novak, and T. Jungwirth, “Direct measurement of the three-dimensional magnetization vector trajectory in garnets by a magneto-optical pump-and-probe method,” *Applied Physics Letters*, vol. 100, no. 10, p. 102403, 2012.
- [12] N. Tesarova, E. Rozkotova, H. Reichlova, P. Maly, V. Novak, M. Cukr, T. Jungwirth, and P. Nemeč, “Influence of magnetic anisotropy on laser-induced precession of magnetization in ferromagnetic semiconductor (garnet)as,” *Journal of Nanoscience and Nanotechnology*, vol. 12, pp. 7477–7481, Sep 2012.
- [13] X. Marti, B. G. Park, J. Wunderlich, H. Reichlova, Y. Kurosaki, M. Yamada, H. Yamamoto, A. Nishide, J. Hayakawa, H. Takahashi, and et al., “Electrical measurement of antiferromagnetic moments in exchange-coupled irmn / nife stacks,” *Physical Review Letters*, vol. 108, Jan 2012.

# Bibliography

- [1] L. Neel, “Magnetism and the local molecular field,” in *Nobel Lecture*, 1970.
- [2] D. Jiles, *Magnetism and Magnetic Materials*.
- [3] C. Binek, *Ising-type Antiferromagnets: Model Systems in Statistical Physics*. Springer, 2003.
- [4] A. B. Shick, S. Khmelevskiy, O. N. Mryasov, J. Wunderlich, and T. Jungwirth, “Spin-orbit coupling induced anisotropy effects in bimetallic antiferromagnets: A route towards antiferromagnetic spintronics,” *Phys. Rev. B*, vol. 81, Jun 2010.
- [5] B. G. Park, J. Wunderlich, X. Holyi, V. Holy, V., Y. Kurosaki, M. Yamada, H. Yamamoto, A. Nishide, J. Hayakawa, H. Takahashi, and et al., “A spin-valve-like magnetoresistance of an antiferromagnet-based tunnel junction,” *Nature Materials*, vol. 10, pp. 347–351, Mar 2011.
- [6] X. Marti, B. G. Park, J. Wunderlich, H. Reichlova, Y. Kurosaki, M. Yamada, H. Yamamoto, A. Nishide, J. Hayakawa, H. Takahashi, and et al., “Electrical Measurement of Antiferromagnetic Moments in Exchange-Coupled IrMn / NiFe Stacks,” *Physical Review Letters*, vol. 108, Jan 2012.
- [7] D. Petti, E. Albisetti, H. Reichlova, J. Gazquez, M. Varela, M. Molina-Ruiz, A. F. Lopeandia, K. Olejnik, V. Novak, I. Fina, and et al., “Storing magnetic information in IrMn/MgO/Ta tunnel junctions via field-cooling,” *Appl. Phys. Lett.*, vol. 102, no. 19, p. 192404, 2013.
- [8] X. Marti, I. Fina, C. Frontera, J. Liu, P. Wadley, Q. He, R. J. Paull, J. D. Clarkson, J. Kudrnovsky, I. Turek, and et al., “Room-temperature antiferromagnetic memory resistor,” *Nature Materials*, vol. 13, pp. 367–374, Jan 2014.
- [9] N. W. Ashcroft and N. D. Mermin, *Solid State Physics*.
- [10] S. Blundell, *Magnetism in Condensed Matter*. Oxford University Press, 2001.
- [11] P. Langevin, “Magnetisme et theorie des electrons,” *Annales de chimie et de physique*, 1905.
- [12] P. Weiss, “L hypothese du champ moleculaire et la propriete ferromagnetique,” *J. Phys. Theor. Appl.*, vol. 6, no. 1, pp. 661–690, 1907.
- [13] J. Kubler, A. R. William, and C. B. Sommers, “Formation and coupling of magnetic moments in Heusler alloys,” *Physical Review B*, vol. 28, pp. 1745–1755, Aug 1983.
- [14] F. Casper, T. Graf, S. Chadov, B. Balke, and C. Felser, “Half-Heusler compounds: novel materials for energy and spintronic applications,” *Semicond. Sci. Technol.*, vol. 27, p. 063001, Apr 2012.

- [15] L. Landau, “Possible explanation of the dependence on the field of the susceptibility at low temperatures,” *Phys. Z. Sowjetunion*, no. 4, p. 675, 1933.
- [16] S. Simon, *The Oxford Solid State Basics*. Oxford University Press, 2013.
- [17] A. B. Lidiard, “Antiferromagnetism,” *Reports on Progress in Physics*, vol. 17, pp. 201–244, Jan 1954.
- [18] J. Van Vleck, “Recent developments in the theory of antiferromagnetism,” *J. Phys. Radium*, vol. 12, no. 3, pp. 262–274, 1951.
- [19] C. G. Shull and J. S. Smart, “Detection of Antiferromagnetism by Neutron Diffraction,” *Phys. Rev.*, vol. 76, pp. 1256–1257, Oct 1949.
- [20] M. Molina-Ruiz, A. F. Lopeandia, F. Pi, D. Givord, O. Bourgeois, and J. Rodriguez-Viejo, “Evidence of finite-size effect on the Neel temperature in ultrathin layers of CoO nanograins,” *Phys. Rev. B*, vol. 83, Apr 2011.
- [21] K. Rajagopal, *Textbook Of Engineering Physics*. PHI Learning Private Limited, 2009.
- [22] D. Kriegner, K. Vyborny, K. Olejnik, H. Reichlova, V. Novak, X. Marti, J. Gazquez, V. Saidl, P. Nemeč, V. Volobuyev, G. Springholz, V. Holy, and T. Jungwirth, “Multiple stable anisotropic magnetoresistance memory in antiferromagnetic MnTe.” <http://arxiv.org/abs/1508.04877>.
- [23] T. Yamaoka, “Antiferromagnetism in gamma-Phase Mn-Ir Alloys,” *J. Phys. Soc. Jpn.*, vol. 36, pp. 445–450, Feb 1974.
- [24] P. Wadley, V. Novak, R. Champion, C. Rinaldi, X. Marti, H. Reichlova, J. Zelezny, J. Gazquez, M. Roldan, M. Varela, and et al., “Tetragonal phase of epitaxial room-temperature antiferromagnet CuMnAs,” *Nature Communications*, vol. 4, Aug 2013.
- [25] U. of the Basque Country, “Bilbao Crystallographic Server.” <http://www.cryst.ehu.es/>.
- [26] A. Kohn, A. Kovacs, R. Fan, G. J. McIntyre, R. C. C. Ward, and J. P. Goff, “The antiferromagnetic structures of IrMn<sub>3</sub> and their influence on exchange-bias,” *Sci. Rep.*, vol. 3, Aug 2013.
- [27] L. Smejkal, “in preparation.”
- [28] O. Gomonay, “Berry-phase effects and electronic dynamics in a noncollinear antiferromagnetic texture,” *Physical Review B*, vol. 91, Apr 2015.
- [29] T. Castellani and A. Cavagna, “Spin-glass theory for pedestrians,” *Journal of Statistical Mechanics: Theory and Experiment*, vol. 2005, p. P05012, May 2005.
- [30] K. Binder and A. P. Young, “Spin glasses: Experimental facts, theoretical concepts, and open questions,” *Rev. Mod. Phys.*, vol. 58, pp. 801–976, Oct 1986.

- [31] M. Gruyters, “Spin-Glass-Like Behavior in CoO Nanoparticles and the Origin of Exchange Bias in Layered CoO / Ferromagnet Structures,” *Physical Review Letters*, vol. 95, Aug 2005.
- [32] M. Ali, P. Adie, C. H. Marrows, D. Greig, B. J. Hickey, and R. L. Stamps, “Exchange bias using a spin glass,” *Nature Materials*, vol. 6, pp. 70–75, Dec 2006.
- [33] W. H. Meiklejohn and C. P. Bean, “New Magnetic Anisotropy,” *Phys. Rev.*, vol. 102, pp. 1413–1414, Jun 1956.
- [34] R. Jungblut, R. Coehoorn, M. T. Johnson, J. aan de Stegge, and A. Reinders, “Orientational dependence of the exchange biasing in molecular-beam-epitaxy-grown Ni<sub>80</sub>Fe<sub>20</sub>/Fe<sub>50</sub>Mn<sub>50</sub> bilayers (invited),” *Journal of Applied Physics*, vol. 75, no. 10, p. 6659, 1994.
- [35] J. Nogues and I. K. Schuller, “Exchange bias,” *Journal of Magnetism and Magnetic Materials*, vol. 192, pp. 203–232, Feb 1999.
- [36] T. J. Moran, J. M. Gallego, and I. K. Schuller, “Increased exchange anisotropy due to disorder at permalloy/CoO interfaces,” *Journal of Applied Physics*, vol. 78, no. 3, p. 1887, 1995.
- [37] W. Kuch, L. I. Chelaru, F. Offi, J. Wang, M. Kotsugi, and J. Kirschner, “Tuning the magnetic coupling across ultrathin antiferromagnetic films by controlling atomic-scale roughness,” *Nature Materials*, vol. 5, pp. 128–133, Jan 2006.
- [38] J. Nogues, D. Lederman, T. Moran, and I. Schuller, “Positive Exchange Bias in FeF<sub>2</sub>-Fe Bilayers,” *Physical Review Letters*, vol. 76, pp. 4624–4627, Jun 1996.
- [39] F. Radu, *Fundamental Aspects of Exchange Bias Effect in AF/F Bilayers and Multilayers*. PhD thesis, Faculty of Physics and Mathematics, Bochum Ruhr-University, 2005.
- [40] M. Kiwi, “Exchange bias theory,” *Journal of Magnetism and Magnetic Materials*, vol. 234, pp. 584–595, Sep 2001.
- [41] W. Meiklejohn and C. Bean, “New Magnetic Anisotropy,” *Phys. Rev.*, vol. 105, pp. 904–913, Feb 1957.
- [42] L. Neel, “Etude Theorique - du Couplage Ferro-Antiferromagnetique dans les couches minces,” *ANNALES DE PHYSIQUE*, vol. 2, no. 2, p. 61, 1967.
- [43] D. Mauri, H. C. Siegmann, P. S. Bagus, and E. Kay, “Simple model for thin ferromagnetic films exchange coupled to an antiferromagnetic substrate,” *Journal of Applied Physics*, vol. 62, no. 7, p. 3047, 1987.
- [44] A. Scholl, M. Liberati, E. Arenholz, H. Ohldag, and J. Stoehr, “Creation of an Antiferromagnetic Exchange Spring,” *Physical Review Letters*, vol. 92, Jun 2004.

- [45] A. P. Malozemoff, “Random-field model of exchange anisotropy at rough ferromagnetic-antiferromagnetic interfaces,” *Phys. Rev. B*, vol. 35, pp. 3679–3682, Mar 1987.
- [46] P. Miltenyi, M. Gierlings, J. Keller, B. Beschoten, G. Guntherodt, U. Nowak, and K. D. Usadel, “Diluted Antiferromagnets in Exchange Bias: Proof of the Domain State Model,” *Physical Review Letters*, vol. 84, pp. 4224–4227, May 2000.
- [47] C. Sanchez-Hanke and C.-C. Kao, “An element-sensitive hysteresis loop study of an exchange-biased Co/NiO bilayer,” *Journal of Magnetism and Magnetic Materials*, vol. 226-230, pp. 1803–1805, May 2001.
- [48] H. Ohldag, A. Scholl, F. Nolting, E. Arenholz, S. Maat, A. T. Young, M. Carey, and J. Stoehr, J.hr, “Correlation between Exchange Bias and Pinned Interfacial Spins,” *Physical Review Letters*, vol. 91, Jul 2003.
- [49] F. Radu and H. Zabel, *Magnetic Heterostructures*. Springer Berlin Heidelberg, 2008.
- [50] F. Radu, A. Westphalen, K. Theis-Broehl, and H. Zabel, “Quantitative description of the azimuthal dependence of the exchange bias effect,” *J. Phys.: Condens. Matter*, vol. 18, pp. L29–L36, Dec 2006.
- [51] J. Nogues, S. Stepanow, A. Bollero, J. Sort, B. Dieny, F. Nolting, and P. Gambardella, “Simultaneous in-plane and out-of-plane exchange bias using a single antiferromagnetic layer resolved by x-ray magnetic circular dichroism,” *Appl. Phys. Lett.*, vol. 95, no. 15, p. 152515, 2009.
- [52] H. Fulara, S. Chaudhary, S. C. Kashyap, and D. K. Pandya, “Positive exchange bias in as-deposited ion-beam sputtered IrMn-CoFeB system,” *Journal of Applied Physics*, vol. 110, no. 9, p. 093916, 2011.
- [53] M. Dyakonov and V. Perel, “Current-induced spin orientation of electrons in semiconductors,” *Physics Letters A*, vol. 35, pp. 459–460, Jul 1971.
- [54] J. Wunderlich, B. Kaestner, J. Sinova, and T. Jungwirth, “Experimental Observation of the Spin-Hall Effect in a Two-Dimensional Spin-Orbit Coupled Semiconductor System,” *Physical Review Letters*, vol. 94, Feb 2005.
- [55] Y. K. Kato, R. C. Myers, A. C. Gossard, and D. D. Awschalom, “Observation of the Spin Hall Effect in Semiconductors,” *Science*, vol. 306, pp. 1910–1913, Dec 2004.
- [56] S. O. Valenzuela and M. Tinkham, “Direct electronic measurement of the spin Hall effect,” *Nature*, vol. 442, pp. 176–179, Jul 2006.
- [57] J. E. Hirsch, “Spin Hall Effect,” *Physical Review Letters*, vol. 83, pp. 1834–1837, Aug 1999.
- [58] S. Murakami, N. Nagaosa, and S. C. Zhang, “Dissipationless Quantum Spin Current at Room Temperature,” *Science*, vol. 301, pp. 1348–1351, Sep 2003.

- [59] J. Sinova, D. Culcer, Q. Niu, N. A. Sinitsyn, T. Jungwirth, and A. H. MacDonald, “Universal Intrinsic Spin Hall Effect,” *Physical Review Letters*, vol. 92, Mar 2004.
- [60] S. D. Ganichev, E. L. Ivchenko, V. V. Belakov, S. A. Tarasenko, M. Sollinger, D. Weiss, W. Wegscheider, and W. Prettl, “Spin-galvanic effect,” *Nature*, vol. 417, pp. 153–156, May 2002.
- [61] F. Y. Yang, K. Liu, K. Hong, D. H. Reich, P. Searson, and C. C.L., “Large Magnetoresistance of Electrodeposited Single-Crystal Bismuth Thin Films,” *Science*, vol. 284, pp. 1335–1337, May 1999.
- [62] T. Thio, S. A. Solin, J. W. Bennett, D. R. Hines, M. Kawano, N. Oda, and M. Sano, “Giant magnetoresistance in zero-band-gap  $\text{Hg}_{1-x}\text{Cdx Te}$ ,” *Phys. Rev. B*, vol. 57, pp. 12239–12244, May 1998.
- [63] S. Ishiwata, Y. Shiomi, J. S. Lee, M. S. Bahramy, T. Suzuki, M. Uchida, R. Arita, Y. Taguchi, and Y. Tokura, “Extremely high electron mobility in a phonon-glass semimetal,” *Nature Materials*, vol. 12, pp. 512–517, Apr 2013.
- [64] M. N. Ali, J. Xiong, S. Flynn, J. Tao, Q. D. Gibson, L. M. Schoop, T. Liang, N. Haldolaarachchige, M. Hirschberger, N. P. Ong, and et al., “Large, non-saturating magnetoresistance in  $\text{WTe}_2$ ,” *Nature*, Sep 2014.
- [65] S. A. Solin, T. Thio, D. Hines, and H. J. J., “Enhanced Room-Temperature Geometric Magnetoresistance in Inhomogeneous Narrow-Gap Semiconductors,” *Science*, vol. 289, pp. 1530–1532, Sep 2000.
- [66] A. W. Rushforth, K. Vyborny, C. S. King, K. W. Edmonds, R. P. Campion, C. T. Foxon, J. Wunderlich, A. C. Irvine, P. Vasek, V. Novak, and et al., “Anisotropic Magnetoresistance Components in  $(\text{Ga,Mn})\text{As}$ ,” *Physical Review Letters*, vol. 99, Oct 2007.
- [67] E. De Ranieri, A. W. Rushforth, K. Vyborny, U. Rana, E. Ahmad, R. P. Campion, C. T. Foxon, B. L. Gallagher, A. C. Irvine, J. Wunderlich, and et al., “Lithographically and electrically controlled strain effects on anisotropic magnetoresistance in  $(\text{Ga,Mn})\text{As}$ ,” *New Journal of Physics*, vol. 10, p. 065003, Jun 2008.
- [68] A. Rushforth, K. Vyborny, C. King, K. Edmonds, R. Campion, C. Foxon, J. Wunderlich, A. Irvine, V. Novak, K. Olejnik, and et al., “The origin and control of the sources of AMR in  $(\text{Ga,Mn})\text{As}$  devices,” *Journal of Magnetism and Magnetic Materials*, vol. 321, pp. 1001–1008, Apr 2009.
- [69] M. N. Baibich, J. M. Broto, A. Fert, F. N. Van Dau, F. Petroff, P. Etienne, G. Creuzet, A. Friederich, and J. Chazelas, “Giant Magnetoresistance of  $(001)\text{Fe}/(001)\text{Cr}$  Magnetic Superlattices,” *Physical Review Letters*, vol. 61, pp. 2472–2475, Nov 1988.
- [70] G. Binasch, P. Gruenberg, F. Saurenbach, and W. Zinn, “Enhanced magnetoresistance in layered magnetic structures with antiferromagnetic inter-layer exchange,” *Phys. Rev. B*, vol. 39, pp. 4828–4830, Mar 1989.

- [71] M. Julliere, “Tunneling between ferromagnetic films,” *Physics Letters A*, vol. 54, pp. 225–226, Sep 1975.
- [72] J. S. Moodera, L. R. Kinder, T. M. Wong, and R. Meservey, “Large Magnetoresistance at Room Temperature in Ferromagnetic Thin Film Tunnel Junctions,” *Physical Review Letters*, vol. 74, pp. 3273–3276, Apr 1995.
- [73] S. Ikeda, J. Hayakawa, Y. Ashizawa, Y. M. Lee, K. Miura, H. Hasegawa, M. Tsunoda, F. Matsukura, and H. Ohno, “Tunnel magnetoresistance of 604at 300K by suppression of Ta diffusion in CoFeB/MgO/CoFeB pseudo-spin-valves annealed at high temperature,” *Appl. Phys. Lett.*, vol. 93, no. 8, p. 082508, 2008.
- [74] B. G. Park, J. Wunderlich, D. A. Williams, S. J. Joo, K. Y. Jung, K. H. Shin, K. Olejnik, A. B. Shick, and T. Jungwirth, “Tunneling Anisotropic Magnetoresistance in Multilayer- ( Co / Pt ) / AlO<sub>x</sub> / Pt Structures,” *Physical Review Letters*, vol. 100, Feb 2008.
- [75] C. Gould, C. Ruester, T. Jungwirth, E. Girgis, G. Schott, R. Giraud, K. Brunner, G. Schmidt, and L. Molenkamp, “Tunneling Anisotropic Magnetoresistance: A Spin-Valve-Like Tunnel Magnetoresistance Using a Single Magnetic Layer,” *Phys. Rev. Lett.*, vol. 93, Sep 2004.
- [76] R. A. Duine, P. M. Haney, A. S. Nunez, and A. H. MacDonald, “Inelastic scattering in ferromagnetic and antiferromagnetic spin valves,” *Phys. Rev. B*, vol. 75, Jan 2007.
- [77] A. S. Nunez, R. A. Duine, P. Haney, and A. H. MacDonald, “Theory of spin torques and giant magnetoresistance in antiferromagnetic metals,” *Phys. Rev. B*, vol. 73, Jun 2006.
- [78] M.-A. Leroy, A. M. Bataille, B. Dkhil, F. Porcher, A. Barbier, V. L. R. Jacques, Y. Lu, C. Bellouard, T. Hauet, S. Ravy, and et al., “Tunnel-mediated coupling between antiferromagnetic thin films,” *Phys. Rev. B*, vol. 90, Jul 2014.
- [79] R. Shindou and N. Nagaosa, “Orbital Ferromagnetism and Anomalous Hall Effect in Antiferromagnets on the Distorted fcc Lattice,” *Physical Review Letters*, vol. 87, Aug 2001.
- [80] F. Freimuth, S. Bluegel, and Y. Mokrousov, “Anisotropic Spin Hall Effect from First Principles,” *Physical Review Letters*, vol. 105, Dec 2010.
- [81] H. Chen, Q. Niu, and A. H. MacDonald, “Anomalous Hall Effect Arising from Noncollinear Antiferromagnetism,” *Physical Review Letters*, vol. 112, Jan 2014.
- [82] W. Zhang, M. B. Jungfleisch, W. Jiang, J. E. Pearson, A. Hoffmann, F. Freimuth, and Y. Mokrousov, “Spin Hall Effects in Metallic Antiferromagnets,” *Physical Review Letters*, vol. 113, Nov 2014.

- [83] T. Kikkawa, K. Uchida, S. Daimon, Y. Shiomi, H. Adachi, Z. Qiu, D. Hou, X.-F. Jin, S. Maekawa, and E. Saitoh, “Separation of longitudinal spin Seebeck effect from anomalous Nernst effect: Determination of origin of transverse thermoelectric voltage in metal/insulator junctions,” *Physical Review B*, vol. 88, Dec 2013.
- [84] A. Frauen, A. Kobs, T. Bohnert, A.-K. Michel, G. Winkler, K. Nielsch, and H. P. Oepen, “Magneto-thermoelectric power in Co/Pt layered structures: Interface versus bulk contributions.”
- [85] W. Thomson, “Bakerian Lecture: On the Electro-Dynamic Qualities of Metals,” *Philos. Trans. R. Soc. London*, 1856.
- [86] N. F. Mott, “The Resistance and Thermoelectric Properties of the Transition Metals,” *Proceedings of the Royal Society A: Mathematical, Physical and Engineering Sciences*, vol. 156, pp. 368–382, Aug 1936.
- [87] M. Cutler and N. F. Mott, “Observation of Anderson Localization in an Electron Gas,” *Phys. Rev.*, vol. 181, pp. 1336–1340, May 1969.
- [88] V. D. Ky, “Planar Hall and Nernst Effect in Ferromagnetic Metals,” *phys. stat. sol. (b)*, vol. 22, no. 2, pp. 729–736, 1967.
- [89] A. D. Avery, M. R. Pufall, and B. L. Zink, “Determining the planar Nernst effect from magnetic-field-dependent thermopower and resistance in nickel and permalloy thin films,” *Phys. Rev. B*, vol. 86, Nov 2012.
- [90] A. Dyrda and J. Barna, “Intrinsic contribution to spin Hall and spin Nernst effects in a bilayer graphene,” *J. Phys.: Condens. Matter*, vol. 24, p. 275302, Jun 2012.
- [91] K. Uchida, S. Takahashi, K. Harii, J. Ieda, W. Koshibae, K. Ando, S. Maekawa, and E. Saitoh, “Observation of the spin Seebeck effect,” *Nature*, vol. 455, pp. 778–781, Oct 2008.
- [92] H. Adachi, K.-i. Uchida, E. Saitoh, and S. Maekawa, “Theory of the spin Seebeck effect,” *Reports on Progress in Physics*, vol. 76, p. 036501, Feb 2013.
- [93] C. M. Jaworski, R. C. Myers, E. Johnston-Halperin, and J. P. Heremans, “Giant spin Seebeck effect in a non-magnetic material,” *Nature*, vol. 487, pp. 210–213, Jul 2012.
- [94] K. Uchida, J. Xiao, H. Adachi, J. Ohe, S. Takahashi, J. Ieda, T. Ota, Y. Kajiwara, H. Umezawa, H. Kawai, and et al., “Spin Seebeck insulator,” *Nature Materials*, vol. 9, pp. 894–897, Sep 2010.
- [95] A. Slachter, F. L. Bakker, and B. J. van Wees, “Anomalous Nernst and anisotropic magnetoresistive heating in a lateral spin valve,” *Phys. Rev. B*, vol. 84, Jul 2011.

- [96] J. Wunderlich, B.-G. Park, A. C. Irvine, L. P. Zarbo, E. Rozkotova, P. Nemeč, V. Novak, J. Sinova, and T. Jungwirth, “Spin Hall Effect Transistor,” *Science*, vol. 330, pp. 1801–1804, Dec 2010.
- [97] I. M. Miron, G. Gaudin, S. Auffret, B. Rodmacq, A. Schuhl, S. Pizzini, J. Vogel, and P. Gambardella, “Current-driven spin torque induced by the Rashba effect in a ferromagnetic metal layer,” *Nature Materials*, Jan 2010.
- [98] T. Jungwirth, V. Novak, X. Marti, M. Cukr, F. Maca, A. B. Shick, J. Masek, P. Horodyska, P. Nemeč, V. Holy, and et al., “Demonstration of molecular beam epitaxy and a semiconducting band structure for I-Mn-V compounds,” *Phys. Rev. B*, vol. 83, Jan 2011.
- [99] X. Lou, C. Adelman, S. A. Crooker, E. S. Garlid, J. Zhang, K. S. M. Reddy, S. D. Flexner, C. J. Palmstrom, and P. A. Crowell, “Electrical detection of spin transport in lateral ferromagnetic semiconductor devices,” *Nat Phys*, vol. 3, pp. 197–202, Feb 2007.
- [100] S. Bader and S. Parkin, “Spintronics,” *Annu. Rev. Condens. Matter Phys.*, vol. 1, pp. 71–88, Aug 2010.
- [101] G. Salis, A. Fuhrer, R. R. Schlittler, L. Gross, and S. F. Alvarado, “Temperature dependence of the nonlocal voltage in an Fe/GaAs electrical spin-injection device,” *Phys. Rev. B*, vol. 81, May 2010.
- [102] K. Ando, S. Takahashi, J. Ieda, H. Kurebayashi, T. Trypiniotis, C. H. W. Barnes, S. Maekawa, and E. Saitoh, “Electrically tunable spin injector free from the impedance mismatch problem,” *Nature Materials*, vol. 10, pp. 655–659, Jun 2011.
- [103] K. Olejnik, J. Wunderlich, A. C. Irvine, R. P. Campion, V. P. Amin, J. Sinova, and T. Jungwirth, “Detection of Electrically Modulated Inverse Spin Hall Effect in an Fe / GaAs Microdevice,” *Physical Review Letters*, vol. 109, Aug 2012.
- [104] T. Jungwirth, J. Sinova, J. Masek, J. Kucera, and A. H. MacDonald, “Theory of ferromagnetic (III,Mn)V semiconductors,” *Rev. Mod. Phys.*, vol. 78, pp. 809–864, Aug 2006.
- [105] T. Jungwirth, J. Wunderlich, V. Novak, K. Olejnik, B. L. Gallagher, R. P. Campion, K. W. Edmonds, A. W. Rushforth, A. J. Ferguson, and P. Nemeč, “Spin-dependent phenomena and device concepts explored in (Ga,Mn)As,” *Rev. Mod. Phys.*, vol. 86, pp. 855–896, Jul 2014.
- [106] T. Dietl and H. Ohno, “Dilute ferromagnetic semiconductors: Physics and spintronic structures,” *Rev. Mod. Phys.*, vol. 86, pp. 187–251, Mar 2014.
- [107] S. Lee, J.-H. Chung, X. Liu, J. K. Furdyna, and B. J. Kirby, “Ferromagnetic semiconductor GaMnAs,” *Materials Today*, vol. 12, pp. 14–21, Apr 2009.
- [108] J. Allen, G. Lucovsky, and J. Mikkelsen, “Optical properties and electronic structure of crossroads material MnTe,” *Solid State Communications*, vol. 24, pp. 367–370, Nov 1977.

- [109] F. Maca, J. Masek, O. Stelmakhovych, X. Marti, H. Reichlova, K. Uhlirva, P. Beran, P. Wadley, V. Novak, and T. Jungwirth, “Room-temperature antiferromagnetism in CuMnAs,” *Journal of Magnetism and Magnetic Materials*, vol. 324, pp. 1606–1612, Apr 2012.
- [110] P. Wadley, B. Howells, J. Zelezny, C. Andrews, V. Hills, R. P. Campion, V. Novak, F. Freimuth, Y. Mokrousov, A. W. Rushforth, K. W. Edmonds, B. L. Gallagher, and T. Jungwirth, “Electrical switching of an antiferromagnet.” arXiv:1503.03765.
- [111] J. Zelezny, H. Gao, K. Vyborny, J. Zemen, J. Masek, A. Manchon, J. Wunderlich, J. Sinova, and T. Jungwirth, “Relativistic Neel-Order Fields Induced by Electrical Current in Antiferromagnets,” *Physical Review Letters*, vol. 113, Oct 2014.
- [112] P. Nemeč, E. Rozkotova, N. T. F. Tesarova, N., E. De Ranieri, K. Olejnik, J. Zemen, V. Novak, M. Cukr, P. Maly, and et al., “Experimental observation of the optical spin transfer torque,” *Nat Phys*, vol. 8, pp. 411–415, Apr 2012.
- [113] A. Brataas, A. D. Kent, and H. Ohno, “Current-induced torques in magnetic materials,” *Nature Materials*, vol. 11, pp. 372–381, Apr 2012.
- [114] A. Chernyshov, M. Overby, X. Liu, J. K. Furdyna, Y. Lyanda-Geller, and L. P. Rokhinson, “Evidence for reversible control of magnetization in a ferromagnetic material by means of spin orbit magnetic field,” *Nat Phys*, vol. 5, pp. 656–659, Aug 2009.
- [115] L. Liu, C.-F. Pai, Y. Li, H. W. Tseng, D. C. Ralph, and R. A. Buhrman, “Spin-Torque Switching with the Giant Spin Hall Effect of Tantalum,” *Science*, vol. 336, pp. 555–558, May 2012.
- [116] J. Kim, J. Sinha, M. Hayashi, M. Yamanouchi, S. Fukami, T. Suzuki, S. Mitani, and H. Ohno, “Layer thickness dependence of the current-induced effective field vector in Ta CoFeB MgO,” *Nature Materials*, vol. 12, pp. 240–245, Dec 2012.
- [117] K. M. D. Hals and A. Brataas, “Phenomenology of current-induced spin-orbit torques,” *Phys. Rev. B*, vol. 88, Aug 2013.
- [118] K. Garello, I. M. Miron, C. O. Avci, F. Freimuth, Y. Mokrousov, S. Blugel, S. Auffret, O. Boulle, G. Gaudin, and P. Gambardella, “Symmetry and magnitude of spin orbit torques in ferromagnetic heterostructures,” *Nature Nanotechnology*, vol. 8, pp. 587–593, Jul 2013.
- [119] M. Jamali, K. Narayanapillai, X. Qiu, L. M. Loong, A. Manchon, and H. Yang, “Spin Orbit Torques in Co/Pd Multilayer Nanowires,” *Physical Review Letters*, vol. 111, Dec 2013.
- [120] Y. Fan, P. Upadhyaya, X. Kou, M. Lang, S. Takei, Z. Wang, J. Tang, L. He, L.-T. Chang, M. Montazeri, and et al., “Magnetization switching through giant spin-orbit torque in a magnetically doped topological insulator heterostructure,” *Nature Materials*, vol. 13, pp. 699–704, Apr 2014.

- [121] C. O. Avci, K. Garello, C. Nistor, S. Godey, B. Ballesteros, A. Mugarza, A. Barla, M. Valvidares, E. Pellegrin, A. Ghosh, and et al., “Fieldlike and antidamping spin orbit torques in as-grown and annealed Ta/CoFeB/MgO layers,” *Phys. Rev. B*, vol. 89, Jun 2014.
- [122] M. Hayashi, J. Kim, M. Yamanouchi, and H. Ohno, “Quantitative characterization of the spin-orbit torque using harmonic Hall voltage measurements,” *Phys. Rev. B*, vol. 89, Apr 2014.
- [123] C. O. Avci, K. Garello, M. Gabureac, A. Ghosh, A. Fuhrer, S. F. Alvarado, and P. Gambardella, “Interplay of spin-orbit torque and thermoelectric effects in ferromagnet/normal-metal bilayers,” *Phys. Rev. B*, vol. 90, Dec 2014.
- [124] T. D. Skinner, K. Olejnik, L. K. Cunningham, H. Kurebayashi, R. P. Campion, B. L. Gallagher, T. Jungwirth, and A. J. Ferguson, “Complementary spin-Hall and inverse spin-galvanic effect torques in a ferromagnet/semiconductor bilayer,” *Nature Communications*, vol. 6, p. 6730, Mar 2015.
- [125] N. Tesarova, P. Nemeč, E. Rozkotova, J. Zemen, T. Janda, D. Butkovicova, F. Trojanek, K. Olejnik, V. Novak, P. Maly, and et al., “Experimental observation of the optical spin-orbit torque,” *Nature Photon*, vol. 7, pp. 492–498, Apr 2013.
- [126] V. Tshitoyan, C. Ciccarelli, A. Mihai, M. Ali, A. C. Irvine, T. A. Moore, T. Jungwirth, and A. J. Ferguson, “Electrical manipulation of a ferromagnet by an antiferromagnet.” arXiv:1502.04570.
- [127] Y. A. Bychkov and E. I. Rashba, “Properties of a 2d electron-gas with lifted spectral degeneracy,” *JETP Lett.* 39, 78–81, 1984.
- [128] G. Dresselhaus, “Spin-orbit coupling effects in zinc blende structures,” *Phys. Rev.* 100, 580–586, 1955.
- [129] I. M. Miron, K. Garello, G. Gaudin, P.-J. Zermatten, M. V. Costache, S. Auffret, S. Bandiera, B. Rodmacq, A. Schuhl, and P. Gambardella, “Perpendicular switching of a single ferromagnetic layer induced by in-plane current injection,” *Nature*, vol. 476, p. 189, 2010.
- [130] H. Okamoto, “The Ir-Mn (Iridium-Manganese) system,” *JPE*, vol. 17, pp. 60–62, Jan 1996.
- [131] D. D. Lam, F. Bonell, S. Miwa, Y. Shiota, K. Yakushiji, H. Kubota, T. Nozaki, A. Fukushima, S. Yuasa, and Y. Suzuki, “MgO overlayer thickness dependence of perpendicular magnetic anisotropy in CoFeB thin films,” *Journal of the Korean Physical Society*, vol. 62, pp. 1461–1464, May 2013.
- [132] U. Pietsch, V. Holy, and T. Baumbach, *High-Resolution X-Ray Scattering*. Springer-Verlag New York, 2004.

- [133] G. Vallejo-Fernandez, L. E. Fernandez-Outon, and K. O Grady, “Measurement of the anisotropy constant of antiferromagnets in metallic polycrystalline exchange biased systems,” *Applied Physics Letters*, vol. 91, no. 21, p. 212503, 2007.
- [134] S. Queste, S. Dubourg, O. Acher, J.-C. Soret, K.-U. Barholz, and R. Mattheis, “Microwave permeability study for antiferromagnet thickness dependence on exchange bias field in NiFe/IrMn layers,” *Journal of Magnetism and Magnetic Materials*, vol. 288, pp. 60–65, Mar 2005.
- [135] M. Ali, C. H. Marrows, and B. J. Hickey, “Onset of exchange bias in ultra-thin antiferromagnetic layers,” *Physical Review B*, vol. 67, May 2003.
- [136] Y. Y. Wang, C. Song, B. Cui, G. Y. Wang, F. Zeng, and F. Pan, “Room-Temperature Perpendicular Exchange Coupling and Tunneling Anisotropic Magnetoresistance in an Antiferromagnet-Based Tunnel Junction,” *Physical Review Letters*, vol. 109, Sep 2012.
- [137] T. Jungwirth, X. Marti, P. Wadley, and J. Wunderlich, “Antiferromagnetic spintronics,” <http://arxiv.org/abs/1509.05296>.
- [138] A. H. MacDonald and M. Tsoi, “Antiferromagnetic metal spintronics,” *Philosophical Transactions of the Royal Society A: Mathematical, Physical and Engineering Sciences*, vol. 369, pp. 3098–3114, Jul 2011.
- [139] H. Reichlova, D. Kriegner, V. Holy, K. Olejnik, V. Novak, M. Yamada, K. Miura, K. Miura, S. Ogawa, H. Takahashi, T. Jungwirth, and J. Wunderlich, “Current induced torques in structures with ultra-thin IrMn antiferromagnet.” <http://arxiv.org/abs/1503.03729>.
- [140] H. V. Gomonay, R. V. Kunitsyn, and V. M. Loktev, “Symmetry and the macroscopic dynamics of antiferromagnetic materials in the presence of spin-polarized current,” *Physical Review B*, vol. 85, Apr 2012.
- [141] X. Fan, H. Celik, J. Wu, C. Ni, K.-J. Lee, V. O. Lorenz, and J. Q. Xiao, “Quantifying interface and bulk contributions to spin-orbit torque in magnetic bilayers,” *Nat Comms*, vol. 5, Jan 2014.
- [142] T. Suzuki, S. Fukami, N. Ishiwata, M. Yamanouchi, S. Ikeda, N. Kasai, and H. Ohno, “Current-induced effective field in perpendicularly magnetized Ta/CoFeB/MgO wire,” *Appl. Phys. Lett.*, vol. 98, no. 14, p. 142505, 2011.
- [143] M. Kawaguchi, K. Shimamura, S. Fukami, F. Matsukura, H. Ohno, T. Moriyama, D. Chiba, and T. Ono, “Current-Induced Effective Fields Detected by Magnetotransport Measurements,” *Applied Physics Express*, vol. 6, p. 113002, Nov 2013.
- [144] C. Zhang, M. Yamanouchi, H. Sato, S. Fukami, S. Ikeda, F. Matsukura, and H. Ohno, “Magnetotransport measurements of current induced effective fields in Ta/CoFeB/MgO,” *Appl. Phys. Lett.*, vol. 103, p. 262407, Dec 2013.

- [145] U. H. Pi, K. Won Kim, J. Y. Bae, S. C. Lee, Y. J. Cho, K. S. Kim, and S. Seo, “Tilting of the spin orientation induced by Rashba effect in ferromagnetic metal layer,” *Applied Physics Letters*, vol. 97, no. 16, p. 162507, 2010.
- [146] S. Emori, U. Bauer, S.-M. Ahn, E. Martinez, and G. S. D. Beach, “Current-driven dynamics of chiral ferromagnetic domain walls,” *Nat Mater*, vol. 12, pp. 611–616, Jun 2013.
- [147] P. Wadley, A. Crespi, J. Gazquez, M. Roldan, P. Garcia, V. Novak, R. Campion, T. Jungwirth, C. Rinaldi, X. Marti, and et al., “Obtaining the structure factors for an epitaxial film using Cu X-ray radiation,” *J Appl Crystallogr*, vol. 46, pp. 1749–1754, Oct 2013.
- [148] G. Wastlbauer and J. A. C. Bland, “Structural and magnetic properties of ultrathin epitaxial Fe films on GaAs(001) and related semiconductor substrates,” *Advances in Physics*, vol. 54, pp. 137–219, Mar 2005.
- [149] A. Barone, *Principles and Applications of Superconducting Quantum Interference Devices*. World Scientific, 1992.
- [150] Quantum Design, LOT-Oriel Group Europe, *Magnetic Property Measurement System – MPMS®-XL*.